Progress towards a quantum simulator with cold atoms

by

Marisa Perea-Ortiz

A thesis submitted to
The University of Birmingham
for the degree of
DOCTOR OF PHILOSOPHY

Ultracold Atoms Group
School of Physics and Astronomy
College of Engineering and Physical Sciences
The University of Birmingham

March 11, 2015

Abstract

This thesis presents work toward a quantum simulator with cold atoms. Characteristic and defining subsystems of the experimental setup are presented. Among them there are: the self-made viewports for ultra-high vacuum using indium seals, work on a modular laser system, for laser cooling, with miniaturised optics for the optimization of double path acusto-optic modulator. Work on a computer control to implement past slot is also presented.

A versatile detection system for absorption imaging was designed and built. This detection system is stable, easy to align and exchange of magnification is simple. As well, a high resolution imaging system was designed, built and tested. This imaging system uses commercial microscope objectives and has been designed to work with four different microscope objective. Magnification of $5\times$, $10\times$ $20\times$ and $50\times$ are possible. With the maximum magnification of $50\times$ a resolution of 1.74μm for 780nm was achieved. Also a camera control for in-situ absorption imaging was programmed. Calculation of number of atoms and temperature were implemented in the program, as well as a defringing algorithm.

A new method for temperature calculation for atoms held in a magnetic quadrupole trap was developed and tested, giving similar calculation of temperature as the commonly known time of flight (TOF) method. It is shown that this new method gives better results than the common TOF method for short time of flight.

Characterization of atom losses and heating in the production of a Bose-Einstein condensate were performed.

ACKNOWLEDGEMENT

First of all I would like to thank my supervisor, Professor Kai Bongs, for giving me the opportunity to work in this group, for his motivation, patience, enthusiasm, and immense knowledge. Besides my advisor, I would like to thank Dr Jochen Kronjaeger for his guidance and teaching; also for the work he has done to keep the teamwork in the project.

I want to thank my colleagues Nadine Meyer, Michael Holynski, Mathis Baumert, Charlotte O'Neal and Harry Proud. Nadine, at the beginning of the PhD you helped me a lot to familiarise with the experiment and at the end you were the greatest support in writing up, for what I sincerely like you. Mike, the prank master (even if you do not admit it), I thank you for all the enjoyable time, at work and out side work. Mathis thanks for make me a tea addict, I do like it. Charlotte thanks for your friendly support and discussion when both got stuck with the experiment or with the theoretical part. Harry, our latest member of the project, I hope you have as wonderful time in the lab as we did.

I want to thanks my boyfriend Alex, for all your support and patience, also for cooking while I was writing up. I also want to thanks all the other members of the Quantum Matter group. You all have made this a very special four years to me.

Thanks to the workshop team, Steve, Dave, Toby, Jag, John, Ben and Alex. The experiment would not exist without all the parts that you have built for us.

To my family, parents Santiago and Magdalena, sisters Monica and Marlene, nieces Kate and Chelsea, nephew Zinedine and my brother in law Iram, thanks for all the support, I love you.

CONTENTS

CHAPTER 1

INTRODUCTION

Ultra cold gases have emerged as new quantum systems that are unique in precision and flexibility for control and manipulation. Since the first achievement of Bose-Einstein Condensation of neutral atoms in 1995 [1–3], a lot of experiments have been able to reproduce this goal, giving the opportunity to study the phenomenon deeply and improve the required techniques such as laser cooling, magnetic trapping and evaporation cooling. Bose-Einstein condensation can be used as a tool for understanding other phenomena like superconductivity, Mott insulator transitions [4] and Anderson localisation [5–7] which can be simulated [8] easily with neutral atoms in a more controlled fashion than solid state experiments.

The experiment aim is to create a quantum mixture of bosons ^{87}Rb and fermions ^{40}K which can be used to simulate condensed matter problems in two dimensions (2D), for that reason we need the full control over disorder and interaction between atoms, in addition to an ultra cold quantum gas. In order to simulate the crystal structures of condensed matter systems an optical lattice would be implemented. The disorder can be generated by two different ways, adding impurities at the system, in this case a second atom species ^{87}Rb or by making an irregular optical lattice using a spatial light modulator (SLM). The interaction between the atoms can be modulated at will by Feshbach resonances [9]. An elemental description for bosons and fermions particles is given in the following section.

1.1 Bosons and Fermions

In the quantum world the particles can be classified into two general groups, *bosons* and *fermions*. Each group has rules that the particles follow. Bosons possess integer spin and can occupy the same quantum state. On the other hand fermions have half-integer spin and obey the Pauli exclusion principle that forbid the particles to occupy the same quantum state. One example of bosonic particles are photons which commonly occupy the same quantum state. A familiar example of fermions are the electrons, which are known to fill the electronic shell of the atoms following Pauli exclusion principle. Further more, the atoms are bosons or fermions depending in their total angular momentum. For instance, potassium has three isotopes, ^{39}K and ^{41}K that are bosons and ^{40}K which is fermion.

The behaviour of a group of bosons is described by the Bose-Einstein statistics. On the other hand fermions are described by Fermi-Dirac statistics. Both of these statisticd s give us the probability of the particle (fermion or boson) to occupy a specific energy state E and are given by:

$$\boxed{n(E) = \frac{1}{\exp[(E-\mu)/k_B T] - 1}} \quad \text{Bose-Einstein statistic, and} \tag{1.1}$$

$$\boxed{n(E) = \frac{1}{\exp[(E-\mu)/k_B T] + 1}} \quad \text{Fermi-Dirac statistics,} \tag{1.2}$$

where μ is the chemical potential, k_B is the Boltzmann constant, T is the temperature of the ensemble.

When the energy of an ensemble of bosons is reduced, interesting phenomenon start to happen. All the particles begin to occupy the lower energy levels. When there is not energy left, all the particles occupy the minimum energy level. On the wave-function point of view when the energy is reduced, the particle wave packages overlap creating a single wave package that describe the whole ensemble of particles. This collapse of the wave function or occupation of the minimum energy level is called Bose-Einstein condensation (BEC). On the other hand, when the energy of an ensemble of fermions is reduced, all the particles cannot occupy the same lowest energy level but will occupy the lower energy levels, filling the lowest first. The total energy of this fermionic system is called Fermi energy and has a defined Fermi temperature T_F.

In order to reach degeneracy of bosons like Bose-Einstein condensation (BEC) or degenerate Fermi gases (DFG), the atoms have to be extremely cold (tens to hundreds of Kelvin) and with a high phase-space density in such a way that the atoms are promoted to occupy the lowest energy levels. In the following section is described the usual experimental techniques to reach BEC. The same techniques are used to cool fermions, beside using sympathetic cooling[1] that bypass the Pauli exclusion principle leading to low temperatures of just a fraction of the Fermi temperature T_F.

1.2 Experimental techniques towards BEC

BEC was predicted by Einstein in 1925 [10], when he generalised the theories of Bose [11] about quantum statistics for photons to massive particles. The condition to have a BEC in a gas can be expressed in terms of the deBroglie wavelength, $\lambda_{dB} = (2\pi\hbar^2/mk_BT)^{1/2}$, associated with the thermal motion of the atoms and the spatial density n as [10]:

$$n\lambda_{dB}^3 \gtrsim 2.612 \tag{1.3}$$

To achieve this limit the atoms have to be cooled to a temperature around $\sim 1 - 0.1\mu$K and reach densities of $10^{14} - 10^{15}$cm^{-3} [12]. The invention of laser cooling [13] gave the opportunity to reach temperatures of ∼mK. Due to their simple level structure and the existing lasers at the required frequency alkali atoms turned out to be good candidates for laser cooling. Laser cooling is used as a first stage of cooling, reducing the temperature from hundreds of kelvins to millikelvins. Laser cooling has a limit in the temperature that can be reached given by the Doppler limit [14].

Typically, the second cooling stage to reach lower temperatures is *evaporative cooling*, where hot atoms are stimulated to leave the trap leaving the cooler atoms to rethermalise [15–19]. Evaporative cooling can be performed in magnetic traps [16,17] or in dipole traps [18]. Tight traps are favourable for evaporative cooling since two body collision happen more frequently [17, 20].

Magnetic traps offer big trapping volumes. Different magnetic trap configurations can be found in the literature [21], among them are the quadrupole trap [22], the time-average orbiting potential

[1]Sympathetic cooling is a cooling technique where cold atoms of one specie are used to cool another specie.

(TOP) trap [23], the spherical hexapole, the Ioffe trap and the baseball coil [21]. But the simplest and easiest to build is the quadrupole trap. The only drawback of this trap is the zero magnetic field at the centre where atoms can experience Majorana spin flips [24] and get lost. This problem becomes more evident when the atoms are colder and therefore spend more time around the zero magnetic field [25]. Different approaches to solve this situation have been developed. Commonly used is an optically plugged quadrupole trap [2, 26, 27] where a blue detune laser beam is focused at the zero magnetic field and used to repel atoms from the centre. Other approach is the use of a dipole trap a the zero magnetic field to recapture the lost atoms [28, 29]. The final approach is the one used in this experiment.

On the other hand, dipole traps bring a tighter confinement but smaller trapping volume in comparison with magnetic traps. For that reason a dipole trap is used after atoms have been cooled to few μK. Different configurations of dipole trap (DT) are around: single beam DT [28], cross DT [18, 29, 30], standing wave DT [31, 32]. In this experiment a single beam DT with an astigmatism is used as final trap [33]. This DT has the advantage of producing a quasi-2D trapping potential.

Outline of the thesis

The outline of this thesis is as follows: Chapter 2 introduces the experimental setup, and gives a description of the apparatus that has been built and characterised for the production of BEC. Also described in this chapter are the vacuum system, the laser system, the magnetic traps, the astigmatic dipole trap and the computer control. Chapter 3 gives a more detailed discussion of the detection methods used and how to obtain information of the atomic cloud. The design and characteristics of the detection system and the camera control program used to perform absorption imaging in real time are also presented. Chapter 4 covers the development and testing of a new method of temperature determination for thermal clouds held in a magnetic quadrupole trap. The final results to reach BEC, techniques used and a study of losses in the magnetic traps are given in Chapter 5. Finally a summary of the main result and the outlook for the future progress of the experiment are presented in Chapter 6.

Statement of contributions

This experiment is the product of the work of a small group of people, among them summer, master and PhD student. The main work has been done by the PhD students. In order to optimise the man power the experiment was divided in different sub-projects each with a PhD student responsible for it who does the main design with contribution and ideas from others. Therefore it is not possible to talk about the experiment without mentioning the work of others. In here I highlight their contributions as well as properly referencing them in the text. Chapter 2 gives the description of the experimental set up. The vacuum system was mainly designed by M. Holynski [34], the science chamber was designed by M. Baumert [33] and the 3D MOT chamber for indium seals was designed by N. Meyer [35] and assembled together with the help of the author. The laser system was designed by N. Meyer [35] and the author helped aligning some of the modules. The magnetic coils system was developed by N. Meyer [35], C. O'Neil [36] has done some redesigns of the coils, and M. Baumert [33] built the oil cooling system. The linear rail to move the transport coils was put together by M. Baumert [33] and M. Holynski [34]. The dipole trap design and characterisation was done by M. Baumert [33] and the author helped designing the optical mount for the dipole trap. The computer control is mainly the work of M. Baumert [33] and the author has improved it further. Section 3.4 of chapter 3 is mainly work of the author, with contributions to the camera control (sect. 3.6) from M. Holynski [34]. Chapter 4 is the work of the author and the data was taken by N. Meyer [35]. Chapter 5, is the work of all the members and the data analysis was mainly done by N. Meyer [35]; the solitons data was taken by H. Proud. The contribution of the principal investigator, Prof. Kai Bongs, and the experiment lead, Dr. J. Kronjeager can be assumed throughout.

.

CHAPTER 2

EXPERIMENTAL SETUP

The aim of this project is to create a flexible ultra cold atom experiment that is capable of producing a quasi 2D Bose-Einstein Condensate (BEC), Bose-Fermi mixtures and degenerate Fermi gases (DFG). This robust, stable and versatile setup can be used as a tool to study physical phenomena like the propagation of solitons [37–40], condensed matter systems [41] and the simulation of transport mechanisms that have analogies in photosynthesis [42].

When different atom species are loaded simultaneously into the same magneto-optical trap (MOT) they disturb each other [43,44]. In order to improve the loading of the atoms this experiment has been designed to have separate 2D-3D MOT setups for each species and can be extended to introduce a third species. At the moment a single 2D-3D MOT setup has been built as a proof of principle but the entire setup has been designed to allocate a second 2D-3D MOT setup. After the atoms have been loaded into the 3D MOT they are moved to the science chamber. The science chamber [33] locates the final steps of the experimental sequence and is the place where the BEC is realised. This chamber can accommodate a 2D optical lattice that can be used to simulate condensed matter systems [5, 8, 41]. The design of the science chamber and its specific features will be discussed in sect. 2.1.3.

In order to perform laser cooling a stable and robust laser system is needed. The stimulation of the atoms is extremely sensitive to the frequency of the light since the absorption spectrum of the atoms is discrete. Therefore the laser system needs to be stabilised with the atoms as will be shown later in sect. 2.3. As well it will be explained the different tasks that the laser system performs.

In order to combine the different species magnetic transport from the MOT chamber to the science chamber is needed, as well as local magnetic trapping in each chamber [35]. Therefore a two layer coil layout was implemented where the inner pair of coils are used for local trapping and the outer pair transports the atoms between the vacuum chambers. The two layer layout has some implications on the design of the vacuum chamber and the coils; mainly the narrow design for both coils and vacuum chambers in order to avoid high power consumption of the transport coils. More information about the vacuum is given in sect. 2.1 and the magnetic trapping and transport in sect. 2.4.

The quasi-2D regime for the BEC is achieved by using an astigmatic dipole trap (DT) where the confinement in the vertical direction is much tighter than in the horizontal plane [33]. More details about the design and characteristics of the dipole trap are given in sect. 2.5.

Another aspect that is considered is the observation and manipulation of the BEC. In order to resolve a single lattice site ($\sim 1.5\mu$m) a high resolution imaging system is needed. This is achieved by implementing commercial microscope objectives. In combination with the narrow science chamber design such resolution can be reached. More details of the imaging system will be given in chap. 3.

A general picture of the experimental system is presented in figure 2.1. The vacuum system consists of three main parts: the 2D MOT chamber, the 3D MOT chamber and the science chamber with different chambers are connected with differential pumping stages to isolate regions of high background gas pressure from other with better vacuum. Figure 2.1 also shows the different sets of coils for magnetic trapping and transport (3D MOT, transport and Feshbach coils). The 3D MOT coils have been mounted at the front and the back of the 3D MOT chamber according to figure 2.1. The transport coils are mounted on a mechanical rail that moves them from the 3D MOT chamber to the science chamber and back. The Feshbach coils are mounted closely around the science chamber. These coils can be connected in anti-Helmholtz or Helmholtz[1] configuration. In the Helmholtz configuration the coils can be used to induce Feshbach resonances [9, 45, 46].

[1] Coils in Helmholtz configuration produce a homogeneous magnetic field at the center of the coils. In anti-Helmholtz configuration the coils produce a magnetic quadrupole trap sect. 2.4

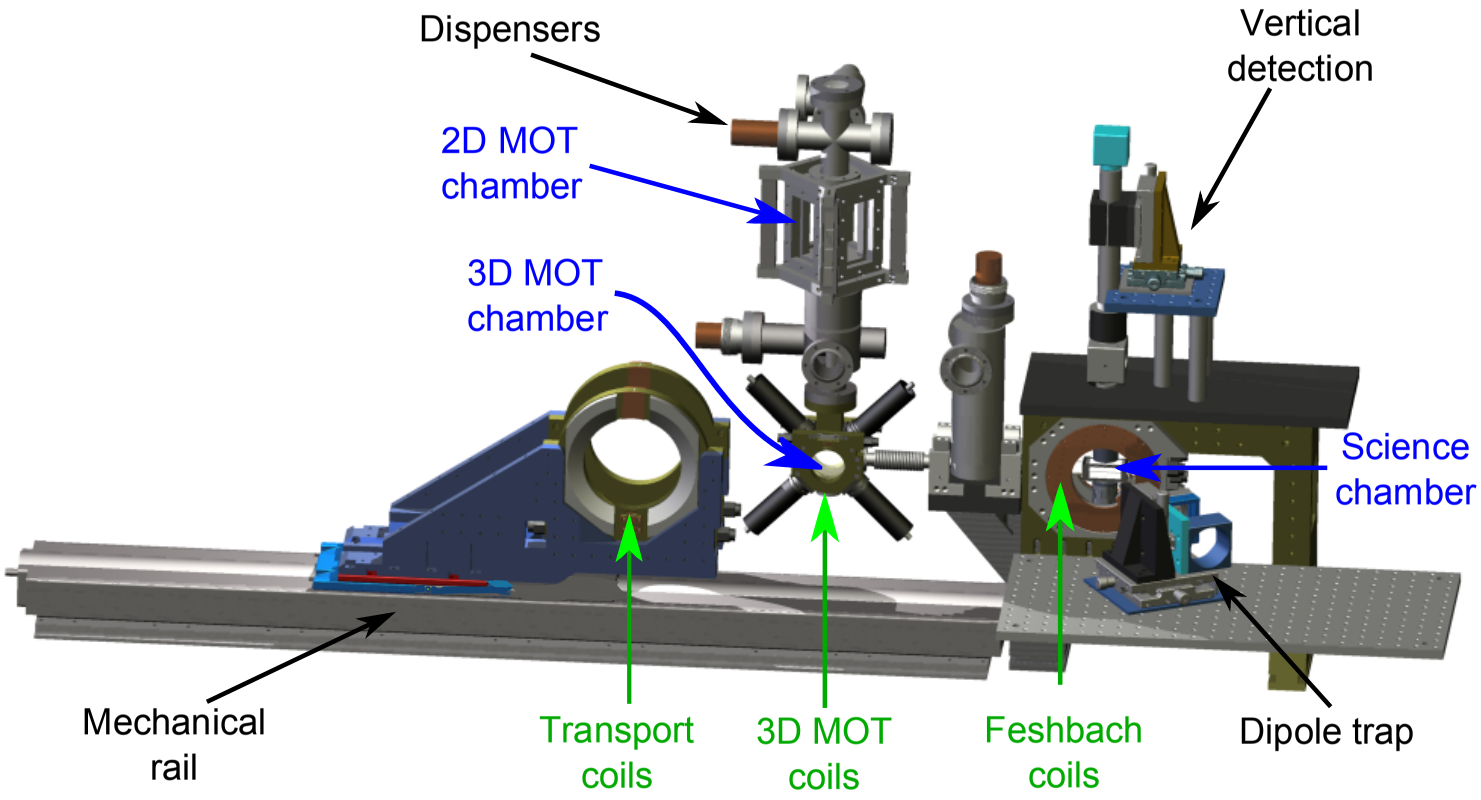

Figure 2.1: *Experimental setup.* The most relevant parts of the vacuum system are shown: 2D MOT, 3D MOT and science chamber (blue). The different sets of coils for magnetic trapping and transport (3D MOT, transport and Feshbach coils) are shown (green). Other components shown are the linear rail used to move the transport coils, the optics for the dipole trap, and the vertical detection setup. The ion getter pumps are not shown for clarity, as well as the optical setup for the 2D MOT.

This chapter gives detail of the apparatus that has been built and developed in the laboratory. It is divided in five sections: vacuum system (sect. 2.1), laser system (sect. 2.3), magnetic trapping and transport (sect. 2.4), dipole trap (sect. 2.5) and finally the computer control (sect. 2.6).

2.1 Vacuum system

A high background pressure of the desired species allows a quick loading rate of trapped atoms but also introduces a high level of background collisions that reduces the magnetic trap life time. In order to achieve a large number of trapped atoms and a long life time it is therefore preferable to have a high gas load location for fast capturing and precooling (2D MOT) and then move the atoms into a region with lower background pressure for further cooling and trapping with a longer life time (3D MOT). This is achieved by using a 2D-3D magneto-optical trap setup (fig. 2.1).

The main purpose of the vacuum system is to provide a suitable low pressure environment for the experiment. By reducing background collisions it supplies long trapping times for atoms. Achieving pressures of 10^{-11}mbar (ultra high vacuum) reduces collisions with background gas leading to sufficiently long trapping times of 41s and 52s in the 3D MOT and the science chamber respectively [35]. In order to maintain the desirable pressure regime pumping techniques such as ion getter pumps (IGPs) and titanium sublimation pumps (TSPs) are used.

The design of the vacuum system was mostly done by Holynski [34], the science chamber was designed by Baumert [33] and the 3D MOT chamber with indium seal was designed by Meyer [35]. However it is presented for completeness of the experimental system description. The specific characteristics of three main vacuum chambers are discussed in the following sections.

2.1.1 2D MOT chamber

In order to capture a high number of atoms an extended trapping volume is favourable. Therefore a home made chamber with rectangular windows has been built accommodating elongated 2D MOT beams. The chosen vacuum sealing technique for the 2D MOT chamber is lead seals. This type of seal offers a high baking temperature $\sim 300°$C [47] but has the necessity of permanent compression flanges that makes this technique bulky but since spatial restrictions do not apply in the 2D MOT

area it is still efficient. The 2D chamber made of stainless steel with 120mm height uses four BK7 rectangular windows of 100mm×55mm size that accommodate beams of 80mm×20mm cross section [34].

The atoms are introduced into the system using heated dispensers that out gases depending on the current flow. Both ^{87}Rb and ^{40}K dispensers are mounted in a five ways cross at the top of the 2D MOT chamber as can be seen in figure 2.1.

A narrow carbon tube of 6mm diameter and 86mm length at the bottom of the 2D MOT is used as a differential pumping stage to let the atomic beam produced by the 2D MOT pass and to reduce the conductance between 2D and 3D MOT chambers. The 2D MOT optics and magnetic field are described in the following and a more complete description can be found in [34].

2D MOT optics

The 2D MOT needs two pairs of counter-propagating beams and a magnetic field with a minimum line in the centre of the chamber in order to produce the magneto-optical trap. The two pairs of counter-propagating beams for the 2D MOT can be produced by two retro reflected beams, a pair of mirrors and large $\lambda/4$ wave-plates to maintain the required polarization. A different approach implemented in this experiment is to use prisms (fig. 2.2) instead of the back reflecting mirror and wave-plate providing the correct polarisation without the necessity of wave-plates [34].

The beam preparation for the 2D MOT is described in figure 2.2. Light coming from a polarisation maintaining fibre is collimated and aligned with a pair of mirrors. Collimated, linearly polarised beams are sent through a $\lambda/4$ wave-plates creating circular polarised light. Collimated elliptical beams are produced by a combination of two cylindrical lenses L_1 and L_2 which focal length $f_1 = -30$mm and $f_2 = 150$mm. The beams pass through the 2D MOT chamber and are back reflected with a pair of prisms. The second reflection in the prisms provide the required polarisation. The light passing through the middle of the prisms is not reflected causing an unbalance between the counter-propagating beams. It has been proven that this unbalance does not cause atom losses [35].

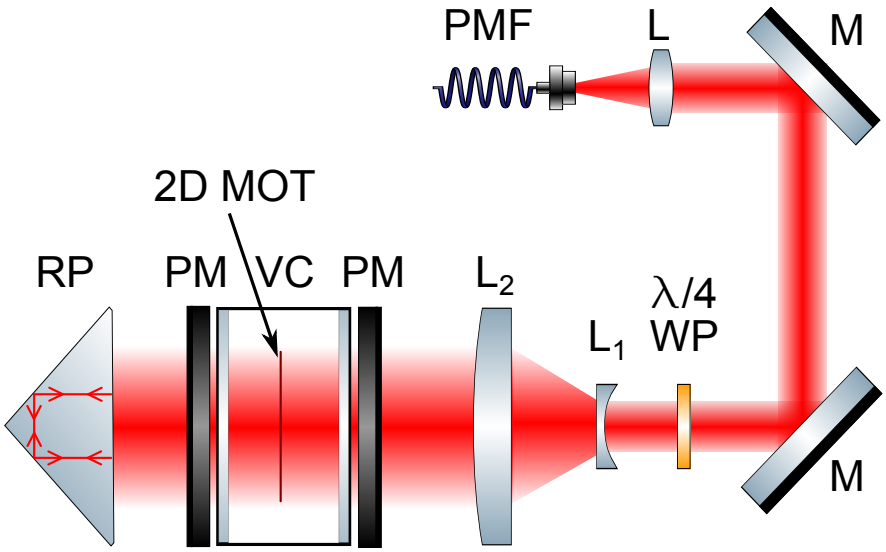

Figure 2.2: *Optical and magnetic setup for the 2D MOT seen from the side.* The 2D MOT has two elliptically collimated beams of which one of them is depicted in this drawing. The preparation of the second beam is the same. Light coming from a polarization maintaining fibre (PMF) is collimated by an achromatic lens (L) and passes through two adjustable mirrors (M). The collimated and linearly polarised beam passes through a $\lambda/4$ wave plate (WP) to generate circular polarised light. Afterwards, the beam is expanded by a lens system formed of two cylindrical lenses L_1 and L_2 with focal length $f_1 = -30$mm and $f_2 = 150$mm creating an elliptical beam with an approximate cross section of 20mm×80mm. The beam passes through the vacuum chamber (VC) and is back-reflected with a retro-reflecting prism (RP). The combination of two reflections provides the required circular polarization for the MOT. Permanent magnets (PM) are used to produce the magnetic gradient needed for the MOT. At the center of the chamber the dark red line illustrates the position of the 2D MOT.

2D MOT magnetic field

The magnetic gradient needed to produce a magneto-optical trap is relatively small ($\approx$ 15G/cm) and it can be generated by coils or permanent magnets. The use of coils enables for an easily tunable gradient by varying the current as well as the possibility to displace the zero of the magnetic field. The main disadvantage of the coil configuration is that the heat dissipated by air cooled coils is enough to induce birefringence on the 2D MOT windows. This birefringence was sufficient to perturb the polarization of the 2D MOT beam [34]. Permanent magnets are used instead as can be seen in figure 2.2. Permanent magnets prevent heating but the variation of the magnetic gradient and center becomes more complicated and the tunable range is more restricted. The magnets have

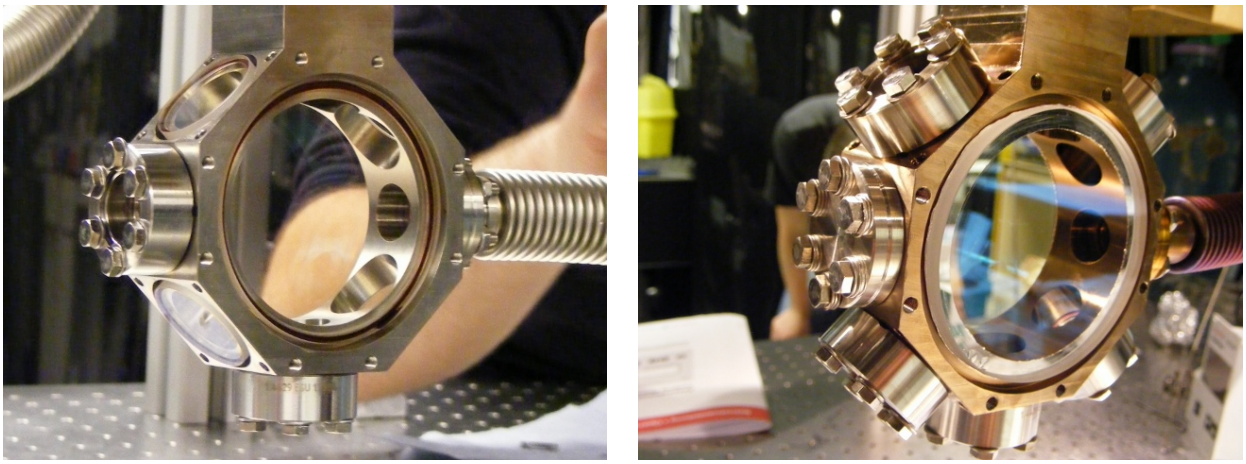

Figure 2.3: *Different sealing techniques used for the 3D MOT chamber: epoxy seal (left) and indium seal (right).* The following description is valid for both 3D MOT chambers. The 3D MOT chambers have an octagonal shape that makes it easy to locate the three pairs of counter-propagating beam, as well as giving good optical access. At the top is the 2D MOT connected via a differential pumping stage with a CF35 flange (not displayed in the pictures). At the bottom a CF16 viewport is placed for testing purposes like 2D MOT alignment and 3D MOT cloud examination. At the right a flexible bellow is connected to a differential pumping stage followed by the science chamber. And at the left a second CF16 viewport can be replaced with another flexible bellow that will connect to the second 3D MOT chamber. On the left picture the 3D MOT chamber uses six epoxy seals, two at the side windows and four at the diagonal windows. On the right picture indium seals are used for the two side windows and four CF16 viewports are used for the other windows.

been fixed with glue to the vacuum chamber after they have been aligned [34].

2.1.2 3D MOT chamber

Due to the restrictions given by the magnetic coil design (see sect. 2.4) a narrow self made 3D MOT chamber was designed to satisfy the special requirements of the experiment (more details can be found in refs. [34, 35]). The 3D MOT chamber of octagonal shape (fig. 2.3) fits three pairs of counter-propagating and orthogonal beams for laser cooling and is designed for good optical access. Also it possesses openings in the horizontal direction to connect to the science chamber and to the second 3D MOT chamber. In the vertical direction it connects to the 2D MOT chamber via a differential pumping stage with a CF35 flange. At the bottom it is connected to a CF16 viewport used for testing purposes.

An extensive explanation of sealing techniques for different vacuum regimes can be found in [47].

In the special case of UHV is recommended to use materials with high baking temperature, with low permeability for gases and low outgassing rate. Typical self made metal-glass vacuum seals use indium, lead or in some cases epoxy glue. Indium and epoxy offer thin seals but relatively low baking temperatures of 130°C and 200°C respectively [34, 47]. In contrast lead has a higher baking temperature of 300°C but needs extra space for permanent compression flanges. This makes lead not a suitable option for the 3D MOT chamber.

The first approach for all window sealings at the 3D MOT chamber was epoxy glue [48] (seen in fig. 2.3 left). Glued windows provided good optical access and a narrow design. The 3D MOT chamber is designed to have four diagonal windows a clear aperture of 22mm diameter for the crossed MOT beams. This open view and the use of CF16 ports[2] give the limit of the thickness of the 3D MOT chamber to 36mm. At the beginning this technique gave low pressures ($\sim 10^{-11}$mbar) but long term water permeability problems led to a different technique being used. More informations about the 3D MOT chamber design and the glueing technique can be found in [34].

The second approach for thin seals and the technique finally used is indium sealing (seen in fig. 2.3 right). Indium is chosen because it provides a thin, easy and strong seal since it wets metal and glass simultaneously. Indium was not considered as a first option due to its low melting point of 157°C [49]. The sealing scheme is simply chamber-indium-window, meaning no extra holders are needed.

The indium seals were implemented only on the two big side windows where keeping a narrow seal is crucial. The four small window seals were replaced with CF16 viewports. This allows to keep the same chamber design and thickness (36mm) except for small changes to the crossed MOT telescope that will be discussed at a later point in 3D MOT optics.

A more detailed description of the indium sealing production is given in the next section.

Indium sealing technique

Indium as a vacuum seal has been used since 1956 [50]. It is normally used in a circular configuration [51] but can also be used for different shaped seals, like ellipsoids [52]. A review of different indium seals can be found in [47]. It is advised to have a clean and dry surface for the seal [53, 54]. The

[2] CF16 flanges have an outer diameter of 34mm.

range of indium wire used varies from $0.5 - 2$mm in diameter depending on the size of the seal with small seals using thinner wires [47]. High purity indium is preferred [53] for clean applications. Cleaning the outer layer of the indium wire with acetone or 10% solution of hydrochloric acid to remove oxide is highly recommended for better bounding [53].

An important point for a good indium seal is the preparation of the sealing surfaces. It is necessary to have a flat, smooth and clean surface. In order to meet these requirements the vacuum chamber of stainless steel has been machined with a lathe to avoid scratches perpendicular to the direction of the seal that could lead to leaks [35]. The vacuum chamber has been baked at a high temperature (~ 400°C) for two days. As a cleaning procedure, all metal parts (vacuum chamber, compression flanges and jig) have passed through a succession of 15 minutes in an ultrasonic bath with acetone followed by a solution of liquinox and finally isopropanol. The windows are cleaned with isopropanol.

For the seal, an indium wire[3] of 1mm diameter and 99.999% purity is used. It is cleaned with acetone. A viton ring of ~ 67mm diameter and 1.5mm thickness is used to protect the window from direct contact with the compression flange. It has the same diameter as the indium ring helping to symmetrically apply the pressure.

The design of the chamber can be seen in the top left of figure 2.4. The chamber has a step where the window of 70mm diameter is placed. Window and chamber have an overlapping area without optical coating of 6mm for the indium to expand into (fig. 2.4 top right).

A step by step description of the manufacturing of the indium seal can be seen in figure 2.4 (from top to bottom, from left to right).

a) After the chamber has been prepared, a jig is used to shape the indium. A piece of aluminium foil is placed underneath to protect the chamber surface from scratches when the indium wire is cut.

b) A loop of 67mm diameter of indium is formed. One end is laid on top of the other and both are simultaneously cut at an angle to maximise the surface contact between the ends. The excess wire is removed and the two freshly cut edges readily stick together.

[3] Goodfellow IN005130.

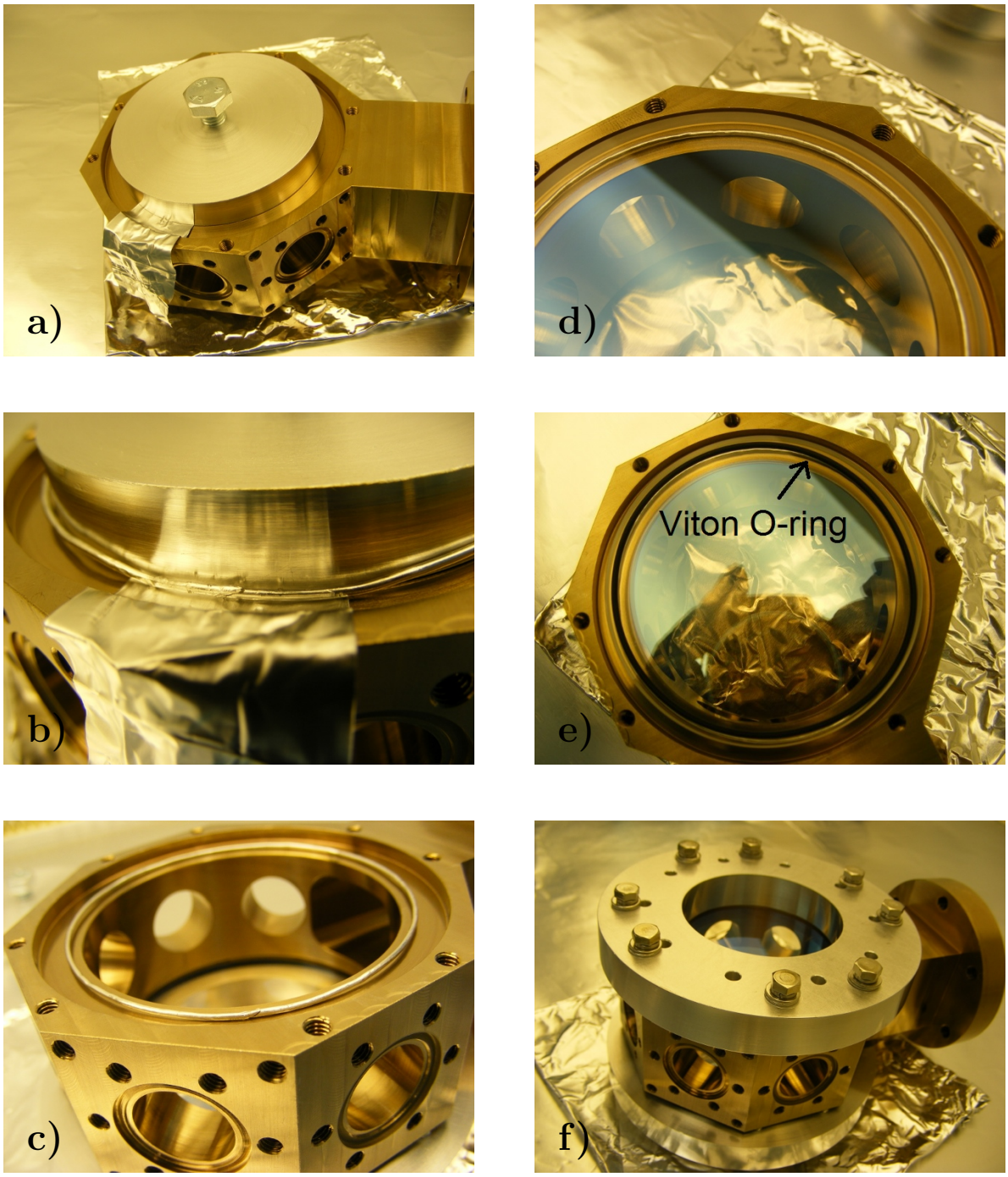

Figure 2.4: *Stages for the production of an indium seal.* a) A jig is used to shape the indium wire in a ring of 67mm diameter. It rests on the chamber rim with a piece of aluminium foil underneath to protect the chamber from scratches when the indium wire is cut. b) Indium is placed around the jig making a ring. Overlapping ends are cut at an angle and joined together. c) Aluminium foil and jig are carefully removed, leaving the indium ring centred. d) The window is centred on the chamber and placed cautiously on top of the indium ring. e) A viton O-ring is laid on top of the window coinciding in position with the indium ring. f) The compression flange is mounted and fixed with eight M4 screws.

c) The aluminium foil and jig are removed carefully leaving a centred indium ring with the appropriate diameter.

d) The window is centred on the chamber and placed carefully on top of the indium ring. The aim is to have the indium ring at the middle of the overlapping area between window and chamber.

e) The viton O-ring is put on top of the window coinciding in position with the indium ring in order to ensure that the pressure is applied in a controlled way through the indium when the compression flange is fixed.

f) A compression flange is placed on top and fixed with eight M4 screws in order to compress and flatten the indium. To provide a homogeneous compression on the indium an alternating criss-cross star pattern is used to tighten the screws, doing steps of 0.2Nm until 2Nm is reached.

The vacuum chamber was mounted on the system. Evacuating the vacuum system and baking at 130°C, a pressure of $\sim 10^{-11}$mbar according to the ion pump was reached. The compression flanges were removed and the seals still perform even after the vacuum system was vented to atmospheric pressure. After evacuating for the second time a similar pressure was achieved.

3D MOT optics

Six collimated MOT beams with 19.7mm diameter at $1/e^2$ intensity were used in the first 3D MOT design (fig. 2.5 left). With the implementation of the new chamber with CF16 viewports on the cross windows divergent beams had to be used instead. Since the new viewports have a clear aperture of 12.7mm which will cut $\sim 25\%$ of the light for the collimated beams. The new four cross telescopes are constructed to provide the same beam size at the centre of the MOT but using divergent beams (fig. 2.5 right). The two horizontal beam did not need to be modified, therefore they are collimated beams.

2.1.3 Science chamber

The science chamber (fig. 2.6) is the place where the BEC is realised as well as where the simulations will be done. It has excellent optical access allowing the location of all beams needed: the beams for

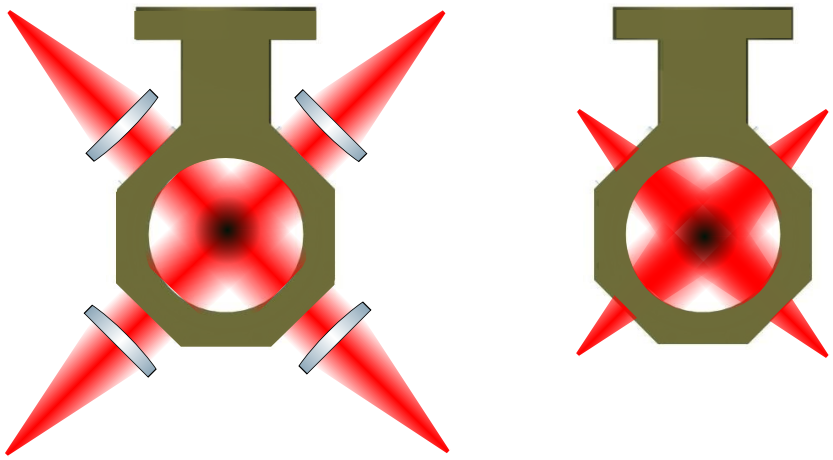

Figure 2.5: *3D MOT optics*. On the left, the 3D MOT chamber with glued windows and the four crossed collimated beams is shown. Each of these beams have been collimated with an achromatic lens ($f = 100$mm) giving a beam size of 19.7mm diameter at $1/e^2$ intensity. On the right, divergent beams are used, providing the same beam size as the collimated beams at the center of the trap (atoms position).

the dipole trap, the optical lattice, the detection, and the manipulation. The science chamber[4] is a glass cell composed of five individual windows bounded to a quartz frame using epoxy glue. The quartz frame serves as an absorber for scattered light. The glueing technique gives the opportunity to have anti-reflecting coatings on both window surfaces. The vertical dimension (23mm) and the thickness of the glass (3.5mm) used for the science chamber fits the working distance (13.9mm) of the glass corrected microscope objectives that are used for detection and manipulation. The other two dimensions (33mm×60mm) are optimised for optical access. More details about the science chamber design can be found in [33].

A differential pumping stage is used to connect the science chamber to the 3D MOT chamber. It allows to keep a pressure ($\sim 10^{-12}$mbar) one order of magnitude lower than the 3D MOT chamber according to the ion getter pump readings.

[4] Japan cell.

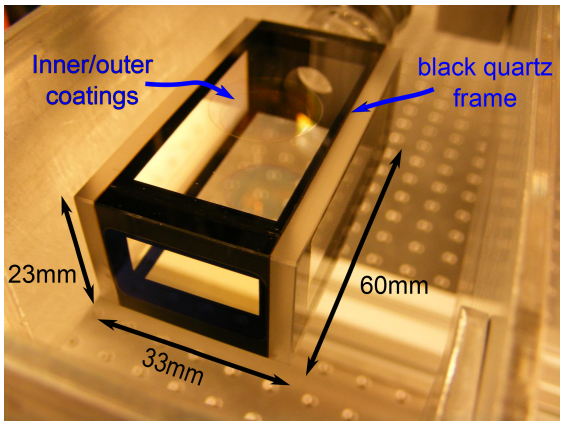

Figure 2.6: *Science chamber* with a narrow design (23mm×33mm×60mm). The vertical dimension (23mm) is optimised for imaging and manipulation with commercial microscope objectives. The science chamber is composed of five individual windows that have internal and external coatings and are glued to a quartz frame.

2.2 Laser Cooling

In laser cooling the radiation force produced by a laser beam is used to reduce the velocity distribution of an atomic cloud. Generally the velocity distribution of the cloud corresponds to a Boltzmann distribution characterized by the mean velocity $\langle v \rangle$ and the velocity dispersion Δv around the mean $\langle v \rangle$. The interaction with a laser beam can modify both of them. By reducing $\langle v \rangle$ the atoms are slow down, but by reducing the velocity spread Δv the temperature is lowered. The decrease of the velocity spread Δv caused by the interaction with the laser light is called "laser cooling". In this section it is described a few laser cooling mechanisms, in the simple case of two-level atoms.

In order to modify Δv, the radiation force must depend on v. Let us take the simplest case of a two-level atom with with frequency ω_0 in the presence of a laser beam with frequency ω_L. The simplest way to introduce a velocity dependence in the radiation force is to used the Doppler effect, which changes the detuning $\Delta = \omega_L - \omega_0$ from resonance by an amount proportional to the velocity v of the atoms. Since the radiation force depends of the detuning Δ, the velocity dependence of the detuning induces a velocity dependence of the force. This type of cooling is called *laser Doppler cooling*

$$F(v) = F_0 + \beta v \tag{2.1}$$

the first is term is the velocity-independent part of the force. The linear term βv (where the coefficient β is negative for red detuning) can be interpreted as a friction force that would damp the atomic velocity to zero if the force F_0 was equal to zero. The theoretical derivation of this force is given in the next sections.

2.2.1 Light forces on moving atoms

This section aim is to show how the semiclassical theory of the light force (Appendix A) can be extended to moving atoms. The first subsections considers the simplest case: an atom moving in a plane wave. Then in the next subsection a simple model leads to an approximation for the light force of an atom moving on a 1D standing wave.

Even when the light force will eventually alter the velocity of the atom $\vec{v}$ it is assume constant in the following derivation. This assumption is justify since the momentum transfer from a single photon $\hbar\vec{k}$ is much smaller than the atom's momentum $m\vec{v}$. Thus many absorption cycles are needed to change $\vec{v}$ noticeable.

Moving atom in a single plane wave

Consider an atom moving with velocity $\vec{v}$ in a plane wave propagating in the $\hat{z}$ direction. To solve this problem it is easier to used the reference frame of the moving atom, where the atom is stationary and the plane wave has a Doppler-shifted frequency ω'_L given by

$$\omega'_L \cong \omega_L \left(1 - \frac{v_z}{c}\right) = \omega_L - \vec{k} \cdot \vec{v} \tag{2.2}$$

The light field is monochromatic in the atomic reference frame, so the resulting scattering force (eq. A.21) for the stationary atom is used with a new detuning $\Delta' = \Delta - \vec{k} \cdot \vec{v}$ resulting in a force

$$\vec{F}_{\text{scatt}} \cong \hbar\vec{k} \left(1 - \frac{v_z}{c}\right) \left(\frac{\Gamma\Omega_0^2}{\Gamma^2 + 2\Omega_0^2 + 4\Delta'^{\,2}}\right). \tag{2.3}$$

The Lorentz transformation back to the lab reference frame does not change the expression for the scattering force. For speeds non-relativistic $v \ll c$ the predominant velocity dependence is $\vec{k} \cdot \vec{v}$ in the denominator, hence the force can be rewritten as

$$\vec{F}_{\text{scatt}} \cong \hbar\vec{k} \left(\frac{\Gamma \Omega_0^2}{\Gamma^2 + 2\Omega_0^2 + 4(\Delta - \vec{k} \cdot \vec{v})^2} \right). \tag{2.4}$$

Analysing this equation can be seen that the scattering force is significant for a narrow range of velocities with $\vec{k} \cdot \vec{v}$ close to Δ. In fact for the low intensity case $\Omega_0^2 \ll \Gamma^2$, the force depends on $\vec{k} \cdot \vec{v}$ is Lorentzian with a FWHM equal to Γ. The reduction of atomic temperatures via the cooling force described above is called **Doppler cooling**.

Moving atom in a 1D standing wave

A one dimensional standing wave consist of two plane waves of equal frequency and intensity, counterpropagaiting along the $\hat{z}$ axis. In the atom's point of view the light field appears bichromatic with frequencies at $\omega_L \pm \vec{k} \cdot \vec{v}$. An useful approximation can be obtained by simply adding the scattering forces due to each of the two counterpropagaiting plane waves. This approximation gives the z-component of the mean light force averaged over a wavelength and in the limit of weak field $\Omega_0^2 \ll \Gamma^2$ interferences and saturation effects can be neglected. Adding the two forces we obtain

$$F_{\text{z}} \cong \hbar\vec{k} \left(\frac{\Gamma \Omega_0^2}{\Gamma^2 + 2\Omega_0^2 + 4(\Delta - kv_z)^2} \right) + (-\hbar\vec{k}) \left(\frac{\Gamma \Omega_0^2}{\Gamma^2 + 2\Omega_0^2 + 4(\Delta + kv_z)^2} \right), \tag{2.5}$$

where Ω_s is the magnitude of the Rabi frequency of each plane wave. In the case when $kv_z \ll \Delta$ and $kv_z \ll \Gamma$ the equation above becomes

$$F_z = \beta v_z \quad \text{where} \quad \beta = \frac{16\hbar k^2 \Gamma \Omega_s^2 \Delta}{(\Gamma^2 + 2\Omega_0^2 + 4\Delta^2)^2}, \tag{2.6}$$

where β is the friction coefficient, and has the same sign of the detuning, therefore the total force is a damping or *cooling* force for red (negative) detuning and an accelerating of *heating* force for blue (positive) detuning. When the detuning Δ is negative, F_z is often referred to as a friction force.

Velocity damping in three dimensions is obtained by an arrangement of three intersecting, mu-

tually orthogonal pairs of counterpropagaiting laser beams. All three velocity components of the atom are damped in the intersection region. Such arrangement is known as **optical molasses**, which is an important form of laser cooling.

2.3 Laser system

In order to meet the requirements for laser cooling and optical manipulation, the laser light must be frequency stabilised to specific frequencies given by the atomic transitions used and have a narrow line width relative to the atomic hyperfine splitting spacing.

In this experiment miniaturised optics are used (fig. 2.7). They were first developed for the QUANTUS project [55, 56]. The miniaturised optic elements have tolerated extreme conditions of decelerations of up to $50g$ [5] without getting misaligned. These small optics have many advantages, for example: better mechanical and temperature stabilities on both short and long time scales [57] and reduced weight and size. The conception of the laser system setup and the design of the modules is due to Meyer [35].

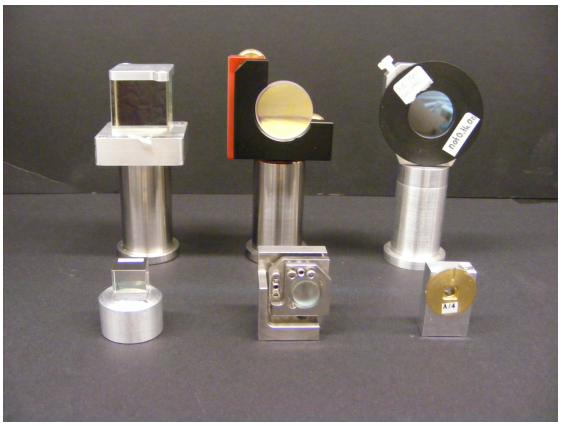

Figure 2.7: *Miniaturised optical elements.* In the picture the small optics design (front) are compared with the common optic elements (back). From left to right: polarising beamsplitter cubes, mirrors and wave plates.

[5] where g is the acceleration of gravity

2.3.1 Laser system overview

The experiment uses two alkaline atomic species, bosonic ^{87}Rb and fermionic ^{40}K. ^{87}Rb and ^{40}K were chosen because both are well known in the cold atoms community and the laser technology for 780nm and 767nm is well developed. This experiment requires two laser systems for laser cooling purposes, one for each species. Overall both systems work in the same way. The only difference is the generated frequencies since the wavelength of atomic transitions for the species are different. The proximity in wavelengths allows in most cases the use of the same optical elements for both laser systems. In principle the potassium laser system can also be used for ^{39}K and ^{41}K because the detuning needed of 126MHz [58] is reachable with this laser system.

The laser system is involved in different stages of the experiment and each of them requires a specific number of beams at the right frequency and power. Starting with the 2D MOT where the atoms are cooled down by laser cooling **cooling** and **repumping** light is needed. After that the atoms are moved to the 3D MOT by a **pushing** beam. Once in the 3D MOT they are recaptured and cooled even further. By optically **pumping** the atoms are transferred into the magnetically low field seeking quantum state before ramping up the magnetic trap. Finally a **detection** beam is needed to illuminate the atoms and deduce their density distribution. In table (2.1) an overview of the atomic transitions and detunings that have been used for each species is given.

The laser system is made up of different modules. This modularity gives flexibility to make changes in some modules without affecting the others. Also these modules can be stacked making it possible to keep the laser system in one third of the optical table. The layout of the modules is shown in figure 2.8 and it is the same for both species. The light is guided through optical fibres between the modules. The modules can be classified in three types: *frequency stabilisation*, *amplification* and *combination and distribution*.

The frequency stabilisation part generates laser light of the required frequencies. It is composed of *Master* and *Offset* modules that have temperature stabilised laser diodes that are controlled by low noise current drivers. The master laser feeds light to the offset modules that then is used as a reference to stabilise cooling and repumping light for laser cooling.

The amplification is done via tapered amplifiers (TA) modules that amplifies the light coming

Element	Light	Transition	Detuning
^{87}Rb	Cooling	$5^2S_{1/2}F = 2 \Rightarrow 5^2P_{3/2}F' = 3$	red-detuned
^{87}Rb	Repumping	$5^2S_{1/2}F = 1 \Rightarrow 5^2P_{3/2}F' = 2$	resonant
^{87}Rb	Pushing	$5^2S_{1/2}F = 2 \Rightarrow 5^2P_{3/2}F' = 3$	red-detuned
^{87}Rb	Pumping	$5^2S_{1/2}F = 2 \Rightarrow 5^2P_{3/2}F' = 3$	resonant
^{87}Rb	Detection	$5^2S_{1/2}F = 2 \Rightarrow 5^2P_{3/2}F' = 3$	resonant
^{40}K	Cooling	$4^2S_{1/2}F = 9/2 \Rightarrow 4^2P_{3/2}F' = 11/2$	red-detuned
^{40}K	Repumping	$4^2S_{1/2}F = 7/2 \Rightarrow 4^2P_{3/2}F' = 9/2$	red-detuned
^{40}K	Pushing	$4^2S_{1/2}F = 9/2 \Rightarrow 4^2P_{3/2}F' = 11/2$	blue-detuned
^{40}K	Pumping	$4^2S_{1/2}F = 9/2 \Rightarrow 4^2P_{3/2}F' = 11/2$	resonant
^{40}K	Detection	$4^2S_{1/2}F = 9/2 \Rightarrow 4^2P_{3/2}F' = 11/2$	resonant

Table 2.1: Overview of the necessary laser frequencies for laser cooling, optical pumping and detection of ^{87}Rb and ^{40}K. These transitions are also shown in figure 2.10.

from the offset modules. After amplification the light is delivered to the combination and distribution modules where cooling and repumping light are combined and distributed into fibres to the experiment. This part has three different modules: 2D MOT module, 3D MOT module and detection module. The last one will distribute light for the pushing beam, optical pumping and detection. The laser system layout, the design of the modules and all work related to frequency stabilisation and amplification has been done by Meyer [35]. The author has contribute with alignment of the distribution modules. A deeper discussion of each module is presented in the next sections.

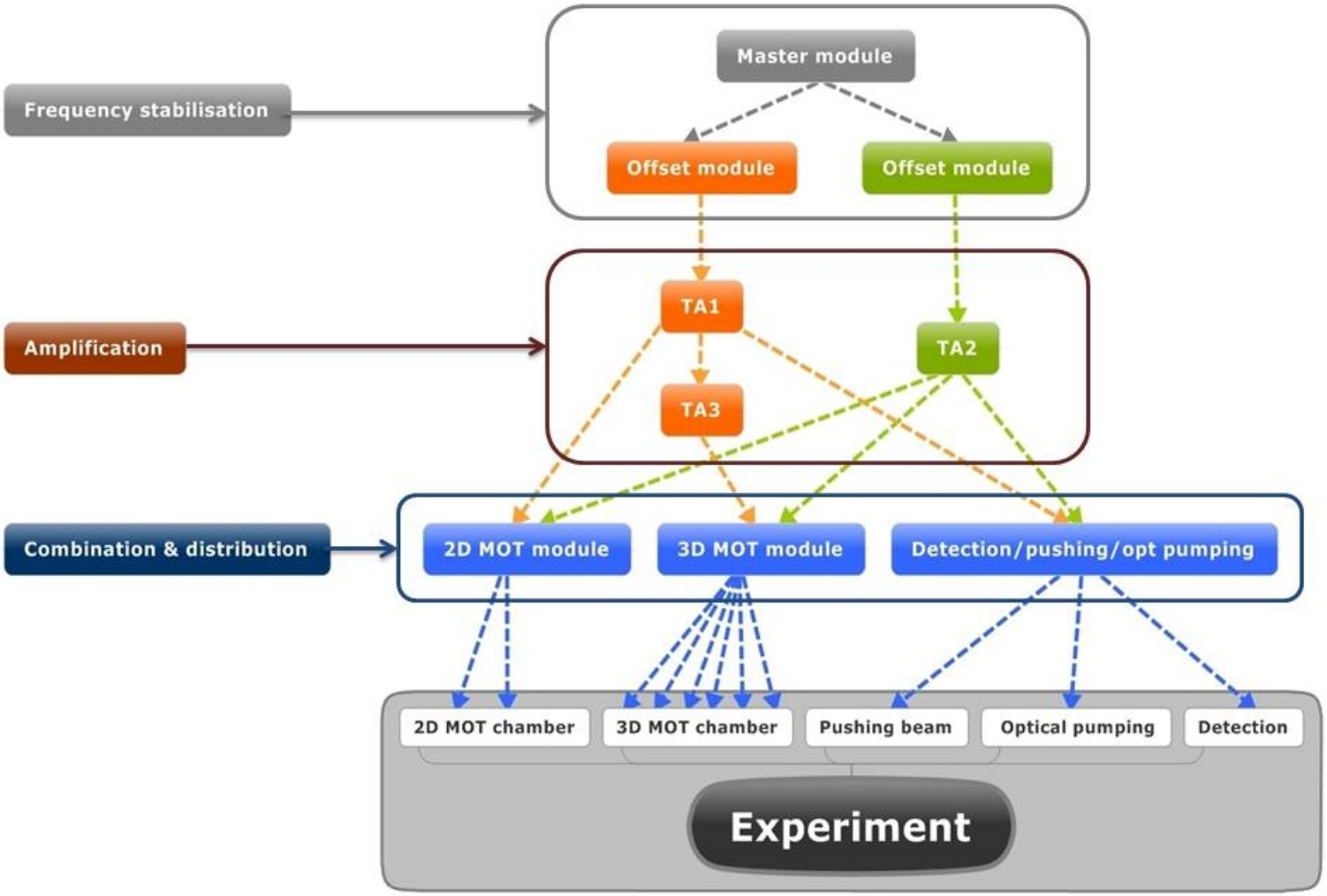

Figure 2.8: *Laser system layout.* This is the representation of the modules organization. The light is guided through optical fibres (dashed arrows) between modules. The modules in the laser system are classified in three groups: frequency stabilisation, amplification and combination & distribution. In the stabilisation part the laser light is generated and set to the required frequencies. The master laser seeds the reference light (gray arrows) to the offset modules which they will use as a reference to generate cooling (orange arrows) or repumping (green arrows) light. At the amplification part the intensity of light gets amplified ($\sim$ 100 times each beam) via tapered amplifiers (TA). The cooling light gets amplified twice since the amount of cooling light needed for laser cooling is higher than repumping light. Afterwards cooling and repumping lights are combined and distributed (blue arrows) to the experiment in the combination and distribution modules.

2.3.2 Frequency stabilization

Alkaline atoms are broadly used in cold atoms experiments for the simplicity on their level scheme due to the fact that they have a single electron in the outermost shell. This electronic structure makes the number of transitions needed for laser cooling to a few and therefore the number of needed laser frequencies is small. The D2 line for ^{87}Rb ($5^2S_{1/2} \Rightarrow 5^2P_{3/2}$ transition) and ^{40}K ($4^2S_{1/2} \Rightarrow 4^2P_{3/2}$ transition) are used for laser cooling (fig. 2.10) since they are cycling transitions.

Master Laser

The light in the master modules (fig. 2.9) is generated by an external cavity diode laser (ECDL) with an interference filter [59] and is stabilised to the crossover $CO23$ transition of the D2 line serving as a reference for locking the ^{87}Rb cooling and repumping laser (fig. 2.10). Due to the low abundance of ^{40}K of less than 0.012% [58] the ECDL laser for potassium has been locked to the saturated absorption spectrum of ^{39}K ($CO12$ transition) for its high natural abundance of 93.26%.

The locking technique used in this module is called frequency modulation (FM) spectroscopy [60] and is commonly used to detect dispersion or absorption features. In this scheme, the laser light passes through a phase modulator (EOM) to produce a frequency modulated optical spectrum composed of a strong carrier with same frequency than the laser, with two weaker sidebands produced by the modulation. The beam is then passed through the sample that contains the spectral feature of interest (gas cell). The sample produces a distortion of the optical signal generating a beat signal. Afterwards the probe light is imposed on a photodiode (PD) where the beat signal can be detected. Since the gas cell is at room temperature all the atomic transitions are Doppler broadened making it difficult or impossible to obtain any transition feature of the atoms. Saturated absorption spectroscopy [61, 62] is therefore also implemented.

In saturated absorption spectroscopy a pump and a probe beam with the same frequency are passed trough the sample (gas cell) in a counter-propagating way. The frequency of pump and probe beam is scanned through the frequency spectrum of relevance for the specific atom transition. When the laser is red detuned from the transition of interest the pump beam excites atoms moving towards

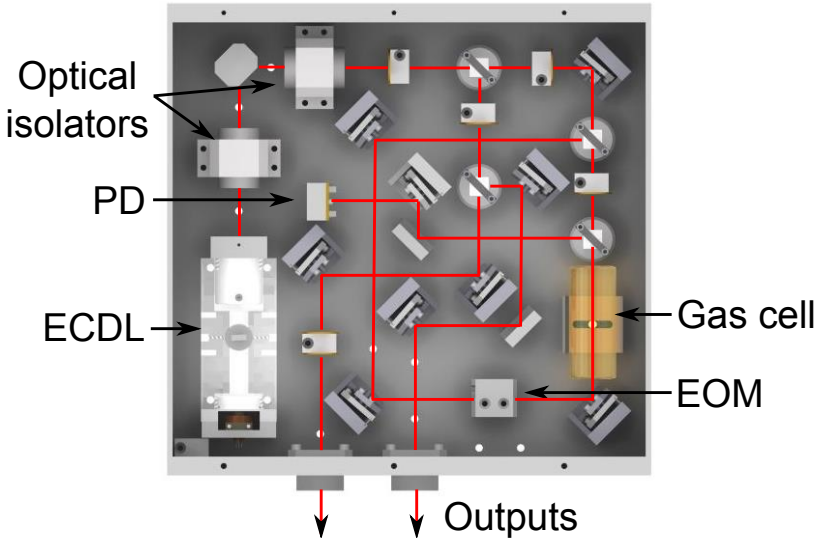

Figure 2.9: *Master module.* At the bottom left light is generated by an external cavity diode laser (ECDL) with interference filter. The light passes through optical isolators and gets divided by a polarising beamsplitter cube and a $\lambda/2$ wave plate. The transmitted beam is used for spectroscopy and the deflected beam is coupled into two fibres (outputs). In the spectroscopy beam path the light is divided into probe and pump beam. Both beams counterpropagate through a gas cell. The probe beam is modulated with an electro optical modulator (EOM) before it passes through the gas cell, afterwards it is detected on a photodiode (PD).

it with velocity v and the probe beam excites atoms moving at the opposite direction with a velocity $-v$. When the laser is blue detuned the excited atoms are moving away from the beams $-v$ for the pump beam and v for the probe beam. In both cases red and blue detuning, the probe beam is absorbed giving a zero transmission signal. But if the laser light is on resonance with the transition of interest the pump beam that is much stronger than the probe beam saturates the sample making it transparent for the probe beam giving a dip in the absorption signal easy to detect. For multilevel atoms extra transitions appear when the pump and probe beams are on resonance with different transitions so called crossover transitions. This transitions are normally stronger than the natural transitions and are commonly used as a reference for locking lasers as it is in our case.

The locked light generated in the master module is distributed into two fibres and is used as a reference frequency for the offset modules. Each master module provides the atom reference frequency for each laser system.

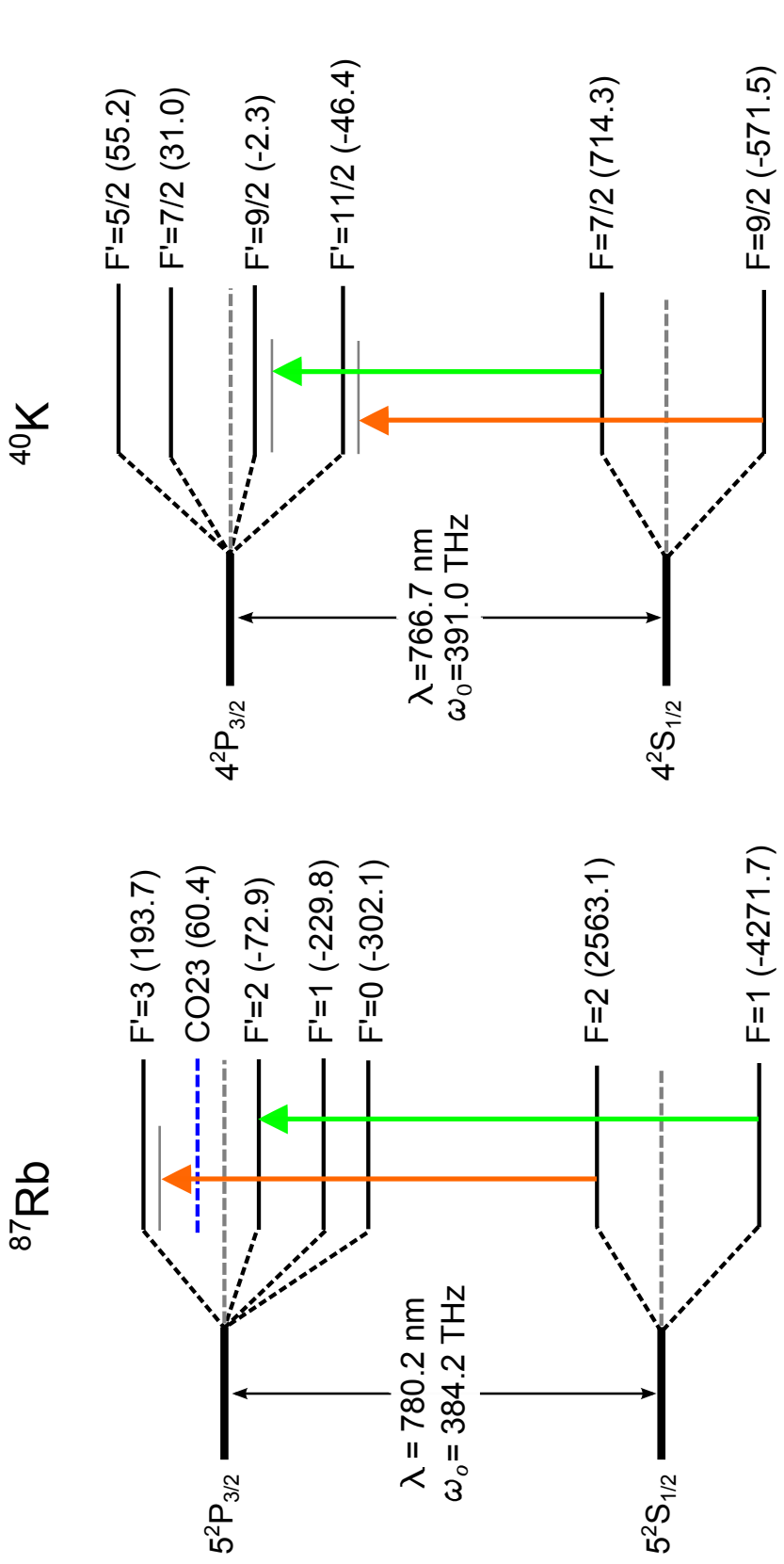

Figure 2.10: *D2 line hyperfine structure for ^{87}Rb and ^{40}K* . The relative hyperfine shifts to scale within each hyperfine manifold (gray dashed line) are shown in MHz. The wavelengths λ and the transition frequencies ω_0 are also presented. The crossover transition between $|F = 2 \Longrightarrow F' = 2\rangle$ and $|F = 2 \Longrightarrow F' = 3\rangle$ for rubidium is shown in dashed blue line and is use for looking the ^{87}Rb master laser. The orange arrows represent the cooling transitions, and the green arrows the repumper ones. The cooling transitions and the potassium repumper transition have been red detune (gray lines) from the main transitions. The numerical values for ^{87}Rb are taken from [63] and for ^{40}K from [58].

Offset Lock Module

The *offset* module (fig. 2.11) has a distributed feedback (DFB) laser diode containing an integrated grating structure emitting in single mode with a line width in the range of MHz. This module uses

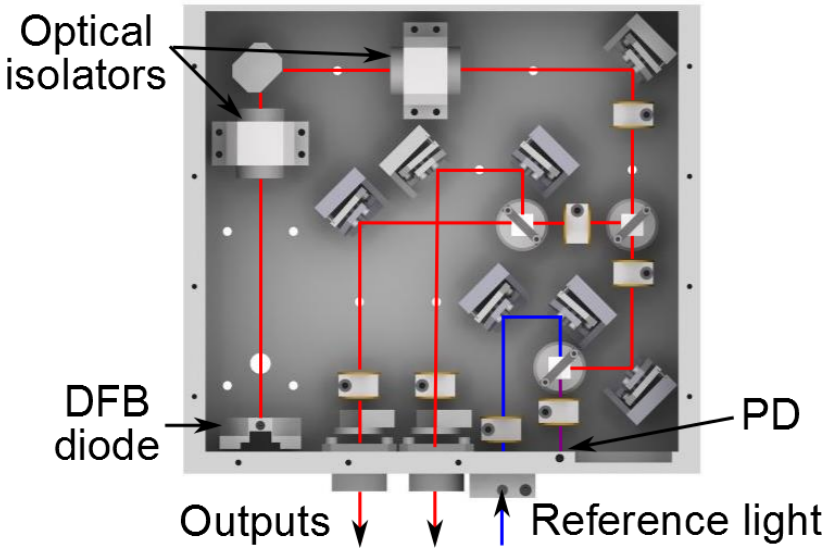

Figure 2.11: *Offset module.* At the bottom left light is generated by a distributed feedback (DFB) laser diode. Light passes through a pair of optical isolators before it is split by a polarising beam splitter and a $\lambda/2$ wave plate in two beams. The deflected beam is split and coupled into fibres. The transmitted beam is combined with the reference light (blue). The reference light comes from the master module. The combined beam (purple) passes through a polariser to make the light interfere and produces the beat signal detected by a fast photodiode (PD).

a method to lock the frequency called offset locking [64]. Experimentally, a beat note is generated by combining part of the light of the reference laser (master laser) with part of the laser light that is going to be frequency stabilised (slave laser) on a photodiode. The servo system ensures a fixed frequency offset to the master laser by locking the frequency of the beat note to a constant value. The offset locked frequency can be tuned up to 120MHz with a voltage controlled oscillator (VCO) that is part of the beat signal processing electronics. A weak spot of this technique is the shifting speed of the frequency, in this case limited by the analogue electronics of the locking system that takes $\sim$ 10ms to tune $\geq$ 60MHz. This is in general not a problem, it just becomes noticeable when detection is performed after loading the 3D MOT, giving a lower signal of the atom cloud. This weakness has been engaged in two different ways. By implementing a beat signal processing

based on digital electronic in a parallel project [65,66] and by modifying the computer control input format. The second method is discussed in more detail on sect. 2.6.

Two offset modules are needed for each species, one for the cooling light and the other for the repumping light. In principle the four offset modules are the same, the only differences are the stabilised frequencies that should satisfy table 2.1 and figure 2.10.

2.3.3 Amplification

Each amplification module (fig. 2.12) uses a tapered amplifier (TA) that consists of an index-guided straight section and a gain-guided tapered section. Both facets are anti-reflection (AR) coated. A TA amplifies the power of the seed laser without modifying the frequency of the light. But a broadening of the linewidth is expected by amplified spontaneous emissions [67]. The TAs are

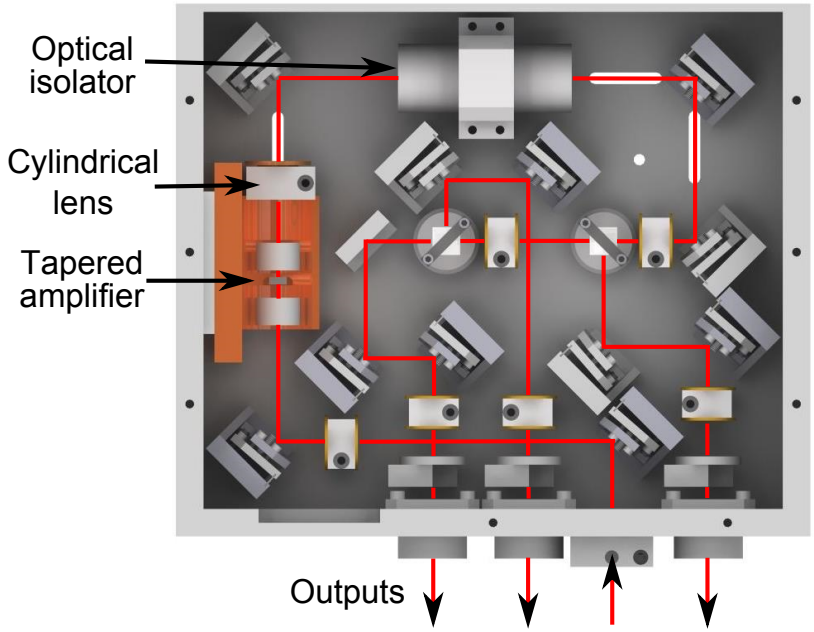

Figure 2.12: *Amplification module.* Frequency stabilised light coming from a offset module is seeded into the amplification module. The light is focused by a lens onto the tapered amplifier. Afterwards amplified light is collimated with a spherical lens and a cylindrical lens in order to correct the astigmatism of the outcome beam. Collimated light passes through an optical isolator and is split into three beams that are fibre coupled.

seeded by the offset lock modules. The seed laser is focused down into the narrow straight section and the laser light is emitted at the facet of the tapered section. The outcome beam needs to be

recollimated since the tapered section induces divergence and astigmatism on the beam. This is done with a combination of lenses, a spherical lens for collimation and a cylindrical lens to correct the divergence and astigmatism. The emission of the TA lasers is amplified as a function of the current going through the TA.

The manufacturers specify an amplification up to 1W and 1.5W, for 780nm and 767nm respectively, with a seeding power of 50mW and with the TA running at a maximum current of 3A. Unfortunately the DFB diodes output power is in the range of tens of mW that is after fibre couple leading into seeding powers of $\approx$ 10mW. Being far bellow the specified seeding power leads into amplification powers of 0.8W to 1W. After fibre coupling the output power is $\sim 40 - 50\%$ of the amplification. The cooling light power that reaches the experiment is not enough for the laser cooling for the 2D MOT and 3D MOT. This problem is solved by taking advantage of the laser system organisation and modularity by adding a second TA for cooling light to the system. This module is seeded by the previous cooling TA and is used to feed exclusively the 3D MOT distribution module (fig. 2.8). In total each laser system has three identical TA modules.

2.3.4 Combination and distribution

After the frequency stabilisation and amplification, the cooling and repumping lights are combined and distributed into the number of fibres needed at the experiment. Table 2.2 lists the number of fibres needed for 2D MOT, 3D MOT and pushing-pumping-detection. It also shows the power supplied for ^{87}Rb . In the case of the 2D MOT and 3D MOT the total power summed over all fibres is shown. These modules (fig. 2.13) are mainly composed of passive optical components, only the acousto-optic modulators (AOMs) are controlled electronically and are used for fast switching and frequency shifting. Additionally shutters have been implemented to block any light leakage from the AOM. There is a module for each stage: 2D MOT, 3D MOT and pushing-optical pumping-detection. These modules have common characteristics, the double path AOM for cooling and repumping light and the combination of both lights. Their main difference is the number of output fibres. As table 2.2 shows 2D MOT , 3D MOT and detection modules have two, six and three output fibres respectively.

Part of the exp.	No. of fibres	purpose of light	power [mW]
2D MOT	2	cooling &	≈ 80
		repumping	≈ 25
3D MOT	6	cooling &	≈ 70
		repumping	≈ 6.0
2D MOT	1	pushing	< 0.10
3D MOT	1	optical pumping	≈ 0.25
3D MOT or SC	1	detection	≈ 0.10

Table 2.2: Summary of the number of fibres and the purpose of the light required at the experiment. The power shown is the total power of the light going to the experiment for ^{87}Rb .

An AOM, as its name implies, is a modulator using sound waves to shift the frequency of light. It is constructed of a quartz crystal with a piezo-electric transducer (PZT) attached to it. The PZT is driven with a radio frequency (RF) signal that produces sound waves in the crystal (phonons). Exchanging phonons between the crystal and the incoming light produces diffraction of the light in different orders and frequency shift. The efficiency of each order depends on the alignment and the incidence angle θ.

The AOM is used in a double path configuration (fig. 2.14) shifting the frequency twice. The alignment for this configuration does not change with the detuning of the driving frequency of the AOM. This is an advantage over the single path configuration where it does change with the detuning.

Alignment of a double path AOM (fig. 2.14): In order to clarify the working principle of the alignment, a step by step description of the alignment process for an AOM is given:

- All the elements that require a precise incidence angle such as AOMs and fibre couplers are preceded by a pair of adjustable mirrors ensuring full control over the direction of the beam. For the AOM the condition is to hit the crystal (front and back surfaces) in the middle with the laser beam.

- With the AOM driver it is possible to attenuate and to tune the signal going to the AOM. The AOMs are adjusted to have a central peak at 80MHz and a power of 1W (30dBm). In

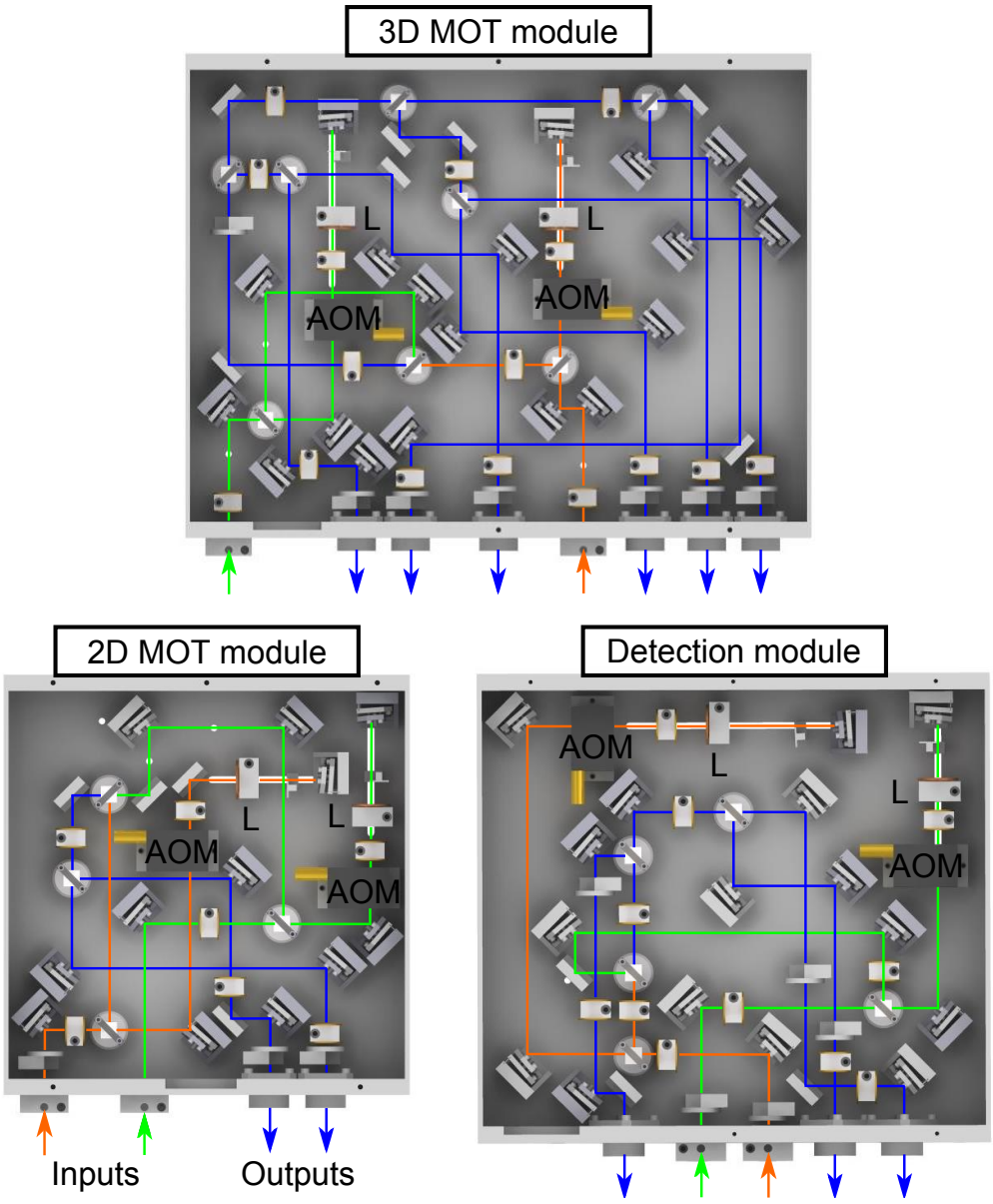

Figure 2.13: *Combination and distribution modules.* This picture shows the three modules making up the combination and distribution part of the laser system. Each of them has two inputs, cooling light (orange) and repumping light (green). Cooling and repumping light pass individually through a double path AOM configuration (fig. 2.14) and get combined on a polarizing beam cube. The combined light (blue) is then distributed into fibres. Each module has different number of output fibres. The 3D MOT, 2D MOT and detection modules have six, two and three output fibres respectively.

order to reach this power a 40dB amplifier is needed. When the AOM driver is turned on the beam is diffracted. The 0^{th} order is the un-deflected beam, and is always visible when the

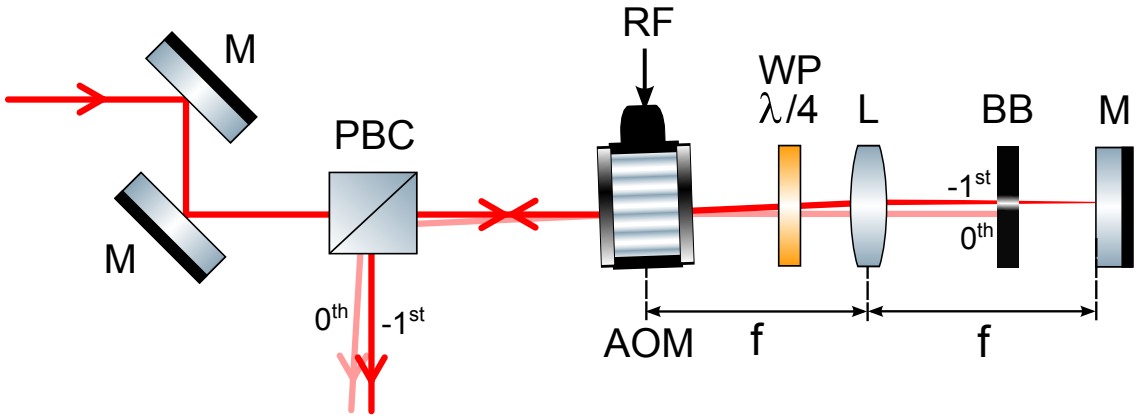

Figure 2.14: *AOM double path configuration.* Incoming light from the left is reflected by two adjustable mirrors (M) that are used to align the beam to hit the center of the quartz crystal inside the AOM. The light passes through a polarising beamsplitter cube (PBC) and the AOM. The AOM is driven with a 80MHz RF signal. The diffracted beam is optimised for the -1^{st} order. A lens (L) is placed behind the AOM at a focal distance f from the middle of the AOM. A quarter wave plate ($\lambda/4$) is placed between AOM and lens. A beam block (BB) is used to block the 0^{th} order of diffraction letting the -1^{st} order pass. The reflecting mirror is placed at a distance f from the lens to reflect and then re-collimate the beam when it passes through the lens for the second time. After the beam gets a total shift of $\lambda/2$ in polarization and it is reflected on the PBC. At the end the light frequency has been shift by -160MHz.

AOM driver is off.

- The diffraction of the beam is adjusted by slightly turning the AOM which effectively changes the incidence angle. In our setup, the AOM is fixed such that the -1^{st} order is maximised, with 80% to 90% of the light going into this order. The position of the beam can be readjusted to hit the middle of the apertures.

- A lens L is placed after the AOM at a distance f (focal length $\sim 40-50$mm) from the center of the AOM. All visible orders should become parallel to each other. Finer adjustment of the lens position can be done if you can verify the parallelism of the different orders by checking the separation of the beam centres through a long distance. This is normally difficult since the lens also changes the beam size along the path. The good positioning of the lens is the part that makes double path alignment insensitive to frequency variations. Since the frequency detuning produces a variation on the diffraction angles, and this configurations is independent to the angular variations of the different orders.

- An adjustable mirror is placed at distance f after the lens (back mirror). This mirror has the purpose of reflecting the light as well as re-collimating the -1^{st} order beam. The collimation criteria is that the size of the beam remains unchanged after it passes through the lens for the second time. A small change of the beam size for a long distance ($\sim$ 3m) is sufficient for this alignment since the beam path inside of the module is less than a meter. Obtaining the matching beam size[6] is extremely important to achieve good coupling efficiencies for the output fibres.

- In order to avoid interferences between the different orders, a beam block for all the orders except the -1^{st} order is placed between the lens and the mirror. The back mirror is adjusted to have the same path in the way back. Changing the height adjustment at the back mirror is possible to see a beam pattern with a single dot for the going beam and a group of different orders corresponding to the reflected beam. By changing the back mirror adjustment on the left-right direction the desirable order is optimised.

- A quarter wave plate ($\lambda/4$) is placed between AOM and lens to produce a $\lambda/2$ shift in polarization of the light. This is needed for redirecting the beam with a beam splitter after its frequency has been shifted.

- Finally, measurement of the output-input power ratio to verify an efficiency of 64% or higher as a result of the double path is done.

2.3.5 Recombination

The laser system was planned for two sets of vacuum chambers for separate species at the experiment. At the current experiment status only one chamber exist so it raises the necessity of combining the light for both species. *Fibre splitters*[7] that have two inputs and two outputs are implemented. In these fibres one side of the cladding has been polished without disturbing the core region. The link between two polarisation maintaining fibres is done by placing the two polished fibre in optical contact with the polarisation axis aligned. The coupling of the light is done by

[6]The beam diameter specified for the couplers is 0.81mm at $1/e^2$-value of Gaussian intensity distribution.
[7]Evanescent Optics Inc. Polarization splitters, part number 968P.

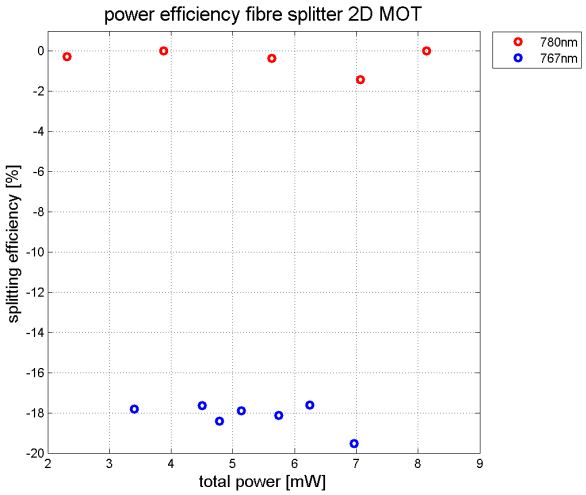

Figure 2.15: *Power distribution efficiency for fibre splitter.* The plot shows the splitting efficiency for 780nm (rubidium) and 767nm (potassium) at different input powers. The splitting efficiency is defined as the difference between the normalized outputs. A splitting efficiency of 0% implies a splitting power of 50/50 between the outputs that is the case for 780nm. On the other hand splitting efficiency of -18% implies splitting of 41/59 for 767nm.

evanescent wave interaction from core to core [68]. To ensure that the fibres remain in contact substrate blocks are loaded around the join.

These fibre splitters are used to combine the ^{87}Rb and ^{40}K lights for the 2D MOT and 3D MOT. The use of this splitters reduces the number of output fibres required from the 2D MOT and 3D MOT modules to half. In the case of the 2D MOT one input of the fibre splitter is connected to the potassium 2D MOT module and the other one to the rubidium 2D MOT module. As a result of the recombination each output fibre is carrying 4 different frequencies (2 cooling and 2 repumping lights). A similar process is done for the 3D MOT modules, with the implementation of three 2x2 fibre splitters the six beams required for the 3D MOT (tab. 2.2) are produced.

The specifications of the fibres given from the company [68] are: polarisation maintaining and ratio tolerances of $\pm 3\%$ for 50/50 splitting for 780nm light. The 2D MOT fibre splitter was tested for both wavelength (780 and 767nm) with different input powers. Results are shown at figure 2.15. The graph shows the splitting efficiency versus the total power. The splitting efficiency is defined as the differences of the two output intensities divided by the average intensity of both beams. From here it can be concluded that the splitting efficiency for 780nm (rubidium) is in the range of the

manufacturing specification, since the splitting efficiencies are close to zero, which means 50/50 splitting. In contrast, the splitting for 767nm (potassium) is not as even. A splitting efficiency of -18% implies a splitting power of 41/59. A non-even splitting for 767nm was expected since the fibre splitter were optimised for 780nm.

2.4 Magnetic trapping and transport

Magnetic trapping for neutrons was first proposed by Vladimirskii [69] in 1961 and for quantum dipoles by Heer [70] in 1963. The first experimental observed of magnetic trapping for neutral atoms was in 1985 in a quadrupole trap [22]. After that, different types of magnetostatic traps used before for neutrons and plasma have been studied [21,71] with the purpose of using them for neutral atoms. Even after the study of different trap configuration, the first two BECs were produced in traps derived from a quadrupole trap [1,2].

The necessity of magnetic trapping comes from different requirements at the experiment. First of all a magnetic gradient of ≈ 15G/cm is needed for the magneto-optical trap. After laser cooling, the atoms have reached temperatures of $\sim 100\mu$K and in order to reduce further the temperature RF induced evaporative cooling [17] in a magnetic trap is applied. Magnetic trapping is also used to transport the atoms between chambers (≈ 150G/cm). Therefore different magnetic traps are built (sect. 2.4.2). In the following magnetic trapping principles are introduced.

2.4.1 Magnetic trap principles

The trapping of an atom with magnetic dipole moment $\overrightarrow{\mu}$ is possible since an inhomogeneous magnetic field $\overrightarrow{B}$ exerts a force $\overrightarrow{F}$ on the atoms

$$\overrightarrow{F}(\vec{r}) = \overrightarrow{\nabla}(\overrightarrow{\mu} \cdot \overrightarrow{B}(\vec{r})). \tag{2.7}$$

The interaction of magnetic dipole with an external magnetic field is given by $U_B = \overrightarrow{\mu} \cdot \overrightarrow{B}$. In the presence of the magnetic field $\overrightarrow{B}$ the potential energy of the atom is given as

$$U_B = g_F m_F \mu_B |\overrightarrow{B}| \tag{2.8}$$

where g_F is the Lande g-factor, m_F the quantum number of the z-component of the angular momentum F and μ_B is the Bohr magneton. Depending on the orientation of the dipole moment relative to the local magnetic field, the atom is drawn into the region of high magnetic field (*high-field seekers*, $g_F m_F < 0$), or low magnetic field (*low-field seekers*, $g_F m_F > 0$). Since a local maximum cannot exist in free space [72] traps with a local minimum are used. Discussion and description of different trapping potentials for neutral atoms can be found in [21]. Here the description of a quadrupole trap is given.

The quadrupole trap is one of the simplest and commonly used magnetic trap in the cold atoms field [12,14,21]. It is formed by two identical coils on the same symmetry axis. The current flowing trough the coils is equal in magnitude but opposite in direction. This layout is known as anti-Helmholtz configuration. A polynomial expansion of the magnetic field for quadrupole trap is given in [21], and near to the center of the trap the magnetic field can be approximated by [73]

$$|\overrightarrow{B}| = A\sqrt{\rho^2 + 4z^2} \tag{2.9}$$

where $\rho^2 \equiv x^2 + y^2$ and the magnetic field gradient $A = \frac{\partial B}{\partial \rho}|_{r=0}$ is constant. From eq.(2.9) can be concluded that at the center of the trap the magnetic field is zero and that the magnetic field gradient is twice as strong in the axial direction z than in the radial direction ρ. Also the magnetic field magnitude increases linearly away from the center.

The potential energy of an atom trap in a quadrupole trap can be obtained by replacing the magnetic field $|\overrightarrow{B}|$ eq.(2.9) into the potential energy U_B eq.(2.8), giving as a result

$$U_B = g_F m_F \mu_B \left.\frac{\partial B}{\partial \rho}\right|_{r=0} \sqrt{\rho^2 + 4z^2}. \tag{2.10}$$

The requirement for stable trapping is that the magnetic moment adiabatically follows the magnetic field, meaning the orientation of the magnetic moment with respect to the magnetic field $\overrightarrow{B}$ should not change. This condition is satisfied when the rate of change of the field's direction θ is slower than the precession ω_{Larmor} of the magnetic moment around the magnetic field vector [12]

$$\frac{d\theta}{dt} < \omega_{Larmor} = \frac{\mu|\overrightarrow{B}|}{\hbar}, \tag{2.11}$$

where the upper boundary for $\frac{d\theta}{dt}$ in a magnetic trap is the trapping frequency. In regions of small magnetic fields the adiabatic condition (eq. 2.11) can be violated creating a region of trap loss due to spin flips to an untrapped state. These losses are known as Majorana losses [24]. This phenomenon becomes more pronounced when the atoms spend more time in the surroundings of the zero field meaning cold samples will lose more atoms than hotter samples. These losses become significant after RF evaporative cooling is performed and the cloud temperature is $\sim 30\mu$K [35]

Trap depth

A defining characteristic of a magnetic trap is the trap depth. This is defined as the maximum temperature corresponding to the fastest atom inside of the trap and is determined by magnetic gradient B' and the constrain size of the vacuum chamber[8] (d_x, d_y, d_z) as [74, 75]:

$$U_0^x = (g_F m_F \mu_B B'_\rho) d_x/2 \tag{2.12}$$

$$U_0^y = (g_F m_F \mu_B B'_\rho - mg) d_y/2 \tag{2.13}$$

$$U_0^z = (g_F m_F \mu_B B'_z) d_z/2 \tag{2.14}$$

$$T_{depth} = U_0/k_B. \tag{2.15}$$

where $B'_\rho = \partial B/\partial\rho|_{r=0}$ and $B'_\rho = \partial B/\partial z|_{r=0}$ are the magnetic gradients along the ρ and z axes respectively. Also,ca it is assumed that the center of the magnetic trap coincides with the middle of the chamber and the gravitational field acts along the y axis, with m the atom mass and g the

[8]Since the atom cloud is inside of a vacuum chamber, the cloud can not occupy a volume larger than the inner dimensions of the chamber.

acceleration of gravity.

Considering that the magnetic gradient along the axial direction z is twice as strong as the radial direction ρ, thus the trap depth in z direction is twice as deep if the vacuum chamber dimensions are the same. The trap depth also depends on the chamber size (d_x, d_y, d_z), which in some cases is tighter in the axial direction than the radial direction making the trap shallower in the shortest direction. Consequently the trap depth is defined as the smallest trap depth. For the current experimental setup, the smallest trap depth in the 3D MOT chamber is along the z axis and for the science chamber is along the y axis.

Magnetic transport

Moving the magnetic field produces transport of the atoms. There are two common approaches to transfer atoms between chambers. The first is done by overlapping a series of quadrupole traps and transferring the atoms from one trap to another successively [76]. The second approach uses a single quadrupole trap that is moved mechanically [27, 32, 77–79]. The main drawbacks of using overlapped coils are the necessity of an optimised current switching, as well as building many sets of coils. On the other hand moving quadrupole field requires a transport medium (mechanical rail). In both cases a set of magnetic traps in each 3D-MOT system to hold the clouds before they get combined is needed. The chosen method for this experiment is the second one. This choice implies a thin vacuum chambers (sect. 2.1) and coils in order to avoid high power consumption of the transport coils.

2.4.2 Magnetic traps at the experiment

In the experiment the magnetic trapping is done with quadrupole traps. Three different sets of coils are used: 3D MOT, transport and Feshbach coils. These coils are mounted in a two layer configuration (fig. 2.1) where the inner layer is formed by the 3D MOT and Feshbach coils and the outer layer by the transport coils [35].

The 3D MOT coils provide the flexibility of individual magnetic trapping at each 3D MOT chamber for laser cooling and magnetic trapping. And with the help of the transport coils the

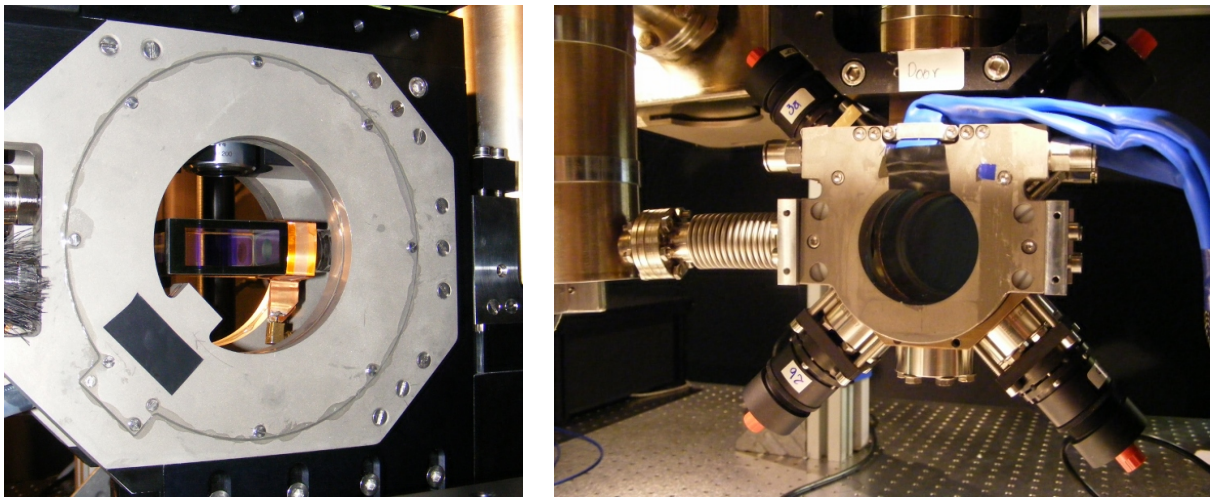

Figure 2.16: *Inner layer of the coils system.* On the left the Feshbach coils are mounted closely to the science chamber. The Feshbach coils are designed for an excellent optical access to allocate different sets of beam in the science chamber, among them detection, dipole trap and optical lattices. On the right the 3D MOT coils are mounted on the 3D MOT chamber. These allow optical access for the horizontal 3D MOT beam and for detection.

cold atom cloud is moved between chambers (3D MOT $\Longleftrightarrow$ science chamber). The Feshbach coils have been optimised to produce a homogeneous magnetic field at the science chamber with the purpose to modulate the atomic interaction via Feshbach resonances [46]. These coils are also used as a magnetic trap in anti-Helmholtz configuration. The 3D MOT and transport coils have been optimised to produce a magnetic gradient of 150G/cm with a maximum current upto 100A for magnetic trapping.

To provide good optical access and low power consumption the coils are mounted as close as possible to the chambers. In the case of the 3D MOT coils they are mounted directly to the chamber (fig. 2.16 right) allowing optical access for the MOT telescope and detection systems. The Feshbach coils (fig. 2.16 left) are surrounding the science chamber leaving enough optical access to allocate the dipole trap, optical lattice beams and horizontal detection.

New coil design

A new coil design (fig. 2.17) was developed for the coils by Meyer [35]. These coils were designed to generate high magnetic gradients whilst being compact and with high optical access. These

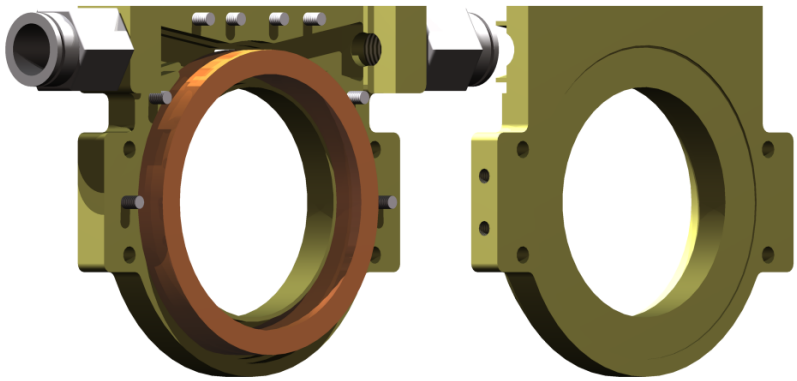

Figure 2.17: *3D MOT coil design.* On the left the drawing shows half of the cooling body (green) with the coil (copper) attached to it. On the right the second half of the cooling body.

Parameters	**3D MOT coils**	**Transport coils**	**Feshbach coils**
N	20	100	70
D[mm]	55	96	56
R[mm]	30.71	85.32	56.68
B'_z[G/cm] @ 100A	165.6	153.7	234.4
B[G] @ 99A	-	-	1100

Table 2.3: *Coils parameters.* This table presents the characteristic parameters for the three sets of coils: 3D MOT, transport and Feshbach. The coil parameter are N: number of windings, D: distance between pair of coils and R: radius of the middle winding. The results of the simulation of the magnetic gradient B'_z along the strong axis and the magnetic field B with the given coil parameters is also presented. More details can be found in [35].

coils are made of copper foil to favour the high current density and compact design. Different coils parameter and results of the simulations of the magnetic field and gradient are presented in table 2.3. Further improvements to the Feshbach coils design have been done in [36].

The copper foil used for the coils has a cross section of 12.7mm width and 0.254mm height. In order to isolate the different windings one side of the cooper foil is coated with a thin Kapton layer of 25.4μm thickness. Neighbouring windings are glued together[9].

In order to dissipate the heat produced by the coils a cooling system is implemented. The best way to cool the coils is by direct contact with the cooling element, usually water. The coils have a

[9]Resintech Ltd epoxy resin RT151

voltage drop of $15-30$V across them which is enough to produce electrolysis in the water, therefore oil is used instead. The coil contact surface with the cooling oil has been treated in order to get a better heat transfer. Part of this treatment is the machining and etching of the surface to flatten it and remove short circuits respectively. The cooling system consists of a pump, cooling oil, a heat exchanger and a reservoir. More information about the cooling system can be found in [33].

2.5 Optical dipole trap

Different approaches to overcome the Majorana losses have been developed on the cold atoms field. Some of these techniques rely on producing traps with non-zero magnetic field such as the time-averaged orbiting potential (TOP) trap [1,23] and the Ioffe-Pritchard trap [21]. Another technique is the optically plugged quadrupole trap [2,26,27] using a repulsive optical potential to push the atoms away for the zero magnetic field of the quadrupole trap. A similar hybrid trap can be produced with a magnetic trap and an attractive dipole trap [28,80,81] where the atoms that escape from the magnetic trap are recaptured by the dipole trap. By applying inductive RF evaporative cooling [17] in any of the aforementioned traps BEC can be reached. But since the BEC is wanted in a quasi-2D regime another approach is used in this experiment.

Quasi-2D system can be generated with different configurations of optical dipole traps [33]. Among them are blue detuned interference trap, red detuned interference trap, cylindrical lens trap and astigmatic lens trap. A comparison between these traps is presented in [33] and it has been concluded that the more suitable dipole trap for this experiment is the astigmatic lens trap for its simplicity in building and alignment, as well as its physical features. The astigmatic dipole trap is described in section [2.5.2]. In the following the dipole trapping principles are presented.

2.5.1 Dipole trapping

The follow derivations and calculation are based on [82]. When an atom is placed into laser light, the electric field $\vec{E}$ induces a dipole moment $\vec{d}$ given by

$$\vec{d} = \alpha \vec{E}, \tag{2.16}$$

where α is the complex polarisability of the atom which depends of the driving frequency ω_L.

The interaction potential of the induced dipole moment in the presence of the driving field $\vec{E}$ is then

$$U_{dip} = -\frac{1}{2}\left\langle \vec{d}\cdot\vec{E}\right\rangle = -\frac{1}{2\epsilon_0 c}\Re(\alpha)I, \tag{2.17}$$

where $I = 2\epsilon_0 c|\vec{E}|^2$ is the field intensity, $\langle\cdots\rangle$ denotes time average. In order to obtain the second equation, the dipole moment $\vec{d}$ is replace with equation (2.16), and after averaging over time and applying the rotating wave approximation[10] the second expression is deduced. From this equation it can be concluded that the potential energy is proportional to the intensity of the laser light and to the magnitude of the real part of the atom polarisability. The dipole force can be written in terms of the dipole potential as

$$\overrightarrow{F}_{dip}(\vec{r}) = -\nabla U_{dip}(\vec{r}) = \frac{1}{2\epsilon_0 c}\Re(\alpha)\nabla I(\vec{r}). \tag{2.18}$$

From equation (2.18), it can be seen that the dipole force is proportional to the intensity gradient of the driving field and to the real part of the polarisability α.

The scattering rate Γ_{sc} is an indicator of the heating of the atoms produced by the dipole trap and can be written in terms of the intensity of the driving field as

$$\Gamma_{sc}(\vec{r}) = \frac{1}{\hbar\epsilon_0 c}\Im(\alpha)I(\vec{r}), \tag{2.19}$$

Assuming the simplest atom level scheme, a two level atom with an optical transition ω_0, an expression for the dipole potential and scattering rate can be written as

$$U_{dip}(\vec{r}) = -\frac{3\pi c^2}{2\omega_0^3}\left(\frac{\Gamma}{\omega_0-\omega_L}+\frac{\Gamma}{\omega_0+\omega_L}\right)I(\vec{r}), \tag{2.20}$$

$$\Gamma_{sc}(\vec{r}) = \frac{3\pi c^2}{2\hbar\omega_0^3}\left(\frac{\omega}{\omega_0}\right)^3\left(\frac{\Gamma}{\omega_0-\omega_L}+\frac{\Gamma}{\omega_0+\omega_L}\right)^2 I(\vec{r}), \tag{2.21}$$

where Γ is the atoms natural linewidth and c is the speed of light. If the driving field is near

[10] In the rotating wave approximation the fast oscillating terms $(\omega_0+\omega_L)$ are neglected.

resonance $\omega_L/\omega_0 \approx 1$ by applying the rotating wave approximation the previous expressions can be written in terms of the detuning ($\Delta \equiv \omega_L - \omega_0$) between the driving field and the atom optical transition ω_0 as

$$U_{dip}(\vec{r}) = \frac{3\pi c^2}{2\omega_0^3}\frac{\Gamma}{\Delta}I(\vec{r}), \tag{2.22}$$

$$\Gamma_{sc}(\vec{r}) = \frac{3\pi c^2}{2\hbar\omega_0^3}\left(\frac{\Gamma}{\Delta}\right)^2 I(\vec{r}). \tag{2.23}$$

From this potential can be deduced that atoms are driven to maxima intensity region when the laser light is red detuned ($\Delta < 0$) and to minimum intensity region when the laser light is blue detuned ($\Delta > 0$). And from the scattering rate expression can be deduced that bigger detuning is favourable to reduce heating by the dipole trap.

2.5.2 Astigmatic dipole trap

To create a quasi-2D trap the confinement in one of the axis (y vertical direction) is much stronger than in the other two axis x and z. This condition is satisfied when the chemical potential μ of the atom cloud is lower than the first excited state of the harmonic oscillator in the tight direction such as $\mu \sim k_B T < \hbar w_y$ [80]. For a reasonable low temperature of $100nK$ the trapping frequency w_y should be $2\pi\cdot$2.6KHz or higher [33] to satisfy the previous condition.

The astigmatic dipole trap is produced with a single collimated beam propagating in the z direction that passes trough a combination of an achromatic doublet lens f_a and a cylindrical lens f_c [83]. The spherical lens focuses the beam down and the cylindrical lens shifts the positions of the vertical f_y and the horizontal f_x foci depending on the focal lengths and the separation between lenses d as

$$f_y = f_a, \qquad f_x = \frac{f_a f_c}{f_a + f_c - d}, \tag{2.24}$$

where the cylindrical lens is mounted in such a way that the vertical direction of the beam is unaffected.

The intensity profile of this trap can be expressed in a similar way as a Gaussian beam in terms

of the beam waists (ϖ_x, ϖ_y) as [33, 83]:

$$I(x,y,z) = \frac{2P_0}{\pi \varpi_x(z)\varpi_y(z)} \exp\left(-\frac{2x^2}{\varpi_x^2(z)} - \frac{2y^2}{\varpi_y^2(z)}\right), \tag{2.25}$$

with horizontal and vertical waist,

$$\varpi_x(z) = \varpi_{x,0}\sqrt{1+\left(\frac{z-\Delta z}{z_R}\right)^2}, \tag{2.26}$$

$$\varpi_y(z) = \varpi_{y,0}\sqrt{1+\left(\frac{z}{z_R}\right)^2}, \tag{2.27}$$

where P_0 is the power in the laser beam, $\varpi_{x,0}$ and $\varpi_{y,0}$ are the beam waist at the foci f_x and f_y respectively, $z_R = \pi\varpi_0^2/\lambda$ is the Rayleigh range and $\Delta z = f_x - f_y$ is the separation between foci.

The dipole potential produced by this intensity profile can be approximated as a harmonic potential U_{Harm} in the vicinity of the foci, so the trapping frequencies ω_i can be calculated from the second derivative of the potential as [83]

$$\omega_i = \sqrt{\frac{1}{m}\frac{\partial^2 U_{Harm}}{\partial\, i^{\,2}}}; \quad \text{with} \quad i = \{x,y,z\}. \tag{2.28}$$

2.5.3 Optical system for the astigmatic dipole trap

The laser used for the dipole trap is a commercially available 1550nm laser that can be amplified with also a commercial amplifier up to 10W. The laser system for the dipole trap, in a similar way to the laser system for laser cooling, produces, amplifies and distributes laser light to the experiment. The 1550nm laser light coming from a commercial photodiode[11] is fed into a one-to-three distribution module where it is divided into two beams that are amplified by fibre amplifier[12]. Amplified light passes through a single pass AOM (which is used for fast switching) and is back coupled into a high power fibre that goes to the experiment.

At the experiment the optical system for the dipole trap (fig. 2.18) is formed of a collimation

[11] Thorlabs, 1550nm laser diode SFL1550S
[12] Nufern, fibre amplifier NuAMP-1550

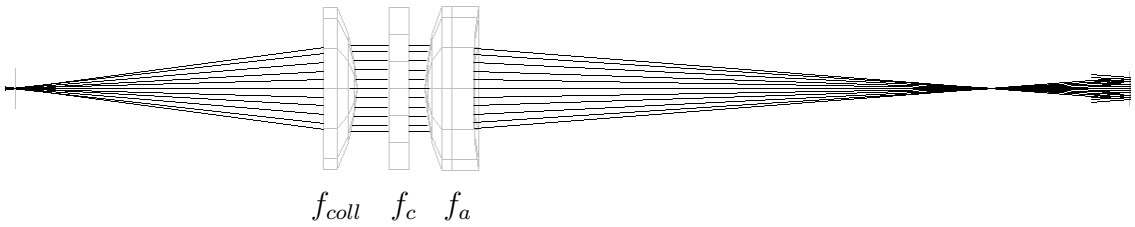

Figure 2.18: *Dipole trap optical system.* 1550nm laser light coming from dipole trap laser system is fed to the optical system trough a hight power fibre and is collimated by an aspheric lens f_{coll} = 100mm. After collimation light passes trough the lens system formed by a cylindrical (f_c = 10m) and achromatic doublet lens (f_a = 200mm) where the astigmatism and the focusing of the light is generated. The optical system is mounted in a three-dimensional (XYZ) translation stage for fine positioning of the dipole trap.

lens[13] (f_{coll} = 100mm) and a lens system formed by a cylindrical lens[14] (f_c = 10m) and an achromatic doublet lens[15] (f_a = 200mm) that focuses and induces the astigmatism on the laser beam respectively. The optical system is mounted on an optical bench which in turn is mounted on a three dimensional translation stage for accurate positioning of 5μm in each direction.

Replacing the focal distances of the cylindrical f_c and achromatic doublet f_a lens in equation (2.24) and using a spacing between lenses of $d = -20$mm is deduced that the vertical foci f_y is at 200mm from the achromatic doublet lens and the horizontal foci f_x is at 196mm. It is chosen to have a minimum beam waist of $\varpi_{x,0} = \varpi_{0,y} = 10\mu$m. Replacing this values at equation (2.26) and equation (2.27), it can be concluded that at the vertical foci the beam waists are $\varpi_y(0) = 10\mu$m and $\varpi_x(0) = 395\mu$m (fig. 2.19) and vice versa for the horizontal foci. At a maximum power of 10W the dipole trap depth is calculated numerically to be 300μK for ^{87}Rb. Additionally the trapping frequencies are calculated numerically and are equal to $(\omega_x, \omega_y, \omega_z) = 2\pi \times (300, 4900, 110)$Hz, at the maximum power of 10W. As a result of the confinement frequencies the atoms cloud trap in the dipole traps is in a quasi-2D system.

[13] Asphericon, aspheric lens SPA 50-100 LPX-C
[14] CVI laser optics, cylindrical lens SCZ-50.8-1000.0-C-1550
[15] Thorlabs, achromatic doublet lens AC508-200-C

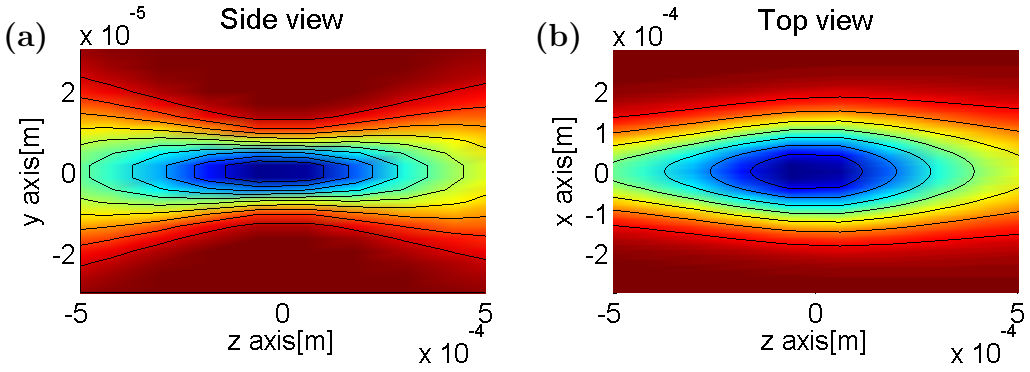

Figure 2.19: *Dipole trap vertical foci views.* This pictures shows the dipole trap foci along the y axis from different views with (a) the side view and (b) the top view. The beam propagates along the z axis. The vertical waist y is the smallest and equal to 10μm. The waist horizontal waist x is bigger and equal to 395μm.

2.5.4 Dipole trap at the experimental

The dipole trap is set up to produce a quasi two dimensional confinement on the vertical direction for the BEC in the science chamber and it has been mounted at an angle (fig. 2.1).

The dipole trap is placed below the zero quadrupole field. It is turned on while RF evaporative cooling is performed in order to recapture the cold atoms that had escaped through the zero of the quadrupole field. When the Majorana losses from the quadrupole trap become more critical and the atoms are cold enough, they are transferred to the dipole trap by slowly reducing the quadrupole field.

Evaporative cooling is also performed in the dipole trap by reducing the intensity of the laser beam [30]. More details about the traps used to produce a BEC are given at chapter 5.

2.6 Computer control

In order to synchronise parts of the experiment to the required precision a computer control is needed. The experiment requires a highly stable and reliable control that ensures repeated production of same sequence when the same commands are executed. Control over digital, analogue and VISA (virtual instrument software architecture) channels is required. Short time periods are

desired in some stages of the experiment e.g. detection ($\sim 50\mu$s).

The computer control was designed and developed by Baumert [33] and Kronjaeger (post-doctoral in charge). The author of this thesis has worked on the computer control to add past slots and the protocol ID. In this section a general overview of the computer control and its component is introduced. A more detail explanation of the design of past slot and the importance of the protocol ID is presented.

2.6.1 Computer control overview

The computer control is formed of three main parts: the front end, the PXI controller and the FPGAs (field programmable gate arrays[16]). Each of this parts executes a specific labVIEW program. The front end is the interactive part of the computer control, and is where the sequences for the experiment are written. The PXI controller is called when a sequence is ready. The sequence is sent to and stored in the PXI and is fed to the FPGAs for execution. Detailed information about FPGAs and PXI controller can be found in [33]. A brief description of the FPGA and PXI is given here and a more elaborate description of the front end is given later.

Digital and analogue channels are controlled by a pair of FPGAs. Each FPGA controls 8 analogue outputs with an independent update rate of 1MHz, an output voltage from -10V to 10V and with a resolution of 16-bit. Each FPGA also controls 96 digital channels with a update rate of 40MHz. The update rates give the limitations in the timing of 1μs to the analogue channels and 25ns for the digital ones.

The FPGA are controlled by a computer PXI controller[17] that runs a real-time operating system (RTOS) optimized for speed and reliability. The PXI administrates and processes all data that goes to the FPGAs, as well as controlling other devices running on VISA. The PFGA and PXI programs are static systems that are not modified by the user. In theory, once these programs have been proven and approved there is no need to change them. On the other hand the front end is in constant evolution. New templates are created to be added to an existent sequence or use to produce new ones.

[16] National Instruments NI 7841R
[17] National Instruments NI PXI-8108 RT.

2.6.2 Front end

The front end is the user interface of the computer control which has two parts: the *front end face* and the *front end framework*. The front end face is where the user creates templates and sequences. The front end framework is used to organize the channels by assigning them the appropriate names, default values, calibration values and delays.

The experiment is run by sequences. Each sequence is formed by time slots where specific channels are modified. In order to create a new sequence an initialisation module[18] is added. After the initialisation module the time slots are added, each time slot is defined by time period and the values of the channels that are modified. The digital channel are defined by logical values (true or false), while the analogue channels are defined by the output signal to reach (-10 to 10 V) and whether this value is reach via a ramp or not. The VISA channels are defined with the TCP/IP address and the commands that want to convey. A schematic of this structure can be seen at table 2.4. Once the sequence is finished the transmission module is included, and then this new sequence is sent to the PXI controller, where it is fed and executed by the FPGAs.

Sequence structure

In the creation of a sequence whenever a new time slot is added the values of the digital and analogue channels are filled with the values of the previous slot. The VISA channels need to be execute once, consequently the information is not transmitted to the new slot. Therefore only the called channels are modified in this new slot. Hence the structure of the sequence is consecutive and is divided in time slots.

In order to simplify the monitoring of the sequences, modules have been created, where each modules performs a specific tasks such as: MOT loading, magnetic transport or detection. In MOT loading light and magnetic field have to be on and at specific values. This implies control over digital channels such as AOMs (on/off), shutters, and coils (on/off), and analogue channels as the current through the coils, the detuning of the lasers and the intensity of cooling beams. All this is controlled by a single module, where the variables that are constant can stay in the back and the

[18] The initialisation module sets all channels to their default value, generally off or zero.

Time slot [ms]	1000	2000	3000	...
Digital channels	[T/F]			
1	T	F	T	...
2	T	T	F	
⋮				
191	F	F	T	
Analogue channels	Value[V]/ramp[T/F]			
1	10/F	5/F	3/F	...
2	5/F	0/T	5/F	
⋮				
16	-	2/F	3/T	
VISA channels				
DDS	RF evap.	-	-	...

Table 2.4: Sequence structure and number of channels available. The 192 digital channel is used for data request from the FPGA to the PXI controller.

ones that need adjustment appear in the front face where the user can change them.

Another example of these is the detection module which is simple but needs several time periods in order to be executed. Starting with setting the detection light to resonance, trigger the camera, open detection shutter, close any other shutter, turn off the dipole trap, and so on. This module is shown in table B.1.

Past time slots

The need for past time slot arose from the VCO[19] long shifting time $\sim$ 10ms for 60MHz detuning. This retardation can not be set as delay time of the VCO channel since the shifting time varies with the detuning. The current way to overcome this situation is adding another module that takes care of this delay and any other task that need to be ready before detection is performed. The

[19]The VCO (voltage controlled oscillator) is part of the offset locking electronics and it is the one used to shift the frequency of the cooling light for detection.

advantage of using past time slots is to keep the modularity by enclosing all involved commands in a single module.

Typical sequence

time slot [ms]	100	50	500	100	**new slot**

Past slots new boundary

time slot[ms]	100	50	100	400	100	

time line[ms] 0 100 150 250 650 750

offset time

slot length **past slot**

Table 2.5: *Past slot sketch.* On the top is shown how the common new slot are created at the end of the already build sequence. On the bottom the past slot are shown with the defining times such as offset time and slot length are depicted. In this case the offset time is assumed to be -500ms and a slot length of 400ms. The time line is also shown, where the start and end boundaries are points in the time line.

The past slot have two times: the first one defines how far in the past the slot starts so called offset-time and the second one is the length of the slot (see table 2.5). These times have condition that should satisfy in order to be valid. The offset-time can have a negative[20] or zero value, this condition ensures that is a past slot or just a normal slot. The length of the slot can be zero or positive, this condition ensures that the slot gets annulled or executed. Given these two time values different situations can happen as will be explained later.

First of all one needs to define the time line (see table 2.5) rather the individual periods of time giving a start and end boundary for each time slot. The boundaries at the beginning and end of the new slot need to be created. The boundary position is calculated with respect to the total sequence time. The start boundary for the new past slot has two cases: first case, the boundary coincides with an existing one or second case, the new boundary is located inside an existing time slot. In the first case the changes are easy to implement where just the called channels are modified in all time slot after the boundary. In the second case is more complicated since new boundary needs to be created that implies the division of the respective time slot into two (see table 2.5). The creation of

[20] As a safety feature the off-set time can not be longer then the sequence length.

the new boundary should not affect the uncalled channels. This implies that the division of the time slot keeps the information regarding the old slot. In general the assignation of the channels value in the new time slot should be as simple as copy from the previous slot[21]. This assignation of values become more complicated when the new boundary is on a time slot where analogue channels have ramps activated. This case implies calculating the value of the analogue channel when it reaches the boundary and the ramp should be activated for both new slots.

For the end boundary something similar can happen: 1) the boundary already exists, 2) the boundary is between two existing boundaries or 3) a completely new boundary is created. The last case happens when the slot length is longer than the offset time. The first two cases can be treated in a similar way as the start boundary and the third case is analogous as the old creation of time slots with the added slot length is equal to the difference between the slot length and the offset time. The past time slot were tested but have not been implemented in experimental sequences.

Protocol sequence and protocol ID

In order to have the possibility of reproducing experiment sequence a protocol sequence file (XML) is created and transmitted to the PXI controller where the camera control (sect. 3.6) can request it and save it with the corresponding pictures generated by the sequence. As a safety feature the protocol sequence has a time stamp (protocol ID) which is generated when the sequence is transmitted to the PXI controller. The protocol ID is also requested by the camera control and stored with the raw data (app. C)

Visualisation of channels of a sequence

In long sequences it is difficult to follow the values of each channel, even when they are displayed on the front end. In the common display the time is shown in tick and the channels are shown by number instead of name. In order to provide an easy way to follow each channel another module has been created, this can be placed in a branch at the end of the sequence just before the transmission module. Each channel is displayed in oscilloscope type, where can be chosen the channels to be displayed by name. Also the time scale can be set to s, ms, or μs. This program is useful to debug

[21] In the case of VISA channels this does not need to be done since the commands have been send in the fist slot.

the sequences and is shown in figure 2.20.

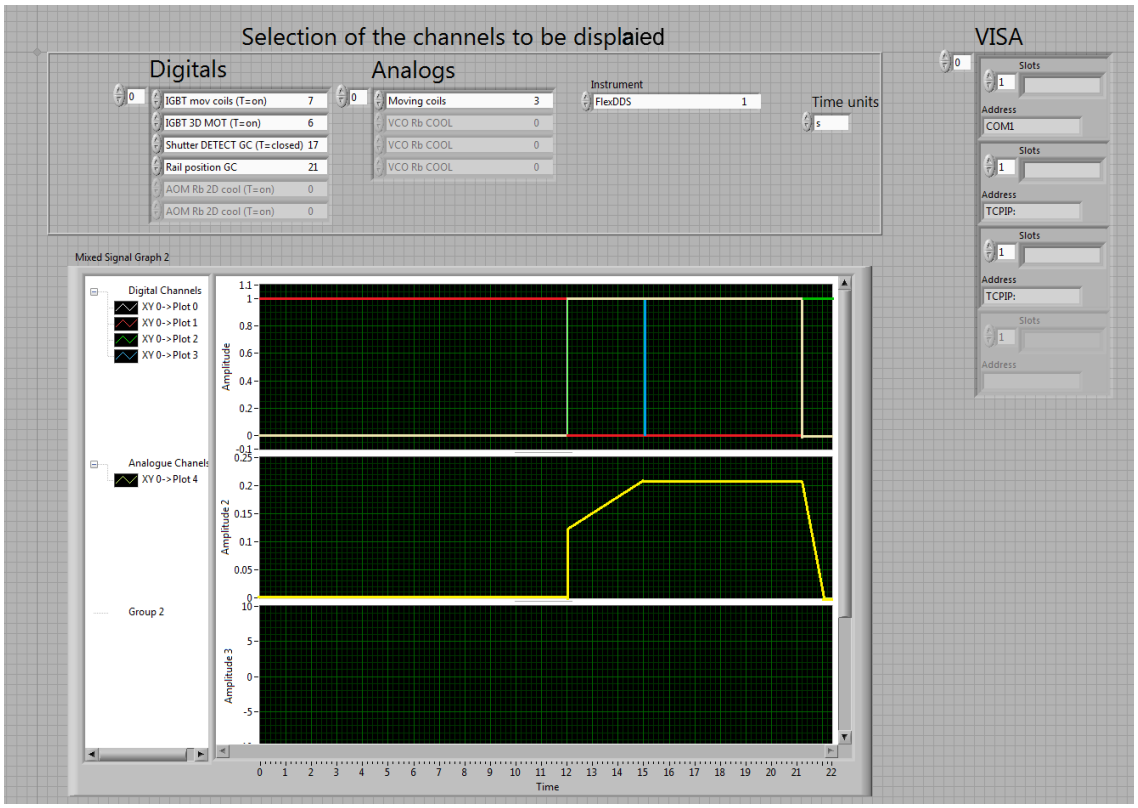

Figure 2.20: *Display module.* In this figure the display module is shown. At the top the selection of the channels is accomplished continuing with the selection of the time units at the right side.

2.7 Summary

This chapter has introduced and described the experimental system formed by: *i*) the vacuum system with three main chambers 2D MOT, 3D MOT and science chamber, *ii*) the laser system capable of producing light for laser cooling and detection, *iii*) the magnetic quadrupole traps used for magnetic trapping (3D MOT and Feshbach coils) and transport (transport coils), *iv*) the optical dipole trap design and the characteristics and *v*) the computer control of the system. Additional information about this experiment design can be found in [33–36]. The detection part of the experiment is presented in the next chapter.

CHAPTER 3

DETECTION

All detection methods are done via optical diagnostic. Direct contact measurements cannot be used since the samples are too small ($\sim 10^5 - 10^9$ atoms) and too cold (mK$-\mu$K) [12]. Luckily, optical diagnostics are very versatile and easy to implement for cold atom systems.

The detection system allows us to visualise and measure the atomic cloud. The aim of all imaging systems and image processing is to supply reliable density distributions of the atom cloud. All properties of the thermal clouds and the condensates are inferred from these density distributions. The inferred information is obtained by comparing the measured distributions with the theoretical density distributions [12].

The observation of the ultra cold atoms can be done in trapped state or in a ballistic expansion. These two methods of observing the ultra cold cloud are called in-situ and time of flight. Furthermore there are three main detection methods used in the cold atoms community: *absorption, fluorescence and dispersive*. Each of these methods relies on different processes of interaction between the atoms and the light and will be described in the following section.

In this chapter I will briefly introduce the interaction of the atom with a probe beam of light and the physical principles of absorptive, fluorescence and dispersive imaging (sect. 3.1), followed by atom number calculations from fluorescence imaging (sect. 3.2), continuing with a brief description of the density distribution for ultra cold atom clouds at different temperature regimes (sect. 3.3) and how to process the absorption images in order to obtain physical quantities like atom number and temperature. Processing of absorption images is discussed in section 3.4, carrying on with the

description of the detection systems (sect. 3.5) and the camera control (sect. 3.6).

3.1 Atom - light interaction for detection

In this section I present the basic parameters needed to describe the detection processes. The detection is performed by illuminating the atom cloud with a probe beam. A beam of light passing through an atom cloud entails three processes: absorption of photons, re-emission of photons, and phase shift of the transmitted light. These processes are respectively the basis of *absorptive, fluorescence,* and *dispersive* detection methods. Absorption and dispersive imaging look at the changes on the detection beam produced by the atom cloud, while fluorescence imaging collect the scattered light.

In order to deduce information from the detected light it is needed to understand the interaction of the probe beam with the atom cloud. In general this interaction can be described by the complex index of refraction $n_{ref}(\vec{r}) = \sqrt{1 + 4\pi n(\vec{r})\alpha}$ [12], where $\alpha = \alpha_0\omega_0^2/(\omega_0^2 - \omega_L^2)$ is the atomic polarisability, and $n(\vec{r})$ is the atom cloud density. Assuming $n_{ref} - 1 \ll 1$, the index of refraction for a two-level system can written (in the rotating wave approximation) [12, 63] :

$$n_{ref}(\vec{r}) \;=\; 1 + \frac{\sigma_0 n(\vec{r})\lambda}{4\pi}\left[\frac{i - 2\Delta/\Gamma}{1 + 4(\Delta/\Gamma)^2 + (I/I_{sat})}\right], \tag{3.1}$$

where $\sigma_0 = \hbar\omega_0\Gamma/2I_{sat} = 3\lambda^2/2\pi$ is the resonant cross section for a two level atom, $\Delta \equiv (\omega_L - \omega_0)$ is the detuning of the laser field ω_L from the atomic transition ω_0, Γ is the linewidth of the transition, I_{sat} is the saturation intensity for the transition, and I is the intensity of the probe beam that propagates along z axis. This index of refraction $n_{ref}(\vec{r})$ (eq. 3.1) can be rewritten in terms of the scattering cross section σ_{sc} [63] as:

$$n_{ref}(\vec{r}) \;=\; 1 + \frac{n(\vec{r})\lambda}{4\pi}\sigma_{sc}\,(i - 2\Delta/\Gamma)\,, \quad \text{with} \tag{3.2}$$

$$\sigma_{sc} \;=\; \frac{\sigma_0}{1 + 4(\Delta/\Gamma)^2 + (I/I_{sat})}. \tag{3.3}$$

The scattering cross section σ_{sc} depends on the detuning Δ from the atomic transition and the

saturation parameter I/I_{sat}. For resonant light ($\Delta = 0$) and low intensity probe beam ($I \ll I_{sat}$) the scattering cross section σ_{sc} reduces to the resonant cross section σ_0 for two level atom.

From general optics [84] we know that the probe beam with an amplitude $E_0(x, y)$ travelling along the z axis and passing through the atom cloud with index of refraction n_{ref} is modified by the atom cloud according to:

$$\vec{E}(x,y) = \vec{E}_0(x,y) \exp\left(\frac{2\pi i}{\lambda}\int_z (n_{ref}-1)dz\right) \tag{3.4a}$$

$$= \vec{E}_0(x,y) \exp\left(\frac{-1-2i\Delta/\Gamma}{2}\sigma_{sc}\int_z n(x,y,z)dz\right) \tag{3.4b}$$

$$= \vec{E}_0(x,y) \exp\left(-\frac{1}{2}\sigma_{sc}\int_z n(x,y,z)dz\right) \exp\left(-i\frac{\Delta}{\Gamma}\sigma_{sc}\int_z n(x,y,z)dz\right) \tag{3.4c}$$

$$= \vec{E}_0(x,y)\, t_a\, \exp(i\phi), \tag{3.4d}$$

where the exponential attenuation (absorption) t_a of the light and the phase shift ϕ are expressed in terms of the product of the column density[1] $\tilde{n}(x,y) = \int_z n(x,y,z)dz$ and the scattering cross section σ_{sc} as [12]

$$t_a = \exp\left(-\frac{1}{2}\sigma_{sc}\tilde{n}(x,y)\right) = \exp\left(-\frac{OD}{2}\right), \quad \text{and} \tag{3.5}$$

$$\phi = -\frac{\Delta}{\Gamma}\sigma_{sc}\tilde{n}(x,y) = -\frac{\Delta}{\Gamma}OD. \tag{3.6}$$

with OD the optical density defined in terms of the column density $\tilde{n}(x,y)$ as:

$$\boxed{OD = \sigma_{sc}\tilde{n}(x,y) = \sigma_{sc}\int_z n(x,y,z)dz.} \tag{3.7}$$

The optical density OD is all the information that is collected from the cloud, from it all the physical properties of the cloud are inferred. In order to obtain a reliable optical density, processing of the images is needed. This image processing is discussed in sect. 3.4.

Absorption and dispersive detection methods rely on measuring the probe beam attenuation t_a and the phase shift ϕ respectively. On the other hand fluorescence detection measures the number

[1]The column density $\tilde{n}(x,y)$ is the density profile $n(x,y,z)$ integrated along the detection axis z.

of photons scattered from the probe beam by the atom cloud as described below.

Each photon that is absorbed by the atom cloud is spontaneously re-emitted[2] in an isotropic way with a rate $\Gamma = 1/\tau$ which is the natural decay rate of the exited state also called natural linewidth of the transition. The total number of photons spontaneously re-emitted per atom is given by the scattering rate R_{sc} which is the product of the decay rate Γ and the population of the excited state ρ_e as [63]:

$$\boxed{R_{sc} = \left(\frac{\Gamma}{2}\right) \frac{(I/Isat)}{1 + 4(\Delta/\Gamma)^2 + (I/I_{sat})}} \tag{3.8}$$

The re-emitted photons are detected and used to obtain information of the atom cloud such as atom number as shown in next section.

3.2 Fluorescence imaging

A relatively easy way to calculate atom number is by detecting the spontaneous re-emission of photons. In this experiment fluorescence detection is used to calculate atom number in the 3D MOT. The detection of the photons is done with two different detectors: a photodiode[3] and a charge-coupled device (CCD) camera[4]. Both detectors have an imaging system that collects the photons and image them onto the respective detectors. The description of the imaging systems is presented in section 3.5. In this section I introduce the formalism used to calculate the atom number from fluorescence detected by both detectors.

In order to relate the number of photons detected by the photodiode or CCD camera with the number of atoms, one needs to know how many photons are scattered[5] per atom and from all these scattered photons how many have been detected. Therefore is required to calculate two things: the total number of scattered photons by the atom cloud and the detection area.

[2]For simplicity in here is not considered the case of stimulated emission.
[3]Contronic OSI100-V-500K/5K-100mm^2 5kHz bandwidth photodiode
[4]PCO Pixelfly qe
[5]The re-emission of photon can be expressed as a scattering process where the probe beam photons have been redirected.

Number of scattered photons

The number of scattered photons per atom is given by the scattering rate R_{sc} (eq. 2.19) which depends of the natural decay rate Γ and the intensity I of the probe beam. Thus the total number of scattered photons $N_{photons}$ is the product of the number of atoms N and the scattering rate R_{sc} as:

$$N_{photons} = N\, R_{sc} \tag{3.9}$$

Since the re-emission of photons by the atoms is isotropic, the detection of a fraction of the total scattered photons $N_{photons}$ is sufficient to determine the total number of atoms N.

Detection area

The detection systems collect a percentage of the total number of scattered photons $N_{photons}$. The number of photons detected is constrained by the aperture of the first lens of each detection system and the separation between this lens and the atom cloud. The percentage of detected photons is given by the ratio of detection solid angle A_d and total solid angle Ω. Where the detection solid angle A_d is determined by the size of the first detection lens as:

$$A_d = \pi(D/2)^2. \tag{3.10}$$

where D is the effective aperture. The solid angle Ω is calculated with the distance d_0 from the 3D MOT center to the first detection lens as:

$$\Omega = 4\pi d_0^2. \tag{3.11}$$

Combining the result from the detection solid angle A_d (eq. 3.10) and the total solid angle Ω (eq. 3.11) the percentage of detected solid angle $d\Omega$ is:

$$d\Omega = \frac{A_d}{\Omega} = \left(\frac{D}{4d_0}\right)^2. \tag{3.12}$$

The total number of photons detected $N_{phot-det}$ is equal to:

$$N_{phot-det} = N_{photons} d\Omega = N R_{sc} d\Omega \tag{3.13}$$

Once the number of photons detected $N_{phot-det}$ has been expressed in terms of the total number of atoms N, we have to look at each specific detector to express the voltage V_d across the PD or number of counts N_{counts} detected by the camera as a function of photons.

Starting with the photodiode PD, the voltage drop V_d is proportional to the number of photons detected $N_{phot-det}$, the photodiode quantum efficiency qe for 780nm and the photodiode transimpedance gain G_{PD} as

$$V_d = N_{phot-det}\ qe\ G_{PD}\ e^- \tag{3.14}$$

with e^- the electron charge.

For the camera the total number of counts N_{count} in the whole CCD camera is proportional to the number of photons detected $N_{phot-det}$, the exposure time t_{exp}, and the CCD efficiency η_{count} (counts/photon) given by [63]:

$$N_{count} = N_{phot-det}\ t_{exp} \eta_{count} \tag{3.15}$$

As a result the number of atoms can be calculated as:

$$\boxed{N = \frac{V_d}{R_{sc}\, d\Omega qe G_{PD} e^-}} \quad \text{for the photodiode, and} \tag{3.16}$$

$$\boxed{N = \frac{N_{counts}}{R_{sc}\, d\Omega\, t_{exp} \eta_{count}}} \quad \text{for the CCD camera.} \tag{3.17}$$

3.3 Density distribution of ultracold atom clouds

This section presents some theoretical density distributions used to describe condensates and cold clouds. Three cases are considered: a thermal cloud, a pure BEC at zero temperature and a partially

condensed cloud. The deduction of these density distributions is mainly base on [12]. All the atom clouds will be held in a harmonic trapping potential and then released. The description of the spatial density will be presented for a trapped state and for the ballistic expansion (TOF). The special case of thermal cloud in a quadrupole trapping potential will be discussed in great detail in sect. 4.2.

These density distributions are needed to describe the atom cloud and to obtain the theoretical optical densities, from where the physical parameters are inferred. Since the final stage of the experiment is in the dipole trap, which can be approximated as a harmonic potential, this thesis presents the density distribution of the BEC and thermal cloud in this type of trapping potential.

3.3.1 Thermal clouds

Let us consider a harmonic trapping potential $U(\vec{r})$:

$$U(\vec{r}) = \frac{1}{2}m(w_x^2x^2 + w_y^2y^2 + w_z^2z^2), \tag{3.18}$$

where w_x, w_y, w_z are the trapping frequencies along the axes x, y, z respectively. A thermal cloud in this trapping potential can be described as a canonical ensemble (constant N) or as a grand-canonical ensemble (constant μ). Since in the experiment the number of particles is not constant it is more appropriated to consider the cloud as a grand-canonical ensemble. Bose-Einstein statistics describes better the atom cloud at low temperatures than the classical statistic (Maxwell-Boltzmann) since it considers the indistinguishable nature of the particles. In Bose-Einstein statistics the density of the phase-space is given by [85]

$$n(\epsilon_i) = \frac{1}{exp\left((\epsilon_i - \mu)/k_BT\right) - 1} \tag{3.19}$$

where ϵ_i is the eigen energy of the state i and is the sum of the potential and kinetic energy of each atom which is equal to $\epsilon = \vec{p}^{\,2}/2m + U(\vec{r})$, and μ is the chemical potential. From this phase space

density $n(\epsilon_i)$ the spatial density distribution $n(\vec{r})$ is defined as

$$n_{th} = \int_p n(\epsilon_i) \frac{d^3p}{h^3}, \tag{3.20}$$

where the subscript th denotes thermal.

Integrating over the momentum we obtain [12]

$$n_{th}(\vec{r}) = \frac{1}{\lambda_{dB}^3} g_{3/2}(z(\vec{r})), \tag{3.21}$$

where $z(\vec{r}) = \exp((\mu - U(\vec{r}))/k_BT)$, $\lambda_{dB} = h/\sqrt{2\pi m k_B T}$ is the deBroglie wavelength, T is the temperature, k_B is the Boltzmann constant, and $g_j(z) = \sum_i z^i/i^j$ is the Bose function where the indistinguishable particles is taken into account.

3.3.2 Bose-Einstein condensates at zero temperature

The Bose-Einstein condensate has been studied extensively theoretically [86–93]. Most of the theoretical descriptions of BEC are in a harmonic trapping potential [90, 92], time dependent harmonic trapping potential [87,88] or generic power-law potentials [86]. A general description of BEC can be found in [93]. A brief description of BEC is given in the introduction of this thesis. In this section we focus in the density distribution of a BEC on a harmonic trapping potential.

The order parameter or the wavefunction of the condensate $\Psi(\vec{r}, t)$ is governed by the Gross-Pitaevskii equation [93]:

$$i\hbar \frac{d\Psi(\vec{r}, t)}{dt} = \left(-\frac{\hbar^2}{2m}\nabla^2 + U(\vec{r}) + g|\Psi|^2 \right) \Psi(\vec{r}, t), \tag{3.22}$$

which includes the interaction parameter $g = 4\pi\hbar^2 a/m$, where a is the s-wave scattering length and $|\Psi|^2 = n_c(\vec{r})$ is the density of the condensate. The time dependence of the order parameter can be factorised and obtain a stationary solution the order parameter Ψ which can be expressed as [93]

$$\Psi(\vec{r}, t) = \Psi(\vec{r}) exp(-i\mu t/\hbar). \tag{3.23}$$

The time dependence of the condensate is fixed by the chemical potential $\mu = \partial E/\partial N$. Replacing the stationary solution eq. (3.23) into the time dependent Gross-Pitaevskii equation (3.22) takes a simple form [93]:

$$\left(-\frac{\hbar^2}{2m}\nabla^2 + U(\vec{r}) - \mu + gn_c(\vec{r})\right)\Psi(\vec{r}) = 0, \tag{3.24}$$

This is the stationary Gross-Pitaevskii equation and is commonly solved in two limits: ideal gas and Thomas-Fermi limit. When the BEC is considered as an ideal gas the interaction between particles is neglected in comparison to the kinetic energy ($n_c g \ll \hbar\omega_{x,y,z}$) where $\omega_{x,y,z}$ are the trapping frequencies of the harmonic potential $U(\vec{r})$ (eq. 3.18). For the Thomas-Fermi limit the interaction term is much stronger and the kinetic energy is neglected ($n_c g \gg \hbar\omega_{x,y,z}$). These two limits originate two different density distributions as follows:

Thomas-Fermi limit

In this limit the kinetic energy is small in comparison with the interaction energy thus it is neglected. Therefore the density is obtained from the stationary Gross-Pitaevskii equation (eq.3.24) and is given by [90]:

$$n_c(\vec{r}) = max\left(\frac{\mu - U(\vec{r})}{g}, 0\right). \tag{3.25}$$

Replacing the harmonic potential $U(\vec{r})$ and expressing the chemical potential μ in terms of the total number of particles one obtains [90]:

$$\boxed{n_c(\vec{r}) = \frac{15}{8\pi}\frac{N}{\prod x_{i,c,0}} max\left(1 - \sum_{i=1}^{3}\frac{x_i^2}{x_{i,c,0}^2}, 0\right)} \tag{3.26}$$

where $x_{i,c,0} = \sqrt{2\mu/m\omega_i^2}$ is the half-lengths of the trapped condensate. In a harmonic potential this distribution is a paraboloid where the width along each axis $x_{i,c,0}$ is inversely proportional to the trapping frequency $(\omega_i)^{-1}$ in the respective axis i. The chemical potential μ is fixed by the normalization condition $N = \int n_c(\vec{r})d^3r$, and is equal to [90]:

$$\mu = \frac{1}{2}\left(\frac{15}{4\pi} g m^{3/2}\omega_x\omega_y\omega_z N\right)^{2/5} \tag{3.27}$$

The expansion of the cloud in time of flight TOF depends on the shape of the trap. For an spherical initial configuration ($\omega_x = \omega_y = \omega_z$) the cloud will expand isotropically. In presence of anisotropic confinement ($\omega_x \neq \omega_y \neq \omega_z$), the expansion of the cloud will be faster in the direction where the repulsive forces are stronger [90]. For our dipole trap configuration it is expected a faster expansion along the vertical direction y, as will be shown in section 5.5.

3.3.3 Partly condensed clouds

Since there are no exact solution for a combination of thermal cloud and BEC at finite temperature, the density distribution of a partly condensed cloud is approximated by the bimodal distribution which is the combination of the condensate and thermal cloud densities and is given by [12]:

$$n_{tot}(\vec{r}) = n_{th}(0)\, g_{3/2}\left(\prod_{i=1}^{3} e^{-x_i^2/x_{i,th}^2}\right) + n_c(0)\, max\left(1 - \sum_{i=1}^{3} \frac{x_i^2}{x_{i,c}^2}, 0\right) \tag{3.28}$$

where $n_{th}(0)$ and $n_c(0)$ are the peak densities of the thermal and condensate clouds respectively.

In order to extract properties of the partly condensed cloud from images, the measured column densities are fitted with the bimodal distribution.

3.3.4 Theoretical column density

Until now the description of the three density cases have been given. Since all imaging techniques measure the column density $\tilde{n}$ (eq. 3.38) of the cloud along the imaging axis z. The theoretical column densities for the thermal cloud $\tilde{n}_{th}$ and the condensate $\tilde{n}_c$ have to be obtained by integrating the respective density distributions $n_{th}(\vec{r})$ and $n_c(\vec{r})$ along the detection axis z, giving as a result [12]:

$$\tilde{n}_{th}(x,y) = \frac{\tilde{n}_{th}(0)}{g_2(1)} g_2\left[e^{(-x^2/2x_{th}^2 - y^2/2y_{th}^2)}\right], \tag{3.29}$$

$$\tilde{n}_c(x,y) = \tilde{n}_c(0) max\left(1 - \frac{x^2}{x_c^2} - \frac{y^2}{y_c^2}, 0\right)^{3/2}, \tag{3.30}$$

where $\tilde{n}_{th}(0)$ and $\tilde{n}_c(0)$ are the density peaks of the thermal cloud and the condensate respectively, and have been calculated as $N_{th} = \int \tilde{n}_{th}(x,y)dxdy$ and $N_c = \int \tilde{n}_c(x,y)dxdy$ giving as a result:

$$\tilde{n}_{th}(0) = \frac{1}{2\pi}\frac{N_{th}}{x_{th}\,y_{th}}, \tag{3.31a}$$

$$\tilde{n}_c(0) = \frac{5}{2\pi}\frac{N_c}{x_c\,y_c}. \tag{3.31b}$$

These column density distributions $\tilde{n}_{th}(x,y)$ and $\tilde{n}_c(x,y)$ are used as fitting function to the experimental images.

3.3.5 Extraction of physical quantities from the column density

Total number of atoms: Since the column density is the sum over one of the axis, the total number of atoms can be calculated by summing along the other two axis. Thus for absorption imaging the number of atoms is obtained as [12]

$$N = \frac{A}{\sigma_{sc}}\sum_{pixels} OD(x,y) \tag{3.32}$$

where, A is the area per pixel of the image, σ_{sc} is the scattering cross-section of the atom cloud (eq. 3.3), and $OD(x,y)$ is the optical density in absorption imaging. This equation gives us the total number of atoms in the thermal cloud and BEC.

Alternatively the number of atoms can be calculated from the peak densities (eq.3.31) of the condensate and the thermal cloud and their respective cloud sizes (x_{th}, y_{th}) and (x_c, y_c) as:

$$N_{th} = \frac{2\pi A}{\sigma_{sc}}\, g_3(1)\, \tilde{n}_{th}(0)\, x_{th}\, y_{th} \tag{3.33}$$

$$N_c = \frac{2\pi A}{5\sigma_{sc}}\, \tilde{n}_c(0)\, x_c\, y_c \tag{3.34}$$

Temperature: The temperature of the BEC and thermal cloud is assumed to be the same.

The expansion of the BEC is anisotropic since the confinement along the different axis is different and the interaction energy is converted into kinetic energy. On the other hand the thermal cloud expands isotropically since it is assumed that the atoms do not interact. Therefore to determine the temperature of the partly condensate cloud we look at the expansion of the thermal cloud rather than the condensate expansion. If the partly condensate cloud has a small fraction of thermal cloud in such way that is not possible to determine that thermal cloud expansion the temperature can still be determine but long TOF time should be used when the expansion is linear for both BEC and thermal cloud. The calculation of the temperature for a thermal cloud is explained in more detail in sect. 4.1.

Phase-space density: Another important quantity to calculate in the process of getting a BEC is the phase-space density define as

$$PSD = n\,\lambda_{dB}^3 \tag{3.35}$$

where n is the density of the atom and λ_{dB} is the deBroglie wavelength. To calculate the density is needed to know the number of atoms ant the volume occupied by the atom cloud. In order to calculate the deBroglie wavelength we need to know the temperature of the cloud. In some cases rather than give the phase-space density, the peak phase-space density is calculated using the peak densities (eq. 3.31) instead of the density $n(\vec{r})$.

3.4 Absorption imaging

Absorption imaging is one of the most common imaging techniques in the cold atoms field, which is chosen for it simplicity in building and subtracting information from the images, as well as for its high contrast (signal/noise). While the description of the imaging system is presented in sect. 3.5. In this section the detection technique and the processing of the image to obtain the column density are presented.

In absorption imaging the atom cloud is illuminated with a resonant probe beam $\vec{E}_0$. The light

gets attenuated according to eq. (3.4d) and the phase shift ϕ becomes zero because the detuning is zero. The intensity detected $I = 2\epsilon_0 c|\vec{E}|^2$ by a photon detector is then

$$I(x,y) = I_0(x,y)\, exp(-OD), \tag{3.36}$$

where $I_0 = 2\epsilon_0 c|\vec{E}_0|^2$ is the initial intensity of the probe beam. In order to recover the optical density OD which relates to the column density $\tilde{n}(x,y)$ according with eq. (3.7) experimentally one takes two images: the absorption image I_A which is equivalent to the intensity I in eq. (3.36); and the bright field images I_B which is obtain when the probe beam is imaged with no absorbing atoms and gives I_0. As a result the optical density OD is given by:

$$\boxed{OD(x,y) = -ln\left(\frac{I_A}{I_B}\right).} \tag{3.37}$$

Some experiments take an additional image called dark field image I_D with no atoms and no probe light. This image I_D contains all background light sources other than the probe beam. However by reducing the background light in the experiment it is possible to obtain the optical density without taking the dark field image I_D.

Combining the experimentally calculated optical density OD in eq. 3.37 with the theoretical one in eq. 3.7 the column density of the atom cloud can be expressed as:

$$\tilde{n}(x,y) = \frac{1}{\sigma_{sc}} OD = -\frac{1}{\sigma_{sc}} ln\left(\frac{I_A}{I_B}\right). \tag{3.38}$$

This column density $\tilde{n}(x,y)$ is the main source of information from the atom cloud. By comparing this column density $\tilde{n}(x,y)$ with the theoretical description of the atom cloud different physical properties are obtained. The deduction of these theoretical column density and the deduction of the physical properties is shown in section 3.3.

3.4.1 Example of optical density calculation

The camera control (sec 3.6) takes two pictures, the absorption image I_A and the bright field image I_B defined in previous section. From these two pictures it calculates the optical density OD. The

resulting images can be seen in fig. 3.1.

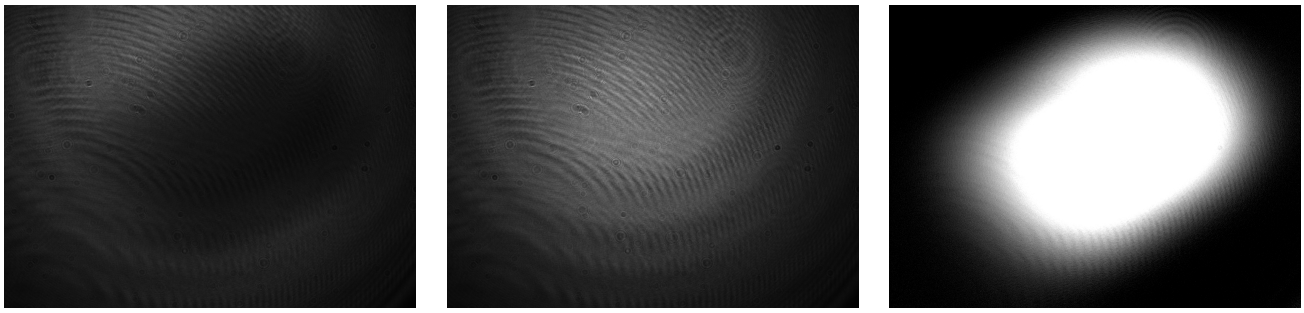

Figure 3.1: *Absorption images processing.* From left to right: absorption image I_A, bright field image I_B and optical density OD.

3.4.2 Defringing algorithm

In the ideal case the absorption image I_A and the bright field image I_B are identical except for the shadow cast produced by the atom cloud. But in all the experiments there is some part of randomness and small fluctuations in the intensity of the beam. Also the polarisation of the light changes slightly over time. Consequently, the light passing through the different windows produces fringes that change over time. Therefore after image processing the obtained optical density has some fringes pattern left. This fringes pattern would make calculations from the OD more noisy and even could throw slightly wrong values. A way to reduce these fringes is by adding a $\lambda/4$ wave plate, this helps us with the big fringes but not with the small ones.

This is the reason behind using an algorithm that could help to best match the fringes pattern at the absorption image I_A. This algorithm has been developed by Erhard [83] and Brinkmann [94] and adapted for our experiment.

The defringing algorithm takes a collection of bright field images $A = \{I_B\}$ and creates an linear combination $I_{def} = \sum_i x_i I_{Bi}$ that best matches the fringe pattern of the absorption image I_A by minimising the difference $Bx - C$ where B is a matrix of scalar products $< A_i|A_j >$, x are the fitting coefficients and C is a vector of scalar products $< A_i|I_A >$. This method works best when the bright field images library A is formed by pictures with the same experimental conditions and have been taken in the same experiment run than the absorption image I_A.

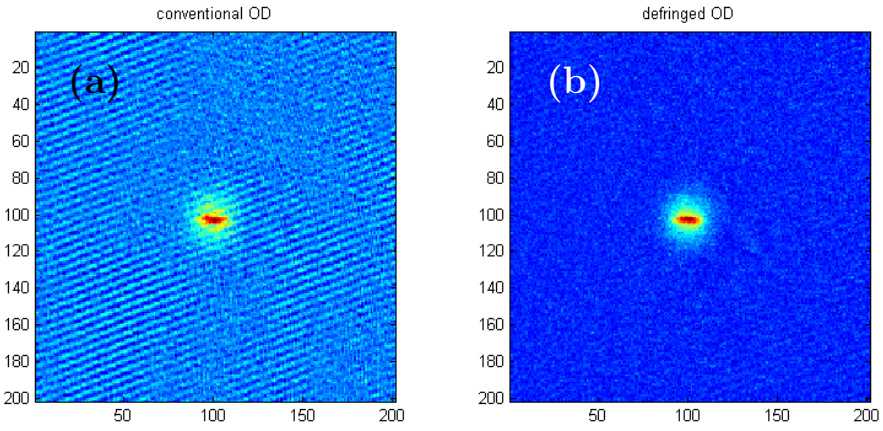

Figure 3.2: *Defringing example*. The BEC has been image using absorption imaging after $30ms$ of time of flight. The optical density OD calculated with the absorption image I_A and bright field image I_B is shown in (a). On the other hand the OD (b) calculated using the absorption image I_A and the solution of the defringing algorithm I_{BD} as bright field image.

An example of this method being applied is shown in fig. 3.2. This is an image of the BEC after 30ms of being released from the dipole trap. In the fig. 3.2 (b) can be seen how the optical density produced with the solution of the defringing algorithm I_{BD} has not fringes in comparison with the standard calculation of the optical density fig. 3.2 (a).

This defringing algorithm is used in all image processing of the experimental data. Besides this defringing algorithm has been integrated in the camera control, where the optical density is calculated in real time. More details about camera control is presented in sect. 3.6.

3.4.3 Background subtraction

After calculating the defringe optical density OD_{def} using the defringing algorithm, the background of the images is set to zero by selecting a area where atoms are no present and averaging over this area giving BG. As a result the final optical density is given by

$$OD = OD_{def} - BG. \tag{3.39}$$

The background subtraction plays an important role when the atom number is calculated with eq.(3.32) since every pixel counts towards the atom number N. This subtraction is also important

for the calculation of the standard deviation σ_t of the atom cloud explain in sect. 4.4. In here each count of the pixels also contributes to the standard deviation

3.5 Imaging systems for detection

In this section the detection systems for fluorescence and absorption imaging are presented. After talking about atom light interaction, detection methods used at the experiment and quantitative analysis of images.

In the current experiment we use two different methods of detection, absorption and fluorescence. Absorption imaging is used to determine number of atoms and temperature of the atom cloud at different stages of the experimental sequence. On the other hand fluorescence imaging is just used to calculate the number of atoms. The detection system for absorption imaging was designed to be easily exchangeable in position and magnification in order to best image the atom cloud.

3.5.1 Detection system for fluorescence

The detection system for fluorescence imaging with the photodiode is shown is fig. 3.3. It is composed of a single lens[6] L and the photodiode PD[7]. The characteristic of the lens L are back focal length of $f_b = 69$mm and a clear aperture of $> 90\%$ of its diameter $D = 75$mm. The characteristic values of the photodiode are a quantum efficiency $qe = 80\%$ for 780nm light and a transimpedance gain $R_{PD} = 500\text{k}\Omega$. The detection system assumes the atom cloud as a point source at a distance d_0 from the detection lens L that is imaged at the PD. The distances between atom, lens and PD are related by thin lens formula

$$\frac{1}{f_b} = \frac{1}{d_0} + \frac{1}{d_I} \tag{3.40}$$

Typically after fully loading the 3D MOT we have 2 x 10^9 atoms at a detuning of $\Delta = 2\pi \cdot 20$MHz from the main transition and total intensity on the six beam of $I = 13.8\text{mW/cm}^2$. This intensity is given for $1/e^2$ diameter. Low and high limit for the number of atoms can be calculated by taking

[6]Thorlabs planoconvex lens LA1740.
[7]Centronic OSI100-V-500k-5k

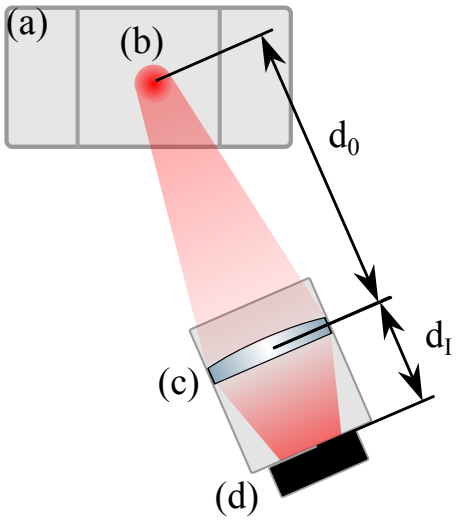

Figure 3.3: *Optical system for the photodiode.* This picture shows the schematic of the photodiode detection system that is formed by a lens (c) with a numerical aperture (N.A.=0.4) and the photodiode (d). As well, in the picture is depicted the atom cloud (b) that is inside of the 3D MOT camber (a). The distance from the 3D MOT to the first lens is $d_0 = 367$mm and for the lens to the PD is $d_I = 85$mm.

different values of the intensity: as the peak intensity or $1/e^2$, for more information refer to [35].

3.5.2 Detection system for absorption imaging

Another omnipresent detection method in the field of cold atoms is *absorption imaging*. The advantage of this method is that the signal is independent of the illumination light, because it is subtracted. One technical condition is that one should be able to take two pictures in short succession, in order to avoid fluctuations of light intensity and polarization. The main disadvantage is that it is a destructive method, meaning that every time a measurement is taken the sample is destroyed.

To carry out absorption imaging, a probe beam is needed, which illuminates the atoms. In sect. 2.3, the wave-length of the light was specified in order to be in resonance with an atomic transition. This way the atoms absorb the light and create a shadow cast in the image detected. As a detector we are using a CCD-camera[8] with maximum resolution of 1392×1024 pixels and pixel

[8]PCO pixelfly qe.

size of $6.45 \times 6.45 \mu m^2$. It is controlled by a PCI-board.

Absorption imaging is used as the primary detection method. For this reason we created an optical system that images the whole cloud. Taking into account that our camera chip is $6.6 \times 9 mm^2$. The largest cloud of atoms is at the 3D MOT, with $\sim$ 6mm diameter before being released from the trap and will expand during time of flight. An optical system is needed to demagnify sufficiently to capture the hole cloud on the camera chip. A detection beam is also required that is larger than the cloud such that the whole cloud distribution can be captured.

On the other hand, the smallest cloud is held in at the dipole trap, with $11.4 \times 386 \mu m^2$ vertical and horizontal waist respectively [33]. To image this, a magnifying system is needed.

For the case of the 3D MOT chamber, the main access is from the side as can be seen in the experimental setup sect. 2.1, and part of it is blocked by the MOT telescopes. On the other hand the glass cell has access for imaging on both vertical and horizontal directions.

Horizontal detection

The design of the opto-mechanical system was developed to allow the flexibility to change in position and magnification, but also to maintain easy alignment and stability. For these reasons commercial $2''$ lens tubes and lenses were used. In this way we can exchange the lenses at any time in order to modify the magnification. Mechanical mounts for the lens tubes and the camera were designed with the aim of making the alignment simple and to remove the unneeded axis of freedom. These mounts are fitted onto a rail in such way that the components can be moved forwards and backwards without rotating them. These mounts also set the same height for all the optical components, so they have the same optical axis, additionally, the camera is mounted on a measuring stage[9] for fine adjustment, see fig. 3.4.

A schematic of the imaging system for horizontal detection can be seen in fig. 3.5. The system works assuming that the atom cloud is a point source, when the first lens l_1 is placed at its focal distance f_1 from the atom cloud, the light will be collimated. The second lens l_2 is placed behind the first lens. Finally the camera is placed at a distance f_2 from the second lens. This configuration gives a magnification of $m = f_2/f_1$. This optical system is similar to a 4F system, the main difference

[9] Owis measuring stage **MT30**

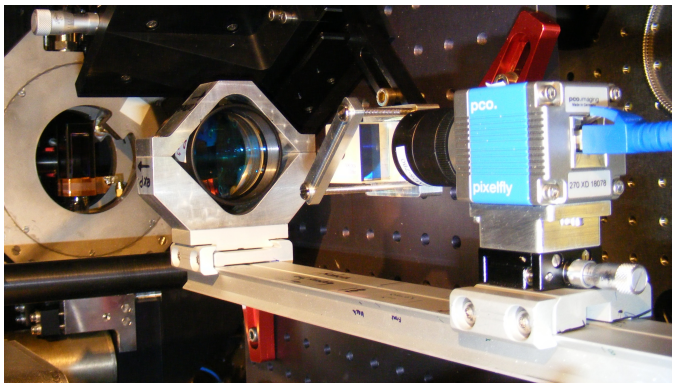

Figure 3.4: Horizontal detection hardware

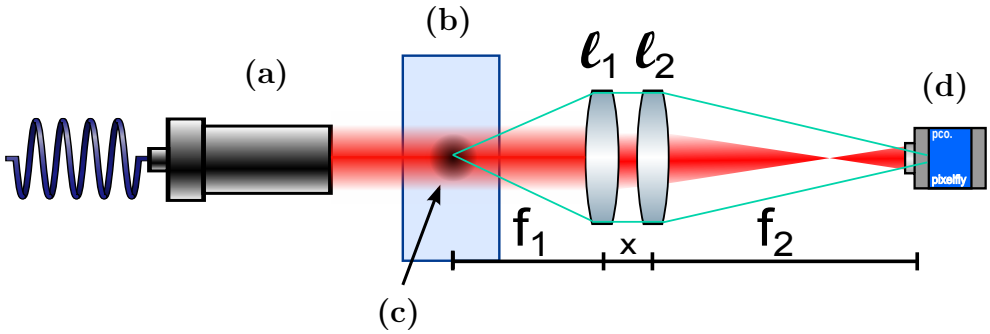

Figure 3.5: *Horizontal detection diagram.* This diagram shows the working principles of the horizontal detection. Resonance light coming from the laser system is collimated by a telescope (a). Collimated light illuminates the atoms cloud (c) which are inside of a vacuum chamber (b). The atoms cloud is assumed to be a point source which is image by the two lenses system (ℓ_1, ℓ_2) into the CCD camera (d). Differently the detection beam is first focused and then diverges.

is that the separation between the two lenses is independent of their focal length. In fact in our configuration the lenses are close together in order to save space.

In order to determine the maximum intensity that can be used for the detection beam, one has to look at the atomic transition saturation intensities I_{sat}. The intensity of the probe beam should not exceed the saturation intensity of the transition used, which is 1.67mW/cm^2 for ^{87}Rb [63]. In the experiment we use telescopes with lens $f = 100$mm that produces a Gaussian beam with a diameter of 19.7mm at $1/e^2$ level from the peak intensity. The power going to the detection beam is 220μW. This give a intensity $I = 72\mu$W/cm^2 which is just 4% of the saturation intensity I_{sat}.

Vertical detection

In order to detect at the glass cell we use the same detection system as for the 3D MOT chamber, but in order to observe small features of the BEC we need a detection system capable of high magnification. It is aimed for a detection system with better resolution, that can be used for future line of research of the experiment. One of these lines is a BEC in an optical lattice with lattice spacing of 1.5μm. Another is the observation of solitons in a BEC, in the special case of 2D systems. In order to observe solitons it is required to have a resolution of the order of a healing length or lower with typical values $0.5 - 1\mu$m [36, 95]

In order to reach the desirable resolution commercial long working distance microscope objectives are implemented. One advantage of using microscope objectives is that the overall configuration does not need to be modified in order to change the magnification if the parfocal length is the same[10]. Mitutoyo provide objectives with glass-thickness compensation for $20\times$ and $50\times$ magnification.

In addition, these objectives need another optical element in order to produce an image into the CCD camera. This element is called secondary lens or colloquially tube lens[11]. With this configuration the detection system is long ($\approx$ 470mm), but with the flexibility of changing the magnification simply by replacing the objective with another one. It may need a small adjustment to compensate for the different parfocal lengths. A schematic of the system can be seen in fig. 3.6 left, where the focal plane at the bottom represents the position of the atoms. For comparison I also include a schematic of the detection system fig. 3.6 right.

The detection system is designed to be used with four different microscope objectives (tab. 3.1) without losing resolution. In order to be able to do this we have to look at the characteristics of each of the microscope objective shown in table 3.1. The detection system has three distances to be determined (fig. 3.6 right) the parfocal length P.L., the separation between the objective shoulder to tube lens ℓ and the distance for the tube lens to the CCD camera f_{TL}. The parfocal length P.L. and the tube lens to camera distance are specified by the manufacturing; the P.L. is given in table 3.1 and the f_{TL} is specified to be 240mm. The only distance left to be determined is the position

[10]The parfocal length is define as the distance from the microscope objective shoulder to the image plain.
[11]Mitutoyo tube lens MT-1

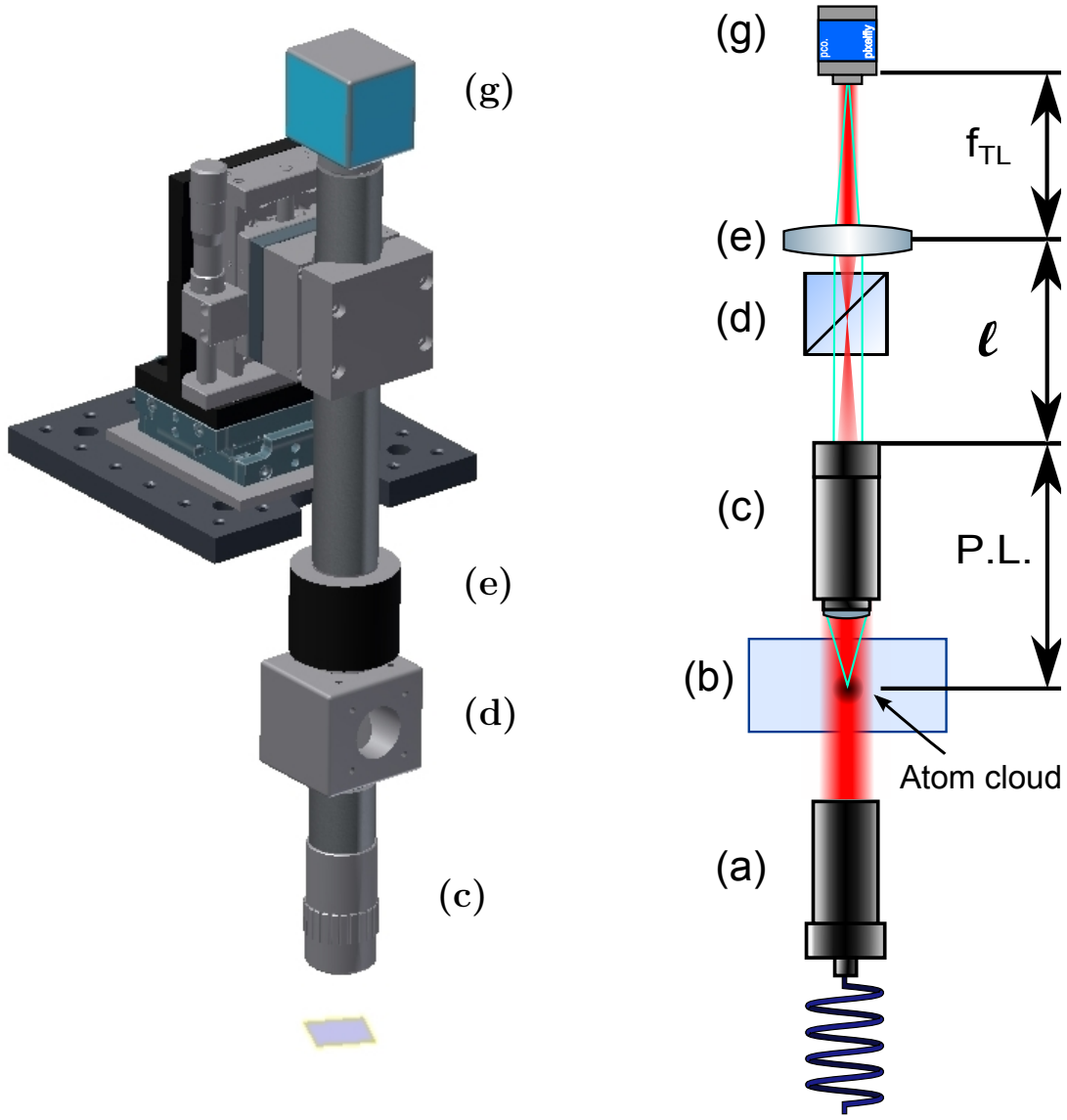

Figure 3.6: *Vertical detection*: drawing (left) and sketch (right). From the bottom to the top an illumination system (a) produces collimated light that illuminates the atom cloud inside the vacuum chamber (b). A microscope objective (c) is looking a the atoms. The tube lens (e) images the intermediate image produced by the microscope objective into the CCD camera (g). In the way between the microscope objective (c) and the tube lens (e) is added a kinematic filter cage cube (d). This cage cube can allocated a dichroic mirror beam splitter, and two polarisers or wave plates. The parfocal length (P.L.) and the distance for the shoulder height to the tube lens (ℓ) are given in table 3.1. The back focal distance of the tube lens is specified as $f_{TL} = 240$mm.

Mag.	**W.D.** [mm]	**P.L.** [mm]	**N.A.**	**f** [mm]	**R** [μm]	**DOF** [μm]	**FOV** [mm]	Φ_1 [mm]	ℓ [mm]
5×	34.0	95	0.14	40	2.8	19.9	4.8	11.2	284.4
10×	33.5	95	0.28	20	1.4	5.0	2.4	11.2	284.4
20×	30.6*	96.19	0.28	10	1.4	5.0	1.2	5.6	408.9
50×	15.08*	96.19	0.5	4	0.8	1.6	0.48	4.0	444.4

Table 3.1: *Microscope objective specifications.* Mag: magnification, W.D.: working distance, P.L.: parfocal length, N.A.: numerical aperture, f: focal distance R: resolution, DOF: depth of field, FOV: field of view for 24mm diameter eyepiece, Φ_1: objective exit pupil diameter, ℓ: separation between tube lens and microscope objective shoulder. The resolution and the focal depth of the objectives are values determined for $\lambda = 780$nm. *Glass corrected working distance with glass thickness of 3.5mm.

of the tube lens with respect to the microscope objective shoulder ℓ, given by [96]:

$$\ell = \frac{(\Phi_2 - \Phi_1) \cdot f_2}{\Phi} \tag{3.41}$$

where $\Phi_1 = 2f_1 N.A.$ is the objective exit pupil diameter given by the focal length f_1 and numerical aperture $N.A.$ of the respective microscope objective, $\Phi_2 = 24$mm and $f_2 = 200$mm are the tube lens clear aperture and focal length respectively, finally $\Phi = 9$mm is the image field of the CCD. The values of ℓ and Φ_1 have been included and are shown in table 3.1. A distance ℓ longer than the specified may produce shading. A distance smaller than ℓ does not affect the optical performance according to the manufacturer [96]. In the vertical detection set up we are using a distance $\ell =$ 112.6mm.

Also the imaging system is designed to have fine adjustment in three different axis (x,y,z) by mounting it on a 3D translation stage.The (X,Y) translation stage[12] is used to align the detection system with the atom cloud, and the Z translation stage[13] is used to focus vertically onto the quasi-2D dipole trap plane. This vertical (Z) translation stage has a bigger range of movement than (X,Y) in order to follow the cloud in time of flight.

[12]Owis KT65-STA, 6mm travelling range in each direction with graduation scale of 5μm.
[13]Owis MT60S-25-X-MSD, 25mm travelling range with fine and coarse graduation of 0.5 and 5μm, respectively.

Tests were performed to determine the maximum achievable resolution of the this imaging system. With the 50× objective and a resolution target (USAF 1951), we are able to yield a resolution of 1.74μm [14] with 780nm illumination light. The resolution is two times worse than specified by the company. This is believed to be caused by the use of coherent light for illumination, which induces fringes reducing the resolution power.

The illumination for absorption imaging and phase imprinting [97] is done from below the science chamber with a similar imaging system like the the vertical detection. Information about this system can be found in [36].

3.6 Camera control

After describing the optical system for detection, this section concentrates on the program that controls the camera and its settings. This program is capable of perform image processing of absorption images in situ as described in sect. 3.4, by calculating the optical density OD and obtaining useful informations, such as number of atoms and temperature (sect. 3.3.5). The obtained information is used as a reference to optimise the experiment.

The goal was to create a program with a graphical user interface (GUI) capable of performing image processing of absorption images in real time, which has the following characteristics (requirements):

- user friendly,
- easy to change camera settings,
- externally triggered by computer control,
- image processing in real time,
- save images and raw data,
- protocol ID and communication.

The supplied camera[15] software *"Camware"* does not have the flexibility required for our experiment only have the basic features for taking and saving pictures, control of the exposure time, and so on.

[14] We are able to resolve elements in the group 8 element 2.
[15] PCO Pixelfly qe

But the camera can also be controlled with MATLAB and LabVIEW.

The first software used to program the camera was LabVIEW. LabVIEW is a programming language suitable for data acquisition and instrument control, and has the advantage that the front panel is already a GUI. This offers the flexibility of an easy manipulation of the GUI. It is user friendly, and covers all the required characteristics mention above reasonably, except for the "image processing in real time"[16]. Moreover programming mathematical operations is simpler in other programming languages. A basic programme was created in LabVIEW, where communication with the camera was established. This program is able to take single and continuous pictures, as a proof of principle that we can control the camera and its parameters.

The final programme was made in MATLAB, implementing the ability to save pictures and raw data, select a region of interest, calculate temperature and number of atoms, defringing algorithm, protocol ID and communication with PXI controller. MATLAB was chosen over LabVIEW for being specialist in dealing with matrices (images), so all the required image processing is easier and faster to do in MATLAB. Besides, all image processing at the camera control and post processing is performed in the same programming language MATLAB. The characteristic of the final program (see fig. 3.7) are described in the following section.

3.6.1 Camera control settings

Upon beginning the GUI program communication with the camera is established, once started we can change the camera parameters such as exposure time, gain, internal or external trigger and magnification. Magnification is not a camera parameter but is needed in order to calculate temperature and number of atoms. Once the camera has been set-up, the control over the program is done over buttons which are explain in the following:

Wait for trigger: Sets the camera in a waiting mode for an external trigger (in our case the computer control trigger). Once the camera has been triggered twice, first for the atoms image and second for the no atoms image, the optical density (OD) is calculated. From the OD all the other quantities like vertical and horizontal projections, the Gaussian fits for

[16]The image processing is described with more detail in sect. 3.4

temperature determination, number of atoms, etc. are calculated. Once the calculations have finished, the images and information display are refreshed and the camera will wait for another two trigger such that the whole process is repeated in a infinite loop until further instructions.

Stop trigger: Breaks the loop on wait for trigger. This means the waiting status and any other processes that are executed in wait for trigger loop are stopped.

Close program: Shuts down the program, taking care of stop the camera and any connection establish with it.

Save pictures: Saves continuously all the images taken, raw data and protocol sequence and store them in a chronological order.

Stop saving: Neutralises save picture button.

Save 1 cycle: This saves a single set of pictures and data.

The saving of the data has been done in a special format called HDF5, more information about the organisation and reading efficiencies of different data structures inside of the HDF5 files is given in appendix C.

3.7 Summary

In this chapter the techniques used to image, measure and characterise the atom cloud were given. A brief introduction of the bases for detection was presented in sect. 3.1, followed by the calculation of the number of atoms with fluorescence imaging (sect. 3.2). Furthermore, in section 3.3 the density distributions for the condensate and thermal cloud were introduced with their corresponding column densities which are used to fit to the partly condensed clouds. Continuing with the image processing (sect. 3.4) of absorption images to obtain a reliable optical densities. Additionally, the detection systems were described (sect. 3.5) and at the end the camera control was introduced (sect. 3.6).

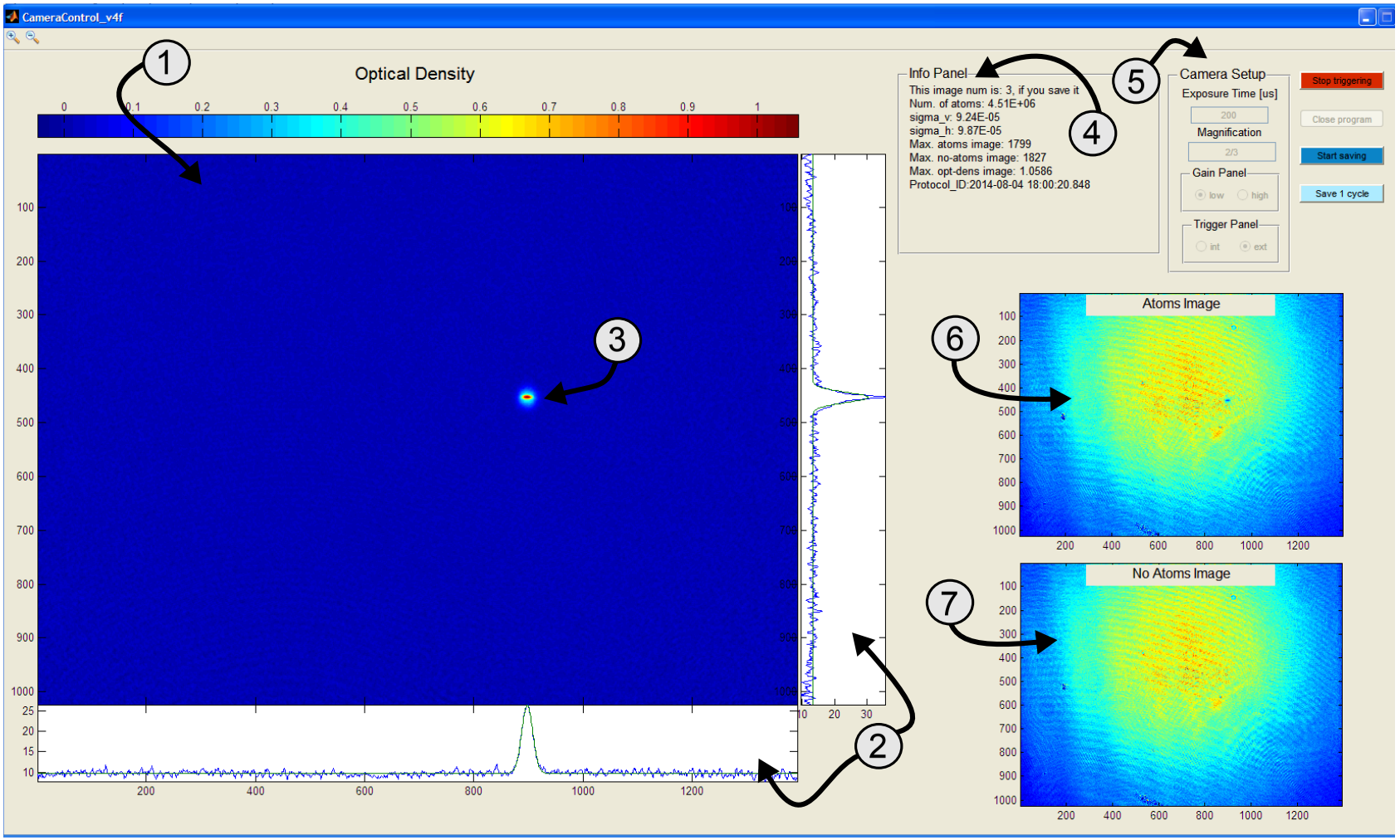

Figure 3.7: *Camera control graphic user interface.* List of components: 1) Optical density image with colour-bar, 2) vertical and horizontal projections of OD with Gaussian fit for temperature calculation, 3) atom cloud, 4) info panel, 5) camera setup, 6) atoms image and 7) no atoms image.

CHAPTER 4

TEMPERATURE DETERMINATION FOR ATOMS IN A MAGNETIC QUADRUPOLE TRAP

This chapter presents a new method of calculating the temperature of an atom cloud held in a magnetic quadrupole trap. The knowledge of the temperature is crucial for characterising the properties of the atom cloud [98]. Furthermore, magnetic quadrupole traps are widely used in the cold atom field, making this new method useful for a vast public.

The research for reliable measurements of the temperature exploded when optical molasses gave a temperature lower than the Doppler limit [99]. Four different methods were used to confirm this result [99], among them are the time of flight (TOF), the fountain, the shower, and the release and recapture (R&R) methods. The first three methods rely on measuring the velocity distribution of a free falling atom cloud and are destructive methods. On the other hand, the R&R method [100] calculates the number of atoms recaptured after turning off the cooling light for a period of time t_{off}. This is not a destructive method since part of the cloud can be recovered. Other types of non-destructive methods are: forced oscillations [101, 102], fluorescence spectroscopy [103] and recoil-induced resonances [104]. However the TOF method is the ultimate winner due to it simplicity and reliability, becoming the most commonly used technique for temperature determination in the cold atoms field.

Before the implementation of CCD cameras, most of the detection methods were done by fluorescence or absorption imaging with photodiode. The TOF technique was not an exception. To realise the TOF method with fluorescence (absorption), a probe beam of resonant light is placed

below the atom cloud at a distance l from the cloud centre. After switching off the trap and letting the atom cloud expand ballistically, the fluorescence (reduction on intensity of the probe beam) produced by the atoms passing through the probe beam is detected as a function of TOF time. Different probe beam geometries [105, 106], clouds with finite size and anisotropic velocity distributions [98], short distance l to the atom cloud [105], and long dropping times [18] have been studied. The temperature is obtained by fitting the detected fluorescence as a function of TOF time with a theoretical description of the falling cloud. The aforementioned methods consider a Gaussian distribution as the initial spatial distribution.

The interest of this chapter is to calculate the temperature of an atom cloud held in a quadrupole trap. The first approach would be to use the common TOF time technique and investigate how adequate and accurate result this technique can give (sect. 4.1). After the atom cloud in the quadrupole trap is described (sect. 4.2), followed by the deduction of the formalism for temperature determination from a single shot (sect. 4.3), continuing with the experimental determination of the cloud size (sect. 4.4) needed for the temperature determination and finally applying the deduced formalism to calculate the cloud temperature of experimentally obtained density distributions (sect. 4.5).

4.1 Temperature determination with the time of flight technique

Detection systems capture the density distribution of the atom cloud but not the momentum distribution (temperature). To recover the momentum distribution the cloud is left to freely expand before detection, such that the momentum distribution is rendered into the position distribution. This approach is the basis of the time of fight (TOF) technique.

In order to know the spatial distribution $n(\vec{r}, t)$ at any TOF time t, we must know the initial position distribution $n(\vec{r}, 0)$ and the momentum distribution $f(\vec{p})$ of the atoms. The initial position distribution $n(\vec{r}, 0)$ of the atoms depends on the cloud temperature T and on the potential U holding the atoms before their release. The momentum distribution $f(\vec{p})$ of a thermal cloud follows a Maxwell-Boltzmann distribution in momentum that goes as $\propto \exp(-\vec{p}^{\,2}/2\sigma_p^2)$. At long TOF times, the spatial distribution of an expanding cloud is dominated by the momentum distribution

and follows a similar distribution but in position as $\propto \exp(-\vec{r}^{\,2}/2\sigma_r^2)$ (fig. 4.1 (a)), which results in a 3D Gaussian distribution in space.

The cloud temperature is deduced from the cloud size, where the size of the cloud is defined as the standard deviation $\sigma(t)$ of the spatial distribution $n(\vec{r},t)$. The cloud size relates to the temperature T of the atom cloud as:

$$\sigma_t^2 = \sigma_0^2 + \frac{1}{m}t^2 k_B T, \tag{4.1}$$

where m is the atom mass, k_B is the Boltzmann constant and σ_0 is the standard deviation of the (initial) spatial distribution of the atom cloud in the trap. If the standard deviation σ_0 of the initial distribution $n(\vec{r},0)$ is unknown, the temperature still can be calculated from the standard deviation σ_t at different TOF times t. The temperature T is calculated by fitting a line to σ_t^2 versus t^2 as $\sigma_t^2 = b + at^2$, where the slope a is proportional to the temperature

$$T = am/k_B. \tag{4.2}$$

I will refer to this method of temperature calculation as the common TOF technique.

Commonly the cloud size $\sigma(t)$ is calculated by fitting a 2D Gaussian distribution [107] to the measured column density $\tilde{n}(x,y)$ (eq. 3.38). If the initial position distribution $n(\vec{r},0)$ does not follow a Gaussian distribution, which is the case of a cloud released from a quadrupole trap (fig. 4.1), then the calculation of the standard deviation σ_t with a Gaussian fit will lead to the wrong temperature at short TOF times. This way of calculating the cloud size is more reliable for long TOF times since the distribution of the cloud is dominated by the ballistic expansion that follows a Gaussian distribution. Therefore, for the common TOF technique long TOF times are required, which in some cases, such as for hot clouds in a relatively small chamber, is not possible to realise, making it difficult or impossible to extract a reliable spatial distribution from the images. Moreover due to gravity the maximum TOF time of all systems is limited by the maximum allowed free fall distance d as $TOF_{max} < \sqrt{2d/g}$.

In order to improve temperature calculation in the short TOF regime, one has to consider the

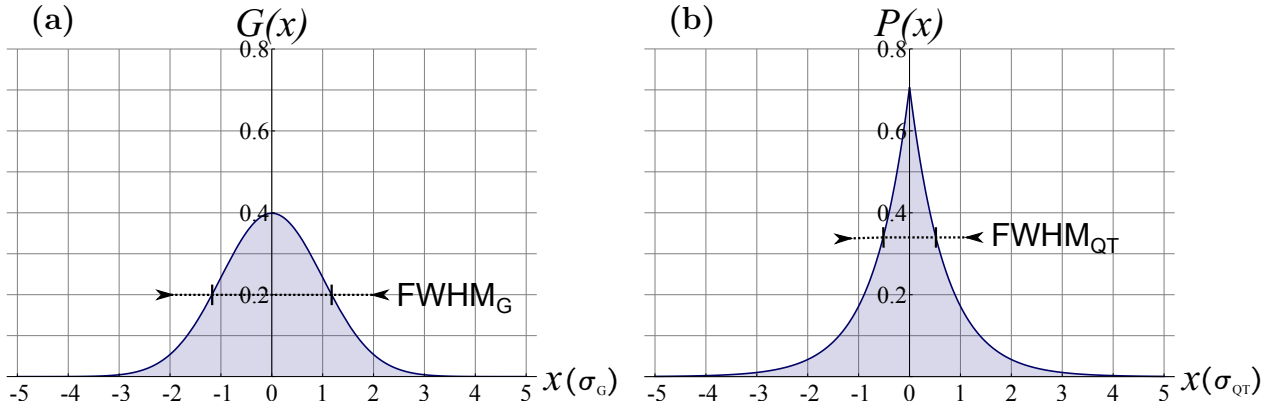

Figure 4.1: *1D Gaussian distribution and 1D density distribution in a magnetic quadrupole trap.* A normalised 1D Gaussian distribution (a) goes like $G(x) = \exp(-x^2/2\sigma_G^2)/\sigma_G\sqrt{2\pi}$. On the other hand the normalized 1D density distribution for a quadrupole trap (b) goes as $P(x) = \exp(-\sqrt{2}|x|/\sigma_{QT})/\sigma_{QT}\sqrt{2}$ (see appendix D). Where σ is the standard deviation of the respective distribution, and it is assumed to be one. Both distribution are normalised. In addition the full with half maximum (FWHM) of each distribution has been depicted. Which are equivalent to $\mathrm{FWHM}_G/2 = \sqrt{2\ln(2)} * \sigma_G \sim 1.18\,\sigma_G$ and $\mathrm{FWHM}_{QT}/2 = (\ln(2)/\sqrt{2}) * \sigma_{QT} \sim 0.49\,\sigma_{QT}$

cloud trapping potential and the gravitational potential that determine the initial spatial distribution $n(\vec{r}, 0)$, where the gravitational field deforms the trapping potential. This deformation is more prominent in shallow traps than in tight traps since the confinement is weaker.

In our experiment the atoms are held in a magnetic quadrupole trap. In this commonly used trap, the spatial distribution is different from a Gaussian distribution as can be seen in fig. 4.1. In time of flight the spatial distribution is the convolution of the quadrupole trap distribution and the momentum distribution (Gaussian). Studies of the spatial distribution at short TOF has been done before [32], but consideration of the influence of the gravitational field have not been done before for temperature determination. The common TOF technique is regularly used to determine the cloud temperature on this type of trap but using long TOF times. An alternative method to calculate the temperature of a cloud in a quadrupole trap was developed by Ram et al. [108] by knowing the cloud temperature in the previous experimental stage (molasses). Also studies of the density distribution of the atom cloud inside of the quadrupole trap have been done before [32,109], although gravity was not included. In the following the density and momentum distributions of an atom cloud inside of a quadrupole trap is deduced.

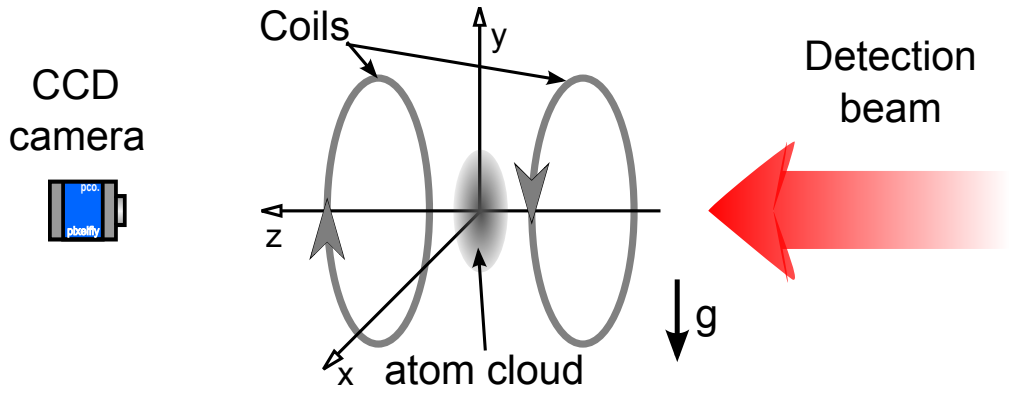

Figure 4.2: *Quadrupole trap schematics.* The diagram shows the configuration of the coils producing a magnetic quadrupole trap. The coils symmetry axis z is the strong axis and the radial direction $\rho = \sqrt{x^2 + y^2}$ is the weak axis. The gravitational field acts along the y axis and the detection system looks along the z axis.

4.2 Thermal atom cloud in a magnetic quadrupole trap

The thermal atom cloud can be considered as a dilute gas of non-interacting particles. A quantum mechanical approach to this system is not needed since the temperatures are still high enough ($T > 100\mu K$) to neglect quantum effects[1]. This system is well describe with classical statistic.

From statistical mechanics [85] one knows that a system of N non-interacting particles at a temperature T can be described as a canonical ensemble where the energy $E(\vec{r}, \vec{p})$ of the system depends on the positions and momenta of the atoms. The total energy of each particle is the sum of the potential energy U and kinetic energy E_K. In this description the probability to find a particle in the position $\vec{r}$ with momentum $\vec{p}$ is given by the Boltzmann distribution[2]:

$$P(\vec{r}, \vec{p}) = Z^{-1} \exp(-\beta E(\vec{r}, \vec{p})), \tag{4.3}$$

with $\beta = 1/k_B T$, where k_B is the Boltzmann constant and Z is the canonical partition function which normalises the probability. This normalised phase-space distribution $P(\vec{r}, \vec{p})$ can be used to describe any closed system of non-interacting particles with a defined temperature T.

[1] The thermal de Broglie wavelength λ_{dB} is still small ($\lambda_{dB} \approx 10nm$) in comparison with the atom spacing ($\approx 1\mu m$), for ^{87}Rb atoms at $T = 100\mu K$

[2] The Boltzmann distribution is also called Gibbs distribution.

In order to obtain the phase-space distribution $P(\vec{r},\vec{p})$ for our system we need to calculate the total energy $E(\vec{r},\vec{p})$ of the atoms, which are under the influence of two potentials: the magnetic quadrupole potential U_B produced by the coils and the gravitational potential U_g (fig. 4.2). The magnetic quadrupole potential U_B introduced in section 2.4 (eq. 2.10) can be rewritten as:

$$U_B(x,y,x) = C\sqrt{\rho^2+4z^2} \qquad \text{with} \quad C = g_F m_F \mu_B B', \tag{4.4}$$

where $g_F m_F \mu_B$ is the magnetic moment of the atom and $B' = \frac{\partial B}{\partial \rho}\Big|_{r=0}$ is the magnetic gradient along of the weak axis $\rho = \sqrt{x^2+y^2}$.

The gravitational potential U_g is equal to $U_g = mgh$, where m is the atom mass, g is the acceleration of gravity and h is the absolute height of the atom. The gravitational potential is rewritten in the same reference system as the magnetic potential as $U_g = mgy + A$, where $A = mgy_0$ is a constant and y_0 is the centre position of the magnetic quadrupole trap. Combining these two expressions for the potentials U_B and U_g[3], the total potential energy U is expressed as

$$U = U_B + U_g, \tag{4.5a}$$

$$= C\sqrt{\rho^2+4z^2} + mgy \tag{4.5b}$$

The total potential energy U of the atom depends only on the atom position (x,y,z). A plot of the total potential energy U along each axis is presented in figure 4.3. The potential energy U has the same linear dependence along x and z directions as the magnetic quadrupole potential U_B, but deviates from a symmetric shape along the y axis because of the contribution of the gravitational potential U_g (fig. 4.3 (b)).

On the other hand the kinetic energy E_K of an atom with mass m and momentum $\vec{p}$ is defined as

$$E_K = \frac{1}{2m}|\vec{p}\,|^2, \tag{4.6}$$

and depends only on the momentum $\vec{p}$ and mass m of the atom. Furthermore the total energy E

[3]The constant A can be drop off since it cancels out at the moment of normalisation of the phase-space distribution $P(\vec{r},\vec{p})$.

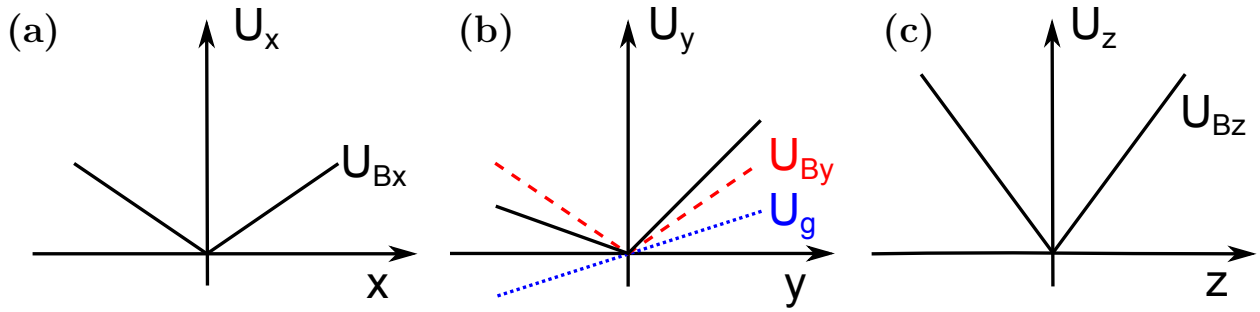

Figure 4.3: *Potential energy cross-sections on different axes.* The potential energy components U_x, U_y, U_z for the three axes x, y and z is depicted in this drawing respectively in (a), (b) and (c). The potential energy has two contributions, the first one U_B is the magnetic potential which has a linear dependence with the absolute distance from the center of the trap (zero point). The second potential energy U_g is the gravitational potential that acts along the y axis and is linear with position. The total potential U is equal to U_B in x and z axis (a) and (c), and it is just modified by gravity along the y axis, as can seen in (b), where the total potential U_y is the combination of the magnetic potential U_{By} (dashed red line) and the gravitational potential U_g (dotted blue line). The potential U_y along the y axis (solid black line) is not symmetric any more due to the contribution of the gravitational potential.

of the atom can be written as

$$E(\vec{r},\vec{p}) = U + E_K \tag{4.7a}$$

$$= C\sqrt{\rho^2 + 4z^2} + mgy + \frac{|\vec{p}\,|^2}{2m}. \tag{4.7b}$$

Once that the total energy $E(\vec{r},\vec{p})$ of the atom has been deduced, the phase-space distribution $P(\vec{r},\vec{p})$ (eq. 4.3) can be expressed in terms of the position $\vec{r}$ and momentum $\vec{p}$ of the atoms by replacing the total energy $E(\vec{r},\vec{p})$ with eq. (4.7b) resulting in:

$$P(\vec{r},\vec{p}) = \underbrace{Z_r^{-1} exp\left(-\beta(C\sqrt{x^2+y^2+4z^2} + mgy)\right)}_{\text{position distribution}} \cdot \underbrace{Z_p^{-1} exp\left(-\beta\frac{|\vec{p}\,|^2}{2m}\right)}_{\text{momentum distribution}}, \tag{4.8}$$

where we have separated the parts that depend on position and momenta. The first term is the position distribution depending only on the potential energy U of the atom. The second term is the momentum distribution depending only on the kinetic energy E_K of the atom. This separation is possible since the phase-space distribution $P(\vec{r},\vec{p})$ does not have cross terms of position and

momentum. Also both distributions are normalised, where the normalisation factors Z_r and Z_p have been calculated analytically and are equal to

$$Z_r = \int exp\left(-\beta(C\sqrt{x^2+y^2+4z^2}+mgy)\right) \mathrm{d}^3r = \frac{4\pi}{C^3\beta^3(1-\alpha^2)^2}, \tag{4.9}$$

$$Z_p = \int exp\left(-\beta\frac{|\vec{p}|^2}{2m}\right) \mathrm{d}^3p = \left(\frac{2\pi m}{\beta}\right)^{3/2}, \tag{4.10}$$

with $\alpha = mg/C$. This parameter α comes naturally when the mathematical expression for Z_r is simplified. Its physical meaning is the ratio between the potential strengths U_B and U_g. In order to hold the atoms against gravity, the confining magnetic force $\vec{F}_B = -\nabla U_B$ needs to be bigger than the gravitational force $\vec{F}_g = -\nabla U_g$. In order to satisfy this requirement C needs to be bigger than mg, as a result α is always smaller than one for magnetically trapped atoms.

In order to calculate Z_r in eq.(4.9) various changes of variables are done because integrals of exponentials of square roots are not straightforward. The first variable change $2z \to z'$ makes the quadrupole potential isotropic along all axes. The second variable change is a rotation of the axis as $(x, y, z) \to (y, z, x)$. The final change of variables is a transformation of coordinates from Cartesian coordinates (x, y, z) to spherical coordinates (r, θ, ϕ) in order to simplify $\sqrt{x^2+y^2+z^2} \to r$. After these three transformations the integral (eq.(4.9)) is straightforward to solve.

The integral in momentum eq.(4.10) to calculate Z_p is a standard integral of a 3D Gaussian and can be calculated easily.

4.2.1 Position distribution

If we now study the phase-space distribution eq.(4.8) in detail one can see that the position distribution $n(\vec{r})$ in the trap is just dependent of the potential energy and by substituting the normalization factor Z_r (eq.4.9) it can be expressed as

$$\boxed{n(\vec{r}) = \frac{C^3\beta^3(1-\alpha^2)^2}{4\pi}\, exp\left(-\beta C(\sqrt{x^2+y^2+4z^2}+\alpha y)\right).} \tag{4.11}$$

This position distribution $n(\vec{r})$ is in fact the normalised spatial density distribution of the trapped atoms, and has symmetry along x and z axis but not along the y axis due to the effect of the

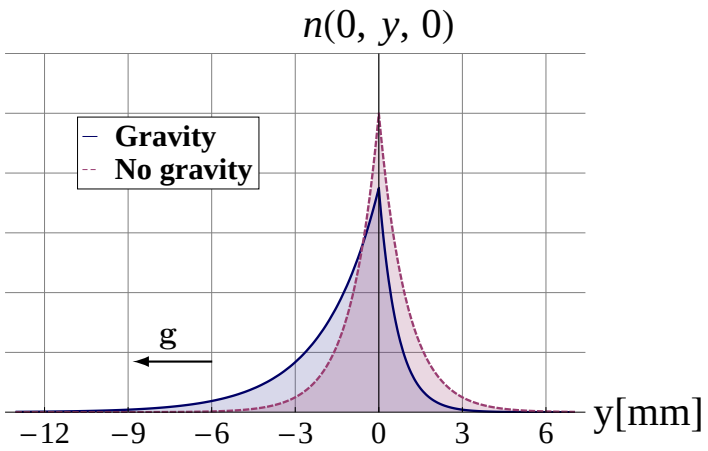

Figure 4.4: *Effect of gravity on the spatial distribution along the y axis.* In this graph $n(x, y, z)$ (eq. 4.11) is plotted with $x = 0$ and $z = 0$. Two spatial distributions $n(y)$ are plotted: $\propto e^{-|y|}$ (dashed pink line) and $e^{-|y|-\alpha y}$ (solid blue line). The atoms follow the pink distribution in case of not gravitational field ($\alpha = 0$), otherwise the blue distribution ($\alpha = 0.5$). The comparison of the two distribution shows the deformation in the spatial density as a result of the gravitational field, where the atoms are pulled away from the magnetic trap centre towards the negative part of the y axis.

gravitational field. A comparison of the normalised spatial densities $n(\vec{r})$ with and without gravity is shown in figure 4.4, where the spatial density $n(\vec{r})$ along the y axis with ($x = 0$, $z = 0$) is plotted for no gravitational field ($\alpha = 0$), and magnetic potential twice as strong as the gravitational potential ($\alpha = 0.5$). In fig. 4.4 can clearly be seen how the gravitational field deforms the symmetric spatial distribution produced by the magnetic quadrupole potential, by making the density distribution along the y axis deviate from the magnetic trap centre it produces an elongated cloud along the y axis, where it is more likely to find atoms below the magnetic trap centre.

The mean of the cloud distribution along the y axis can be calculated as the expectation value of y according to

$$\langle y \rangle = \int y\, n(\vec{r}) d^3 r \tag{4.12a}$$

$$= \frac{-4\alpha}{(1-\alpha^2)C\beta} \tag{4.12b}$$

From this equation 4.12b is clear that for high magnetic gradient (C large and α small) the shifting of the cloud center along the y axis decreases.

4.2.2 Momentum distribution

From the phase-space distribution $P(\vec{r},\vec{p})$ (eq.4.8) one can see that the momentum distribution depends only on the kinetic energy, and obeys the Maxwell-Boltzmann distribution in momentum which is equal to

$$\boxed{f(\vec{p}) = \left(\frac{\beta}{2\pi m}\right)^{3/2} exp\left(-\beta\frac{|\vec{p}|^{\,2}}{2m}\right),} \tag{4.13}$$

this equation can be rewritten explicitly for the momentum coordinates $\vec{p} = p_x\widehat{x} + p_y\widehat{y} + p_z\widehat{z}$ as

$$f(\vec{p}) = \left(\frac{1}{2\pi m k_B T}\right)^{3/2} exp\left(-\frac{p_x^2}{2mk_BT}\right) exp\left(-\frac{p_y^2}{2mk_BT}\right) exp\left(-\frac{p_z^2}{2mk_BT}\right). \tag{4.14}$$

This momentum distribution is isotropic in all momentum directions (p_x, p_y, p_z), and has been written as the product of three independent normalized 1D Maxwell-Boltzmann distribution of p_x, p_y and p_z each with the same standard deviation $\sigma_p = \sqrt{mk_BT}$.

4.3 Deducing the cloud temperature in a quadrupole trap from a single shot

In this section we will demonstrate how to obtain the temperature T of a thermal atom cloud solely from the standard deviation of the cloud at an arbitrary TOF time and the known phase-space distribution $P(\vec{r},\vec{p})$ (eq. 4.8).

In order to deduce the temperature, the atoms are released from the magnetic quadrupole trap and left to expand ballistically. Therefore we need to calculate the spatial distribution of the expanding cloud.

The spatial distribution of the expanding cloud $n(\vec{r},t)$ depends on the initial phase-space distribution $P(\vec{r}_0,\vec{p})$. The atoms position $\vec{r}$ after the TOF time t is related to their initial position $\vec{r}_0$ and momentum $\vec{p}$ as $\vec{r} = \vec{r}_0 + \vec{p}\,t/m$. From this relation the spatial distribution $n(\vec{r},t)$ of the atoms

in TOF is given by

$$
\begin{aligned}
n(\vec{r},t) &= \int_p \int_{r_0} P(\vec{r}_0,\vec{p})\delta^3(\vec{r}-\vec{r_0}-\vec{p}t/m)d^3r_0 d^3p\,, && (4.15a)\\
&= Z_r^{-1}\int_{r_0} exp\left(-\beta(C\sqrt{x_0^2+y_0^2+4z_0^2}+mgy_0)\right) * \\
&\quad Z_p^{-1}\int_p exp\left(-\beta\frac{\vec{p}^2}{2m}\right)\delta^3(\vec{r}-\vec{r}_0-\vec{p}t/m)d^3r_0 d^3p\,, && (4.15b)\\
&= Z_r^{-1}\int_{r_0} exp\left(-\beta(C\sqrt{x_0^2+y_0^2+4z_0^2}+mgy_0)\right) * \\
&\quad Z_p^{-1} exp\left(-\frac{\beta}{2m}\left(\frac{m(\vec{r}-\vec{r}_0)}{t}\right)^2\right) d^3r_0\,; && (4.15c)
\end{aligned}
$$

where the integral over d^3p has been evaluated with the delta function $\delta^3(\vec{r}-\vec{r_0}-\vec{p}t/m)$. Equation (4.15c) can be expressed as the convolution of the spatial distribution $n(\vec{r})$ and momentum distributions $f(\vec{p})$ as:

$$
\begin{aligned}
n(\vec{r},t) &= \int_{r_0} n(\vec{r}_0) f\left(m(\vec{r}-\vec{r}_0)/t\right)d^3r_0, && (4.16)\\
&= (n\otimes f)(\vec{r}), && (4.17)
\end{aligned}
$$

where $n(\vec{r}_0)$ is the spatial distribution of the trapped atoms eq.(4.11) therefore zero TOF time $n(\vec{r}_0)=n(\vec{r},0)$, and $f\left(m(\vec{r}-\vec{r}_0)/t\right)$ is the momentum distribution eq.(4.13).

The convolution of two functions $f(x)$ and $g(x)$ is normally solved with Fourier transform F as $f\otimes g(x)=F^{-1}\left[F(f(x))F(g(x))\right]$ with F^{-1} the inverse Fourier transform. This identity simplifies the convolution integral but the Fourier transforms have to be calculated. The Fourier transform of the spatial distribution is difficult if not impossible to solve analytically because of the trapping potential that goes as $\sqrt{x^2+y^2+4z^2}$, making the different variables not separable. Moreover the symmetry is broken in the y axis due to the gravitational field. On the other hand the Fourier transform of the momentum distribution is standard and can be calculated easily.

Instead of solving this integrals to calculate the spatial distribution $n(\vec{r},t)$ at a given TOF time analytically we take another approach. In general the temperature is deduced from the expansion of

the cloud which measure the momentum distribution. Since the momentum distribution is isotropic along all axes thus we can calculate the temperature T by looking at the cloud expansion on just one of the axes. We chose to examine the expansion of the cloud along the x axis where the phase-space distribution $P(\vec{r},\vec{p})$ is symmetric and the cloud size along this axis can be measured experimentally. In the following, an analytical expression for the cloud size along the x axis at any TOF time is calculated and, from this size, a formula to calculate the temperature T is deduced.

The cloud size is represented by the standard deviation σ of the spatial distribution $n(\vec{r},t)$ along each of the axes. In general the standard deviation σ of a 1D distribution $P(X)$ in X is defined as

$$\sigma^2 = \left\langle (X - \langle X\rangle)^2 \right\rangle \tag{4.18a}$$

$$= \langle X^2\rangle - \langle X\rangle^2, \tag{4.18b}$$

where $\langle\ \rangle$ denotes the expectation value and $\langle X\rangle$ is the mean of the distribution and it is equal to $\langle X\rangle = \int_X XP(X)dX$.

After a TOF time t, the position of the particles in the x direction is given by $x(t) = x_0 + tp_x/m$. Thus the standard deviation of an expanding cloud along the x axis is

$$\sigma_t^2 = \langle x^2(t)\rangle - \langle x(t)\rangle^2. \tag{4.19}$$

Each of these expectation values can be calculated independently. The expectation value $\langle x(t)\rangle$ is equal to:

$$\langle x(t)\rangle = \left\langle x_0 + \frac{tp_x}{m} \right\rangle \tag{4.20a}$$

$$= \int_{r_0}\int_p \left(x_0 + \frac{tp_x}{m}\right) P(\vec{r}_0,\vec{p})\ d^3r_0 d^3p \tag{4.20b}$$

$$= \int_{r_0} x_0\ n(\vec{r}_0)d^3r_0 + \left(\frac{t}{m}\right)\int_p p_x f(\vec{p})d^3p \tag{4.20c}$$

$$= \cancelto{0}{\langle x_0\rangle} + \frac{t}{m}\cancelto{0}{\langle p_x\rangle} \tag{4.20d}$$

$$= 0, \tag{4.20e}$$

the expectation values $\langle x_0 \rangle$ and $\langle p_x \rangle$ are equal to zero because the spatial distribution $n(\vec{r_0})$ and the momentum distribution $f(\vec{p})$ are symmetric along x. The expectation value $\langle x^2(t) \rangle$ is calculated in a similar way as

$$\langle x^2(t) \rangle = \left\langle \left(x_0 + \frac{t p_x}{m} \right)^2 \right\rangle \tag{4.21a}$$

$$= \left\langle x_0^2 + \frac{2t x_0 p_x}{m} + \left(\frac{t}{m} \right)^2 p_x^2 \right\rangle \tag{4.21b}$$

$$= \langle x_0^2 \rangle + \frac{2t}{m} \cancelto{0}{\langle x_0 p_x \rangle} + \left(\frac{t}{m} \right)^2 \langle p_x^2 \rangle \tag{4.21c}$$

$$= \langle x_0^2 \rangle + \left(\frac{t}{m} \right)^2 \langle p_x^2 \rangle, \tag{4.21d}$$

where the cross term $\langle x_0 p_x \rangle = \langle x_0 \rangle \langle p_x \rangle$ is equal to zero since the momentum distribution $f(\vec{p})$ and space distribution $n(\vec{r})$ are independent to each other and symmetric along the x axis.

Replacing the results of the expectation values $\langle x(t) \rangle$ (eq. 4.20e) and $\langle x^2(t) \rangle$ (eq. 4.21d) into equation 4.19 one obtains:

$$\sigma_t^2 = \langle x^2(t) \rangle - \cancelto{0}{\langle x(t) \rangle^2}, \tag{4.22a}$$

$$= \langle x_0^2 \rangle + \left(\frac{t}{m} \right)^2 \langle p_x^2 \rangle \tag{4.22b}$$

$$\sigma_t^2 = \sigma_0^2 + x_{th}^2, \tag{4.22c}$$

The first term $\langle x_0^2 \rangle$ in eq. (4.22b) can be expressed as the standard deviation $\sigma_0^2 = \langle x_0^2 \rangle - \langle x_0 \rangle^2$ because the expectation value $\langle x_0 \rangle^2$ is zero. The cloud size along the x axis in a trapped state is σ_0 thus it is the cloud size a zero TOF time. The second term $x_{th}^2 = (t/m)^2 \langle p_x^2 \rangle$ in eq. (4.22c) is the increase of the cloud size due the thermal expansion in free fall. The calculation of σ_0^2 from the spatial distribution $n(\vec{r})$ and x_{th}^2 from the momentum distribution $f(\vec{p})$ is done in the following sections.

4.3.1 Obtaining the initial cloud size σ_0 from the spatial distribution $n(\vec{r})$

Using the spatial density $n(\vec{r})$ in eq.(4.11), one can calculate the expectation values $\langle x_0^2 \rangle$ inside the trap as

$$\langle x_0^2 \rangle = \int x^2 n(\vec{r}) \mathrm{d}^3 r \tag{4.23}$$

$$= Z_r^{-1} \int x^2 exp\left(-\beta C(\sqrt{x^2+y^2+4z^2}+\alpha y)\right) dx\, dy\, dz. \tag{4.24}$$

To calculate $\langle x_0^2 \rangle$ we do the same changes of variables as for calculating Z_r (eq. 4.9). In addition we have taken advantage that the distribution along the new coordinates x and y axis is symmetric so the expectation value $\langle x_0^2 \rangle$ is calculated as $\langle x_0^2 \rangle = \langle y_0^2 \rangle = \langle \rho_0^2 \rangle / 2$. With the transformation of coordinates from Cartesian to spherical ρ_0 can be express as $\rho_0 = r sin\theta$. Giving as a result:

$$\langle x_0^2 \rangle = \frac{1}{4Z_r} \int exp\left(-\beta C r(1+\alpha cos\theta)\right) r^4 sin^3\theta dr d\theta d\phi, \tag{4.25}$$

$$= \frac{1}{4Z_r} \int_0^{2\pi} d\phi \int_0^{\pi} sin^3\theta d\theta \int_0^{\infty} exp\left(-\beta C r(1+\alpha cos\theta)\right) r^4 \mathrm{d}r. \tag{4.26}$$

The integral over ϕ is straightforward, and the integral over r is the Gamma function $\Gamma(t) = \int_0^\infty x^{t-1} e^{-x} dx$. With a change of variables $\beta C(1+\alpha cos\theta) r \to x$, the integral over r is solved and the expectation values $\langle x_0^2 \rangle$ is left with dependence on the angle θ as:

$$\langle x_0^2 \rangle = \frac{12\pi}{Z_r \beta^5 C^5} \int_0^{\pi} \frac{sin^3\theta}{(1+\alpha cos\theta)^5}\, d\theta. \tag{4.27}$$

To simplify from this trigonometric function to a polynomial function another change of variables $cos\theta \to x$ is done, resulting in

$$\langle x_0^2 \rangle = \frac{12\pi}{Z_r \beta^5 C^5} \int_{-1}^{1} \frac{1-x^2}{(1+\alpha x)^5}\, dx. \tag{4.28}$$

The integral over x is solved after partial fractions decomposition[4] to the fraction $(1-x^2)/(1+\alpha x)^5$. The last change of variable $1-\alpha x \to y$ is performed[5] giving as a result

$$\int_{-1}^{1} \frac{1-x^2}{(1+\alpha x)^5}\, dx = \frac{4}{3}\frac{1}{(1-\alpha^2)^3} \tag{4.29}$$

where the integral over y was evaluated and after algebraical simplification the final result in eq. 4.29 is obtained. Replacing the result of the previous integral (eq. 4.29) in the expectation value $\langle x_0^2 \rangle$ (eq. 4.28) and using the value of Z_r (eq. 4.9) one gets

$$\boxed{\langle x_0^2 \rangle = \frac{4}{C^2\beta^2(1-\alpha^2)} = \sigma_0^2.} \tag{4.30}$$

where σ_0 is considered to be the size of the cloud at zero TOF time. A discussion of how this cloud size σ_0 behaves at different magnetic gradients B' and temperatures T is presented later in sect. 4.3.4.

4.3.2 Obtaining the thermal expansion $x_{\mathbf{th}}^2$ from the momentum distribution $f(\vec{p})$

The thermal expansion $x_{th}^2 = (t/m)^2\langle p_x^2 \rangle$ has a dependence on the expectation value $\langle p_x^2 \rangle$ which can be calculated from the momentum distribution $f(\vec{p})$ as

$$\langle p_x^2 \rangle = \int_p p_x^2 f(\vec{p}) dp_x dp_y dp_x, \tag{4.31a}$$

$$= \left(\frac{1}{2\pi m k_B T}\right)^{3/2} \int_{p_x}\int_{p_y}\int_{p_z} p_x^2 exp\left(-\frac{p_x^2+p_y^2+p_z^2}{2mk_BT}\right) dp_x dp_y dp_x, \tag{4.31b}$$

Instead of solving these integrals, $\langle p_x^2 \rangle$ can easily be calculated with respect to the kinetic energy

[4] $\frac{(1-x^2)}{(1+\alpha x)^5} = \frac{(1-\alpha^{-2})}{(1+\alpha x)^5} + \frac{(2\alpha^{-2})}{(1+\alpha x)^4} - \frac{(\alpha^{-2})}{(1+\alpha x)^3}$.

[5] $\int_{-1}^{1} \frac{1-x^2}{(1+\alpha x)^5}\, dx = \left(1-\frac{1}{\alpha^2}\right)\left(-\frac{1}{\alpha}\right)\int_{1+\alpha}^{1-\alpha} \frac{dy}{y^5} + \left(\frac{2}{\alpha^2}\right)\left(-\frac{1}{\alpha}\right)\int_{1+\alpha}^{1-\alpha} \frac{dy}{y^4} - \left(\frac{1}{\alpha^2}\right)\left(-\frac{1}{\alpha}\right)\int_{1+\alpha}^{1-\alpha} \frac{dy}{y^5}$

E_K as:

$$\begin{aligned} \langle E_K \rangle &= \frac{1}{2m}\langle \vec{p}^{\,2} \rangle && (4.32a) \\ &= \frac{1}{2m}\langle p_x^2 + p_y^2 + p_z^2 \rangle && (4.32b) \\ &= \frac{3}{2m}\langle p_x^2 \rangle && (4.32c) \end{aligned}$$

From the equipartition theorem the kinetic energy $\langle E_K \rangle$ relates with the temperature T as:

$$\langle E_K \rangle = \frac{3}{2} k_B T. \tag{4.33}$$

From equations (4.32c) and (4.33) we can deduce that the expectation of $\langle p_x^2 \rangle$ is

$$\langle p_x^2 \rangle = m k_B T. \tag{4.34}$$

substituting this result in x_{th}^2 we obtain

$$\boxed{x_{th}^2 = \frac{t^2}{m}(k_B T).} \tag{4.35}$$

Where x_{th}^2 is the thermal expansion of the cloud, which depends linear on temperature T and quadratically on TOF time t. Some methods of temperature calculation assume a point as initial cloud size $\sigma_0 = 0$, for these methods the size of the cloud at free fall will be equal to this thermal expansion x_{th}.

4.3.3 Deducing the temperature T of the cloud from its size σ_t after TOF

Analytical expressions for the initial cloud size σ_0 and the cloud thermal expansion x_{th} were deduced in the previous sections and can now be replaced in the expression for the cloud size σ_t after TOF

(eq. 4.22c) giving as a result

$$\sigma_t^2 = \underbrace{\frac{4}{C^2(1-\alpha^2)}(k_B T)^2}_{\text{initial cloud size}^2} + \underbrace{\frac{t^2}{m}(k_B T)}_{\text{thermal expansion}^2}. \tag{4.36}$$

This σ_t gives the size of the expanding cloud after a TOF time t along the x axis, where the cloud has been initially held in a magnetic quadrupole trap. It contains the information of the initial cloud size σ_0 from the quadrupole trap and the thermal expansion x_{th} depending on TOF time t. A broader discussion of the parameters that influence the cloud size in a trapped state and after a ballistic expansion is presented in sect. 4.3.4. In that section the short and long TOF times regimes introduced before are also discussed.

By reorganising the expression for the cloud size squared σ_t^2 eq.(4.36) after TOF time in terms of $k_B T$ results in:

$$(k_B T)^2 + \frac{C^2 t^2 (1-\alpha^2)}{4m}(k_B T) - \frac{C^2(1-\alpha^2)}{4}\sigma_t^2 = 0. \tag{4.37}$$

This is a quadratic equation in T that can be solved with the quadratic formula giving as a result:

$$\boxed{T = \frac{C^2 t^2 (1-\alpha^2)}{8 m k_B}\left(\sqrt{1 + \frac{16 m^2 \sigma_t^2}{C^2 t^4 (1-\alpha^2)}} - 1\right).} \tag{4.38}$$

This formula is an accurate and analytical expression to calculate the temperature T of an expanding atom cloud, after being initially trapped in a magnetic quadrupole trap from a single TOF time t. This formula is valid for all TOF times since it considers the trapping potential and gravity.

The experimental information needed to calculate the temperature T with equation 4.38 is the trapping potential $\propto C$, the TOF time t and the standard deviation σ_t of the spatial distribution of the expanding cloud along the symmetric axis x. The uncertainty of any of this variable generates an uncertainty on the temperature. Precise measurements of the magnetic gradient are done by finding the levitation current and comparing with the theoretical levitation gradient of 15G/cm. The TOF can be verified by measuring the reaction time of the coils switching off, ether measuring the current across the coils or measuring the magnetic gradient as a function of switch off time. The remain variable to determine is the standard deviation of the cloud σ_t. Since an analytical expression for

the 1D spatial distribution is unknown, fit function to calculate the standard deviation σ_t can not be used. Therefore, an experimental method to calculate σ_t was developed and is described in sect. 4.4.

4.3.4 Examination of the cloud size σ_t after TOF

In this section, a study of how the initial cloud size σ_0 and the cloud size σ_t after TOF are influenced by different parameters such as temperature T, magnetic gradient B' and TOF time t is carried out. Also, the effect of gravity on the initial cloud size will be studied. Furthermore the short and long TOF time regimes introduced in sect. 4.1 are discussed.

The cloud size σ_t after TOF along the x axis is directly related to the squared standard deviation σ_t^2 of the atom spatial distribution (eq. 4.36), which shows explicitly the two factors that contribute to short and long TOF time regimes. The first term σ_0^2 is the squared standard deviation of the spatial distribution of the trapped state, which depends only on the trapping potential U and the temperature T. The second term x_{th}^2 is the thermal expansion which increases with TOF time t^2 and depends linearly on the cloud temperature T. At short TOF times the cloud size σ_t is dominated by σ_0^2, and at long TOF times by the thermal expansion x_{th}^2.

From the parameters that are studied (T, B', g, t) I will start analysing the effect of the gravitational field in combination with the magnetic gradient B' and the temperature T in the cloud size σ_t. The gravitational field influences the initial cloud size σ_0 as it deforms the trapping potential. In free fall all atoms are pulled down evenly therefore the overall effect is the dropping of the cloud, while the cloud shape is not affected by gravity. Looking at σ_0^2 (eq. 4.30) the effect of the gravitational field is contained in the term[6] $\alpha = mg/C$. The increase in cloud size along the x axis due to gravity is proportional to the *gravitational factor*[7] equal to $1/(1-\alpha^2)$. From which can be seen that the gravitational field plays a more important role for the cloud size when α is close to one, meaning clouds in weak magnetic traps with small C. In weak traps the atom clouds are more

[6]The factor α is equal to one when $C = mg$ and this value of C is produced when the magnetic gradient is equal to $15G/cm$ for the specific case of ^{87}Rb atoms in the $F = 2, m_F = 2$ state.

[7]The gravity factor is always bigger or equal to 1. Hence I will refer to the effect of this gravitational factor as increase on size, where the percentage increase is given by $(gravitational factor - 1) * 100$.

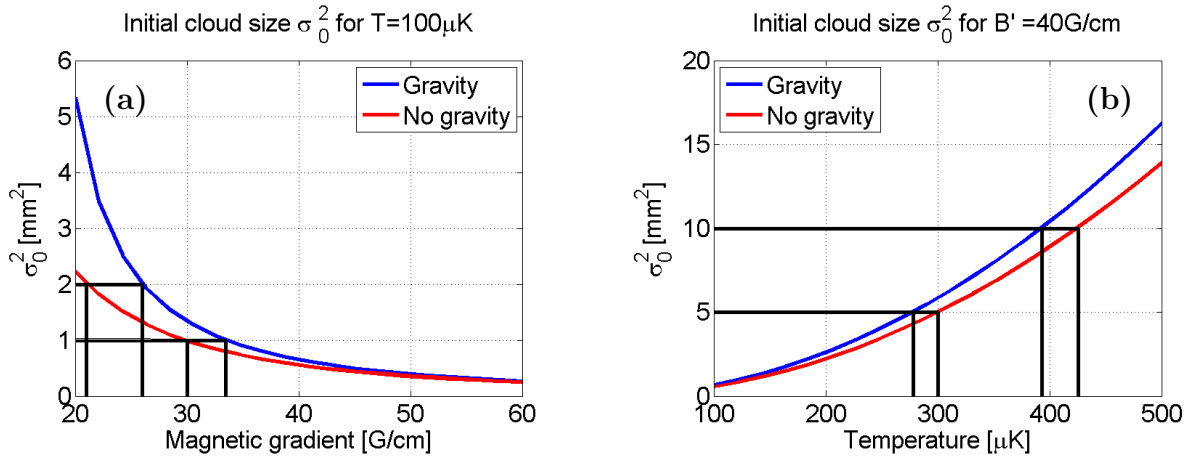

Figure 4.5: *Initial cloud size squared σ_0^2 as a function of magnetic gradient B' and temperature T.* These plots show the initial cloud size squared σ_0^2 at different magnetic gradient and temperatures with and without gravity. In (a) the initial cloud size square σ_0^2 has been plotted for a range of magnetic gradients from 20 to 60G/cm at a constant temperature $T = 100\mu$K. In general σ_0^2 is bigger at low magnetic gradients because the atom cloud is loosely hold. Comparing gravity and no gravity cases in (a) can be concluded that the gravitational field widen the atoms cloud at low magnetic gradients and almost has no effect for high magnetic gradients. In (b) the initial cloud size squared σ_0^2 is plotted for a range of temperature from 100 to 500μK keeping the magnetic gradient B' constant at 40G/cm. On this plot, it can be seen that the initial cloud size squared σ_0^2 has a quadratic dependence with temperature and the effect of the gravitational field seems to be bigger for hot clouds, but from gravity factor one knows that the proportional difference is constant.

deformed by the gravitational field than clouds in strong magnetic traps as can be seen in figure 4.5.

Figure 4.5 shows the initial cloud size squared σ_0^2 with gravity ($\alpha = mg/C$) and without gravity ($\alpha = 0$) varying the magnetic gradient B' (a) and the temperature T (b). In general, σ_0^2 grows with temperature T and shrinks with the magnetic gradient B'. In both cases, constant temperature T and constant magnetic gradient B', the initial cloud size squared σ_0^2 is bigger with gravity than without gravity. By comparing the plots with and without gravity one can see how much the gravitational factor increase the initial cloud size squared σ_0^2. For example, in figure 4.5 (a) the increase in size due to gravitational factor is more than double for 20G/cm and just few % for magnetic gradients higher than 40G/cm. The gravitational factor produces an increase on cloud size of less than 1% at magnetic gradients higher than 150G/cm, and can be considered negligible.

In figure 4.5 (a) it can be seen that for an increased in initial size squared from 1 to 2mm^2 the

magnetic gradient B' is decrease from 33.5 to 26G/cm (23%) in the gravity case and from 30 to 21G/cm (30%) in the no gravity case. Therefore it can be concluded that the increase of the initial size is higher for the gravity case than the no gravity case. On the other hand in figure 4.5 (b) can be seen that the temperature corresponding to $\sigma_0^2 = 5\text{mm}^2$ varies from 300 to 278μK if gravity is consider, this difference corresponds to a variation of 8% in temperature. A similar difference in temperature is obtain for $\sigma_0^2 = 10\text{mm}^2$.

The question now to be asked is why is the initial cloud size σ_0 along the x direction affected by gravity? Since the gravitational field is acting along the y axis. To respond to this question we need to look at the spatial distribution of the whole cloud along the different axes. Starting with the case of weak magnetic trapping where α is close to one. In this case the spatial distribution along the y axis is pronouncedly deformed by gravity and follows a distribution similar to fig. 4.4 (gravity case). In this distribution the atoms are more probable to be found below the quadrupole trap center. Away from the center of the trap the atoms confinement is stronger but wider, making it possible for the atoms below the magnetic trap center to occupy a wider region. As a result the standard deviation of the distribution of the atoms along the x and z axis is bigger. On the case of strong magnetic traps $\alpha \ll 1$ the shifting of the trap distribution along the y axis is nearly null (see eq. 4.12b) and the distribution and cloud size along the other axes gets unaffected as shows fig. 4.5 (a).

Another aspect to consider is at which point the distribution of the cloud is predominated by the initial cloud size squared σ_0^2 or by the thermal expansion x_{th}^2. From σ_t^2 eq. (4.36) is known that the initial cloud size σ_0 does not change with time, just the thermal expansion x_{th}^2 is related to TOF time. The TOF time needed to equalise the thermal expansion x_{th}^2 with the initial cloud size squared σ_0^2 is presented in figure 4.6. Before this TOF time the cloud size will be dominated by the initial cloud size σ_0^2 and after this TOF time by the thermal expansion. Therefore I will refer to this time as the TOF time boundary. The TOF time boundary gives the transition between the short and long TOF time regimes.

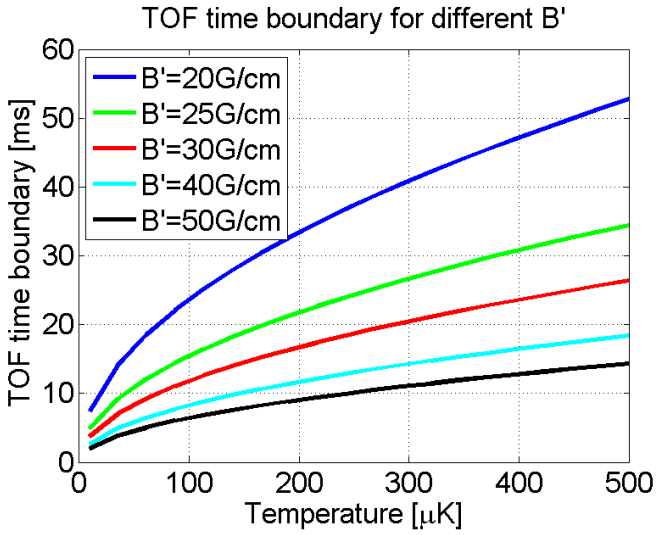

Figure 4.6: *TOF time boundary as a function of magnetic gradient B' and Temperature T.* In this plot the TOF time boundary ($t = \sqrt{4mk_BT/C^2(1-\alpha^2)}$) when the thermal expansion x_{th}^2 equalise the initial cloud size square σ_0^2 is plotted. The TOF time boundary is plotted as a function of temperature from 10 to 500μK for a range of magnetic gradient B' from 20 to 50G/cm. In general TOF time boundary is higher at low magnetic gradients because the atom cloud is loosely hold increasing the initial cloud size σ_0. On this plot can bee seen that for cold clouds the TOF time boundary is shorter, which is not intuitive. The explanation for this counter-intuitive effect is that the initial cloud size depends quadratically in temperature and the thermal expansion depends linearly, which makes hot clouds big from the start and the thermal expansion needs more time to reach the same size.

Figure 4.6 shows the TOF time boundary ($t = \sqrt{4mk_BT/C^2(1-\alpha^2)}$) for different magnetic gradients B' and temperatures T. The TOF time boundary is higher for weak magnetic trap since the initial cloud size σ_0 is bigger. Looking at the temperature (T) dependence, the TOF time boundary is longer for hot clouds as can be seen in fig. 4.6. This result is counter-intuitive since the thermal expansion x_{th}^2 is faster for hot clouds because it has a linear dependence on temperature T. But the initial cloud size σ_0^2 also depends on temperature T and does it quadratically. So in order to double the initial size squared $2\sigma_0^2$ one has to let the cloud expand for longer.

The convention for the thermal expansion predominating is when the cloud size σ_t at TOF is much bigger than the initial cloud size σ_0. This condition affects when the common TOF technique can be used, while the temperature determination with our formula (eq. 4.38) is reliable for both short or long TOF regimes. Making our method of temperature determination more accurate at short TOF time regime than the common TOF technique as will be shown later.

Until now I have introduced the common TOF technique and its limitations (sect. 4.1), then we have studied the phase-space distribution of the atom cloud trapped in a magnetic quadrupole potential and consider the effect of gravity in the spatial distribution (sect. 4.2). Followed by the development of a formula for temperature determination and the examination of the cloud size after TOF time (sect. 4.3). Everything previously established is the theoretical framework for temperature determination and before applying it to the experiment date a method to calculate the cloud size σ_t at any TOF time is developed in the next section.

4.4 Experimental determination of the standard deviation σ_t from absorption images

For long TOF times a 2D Gaussian fits reasonably the spatial distribution of the atom cloud since it is dominated by the momentum distribution $f(\vec{p})$ that follows a Gaussian distribution. For short TOF times the density profile obtained from pictures cannot be fitted to a theoretical distribution since the spatial distribution at TOF is unknown analytically. This problem raises the necessity to determine the standard deviation σ_t in some other way more reliable than a Gaussian fit for all TOF times. In this section is explain how the size of the cloud σ_t is obtain by analysing the absorption images.

All the information of the atom cloud is obtained from the optical density OD (fig. 4.7 (a)) which is calculated as explained in sect. 3.4.1. Since there are areas of the optical density without relevant information just adding noise, a region of interest (ROI) is specified in such a way that is centred with the cloud and covers the cloud up to 99%. Due to the fact that the image shows only parts of the cloud, a special treatment of the data is done as explained later. The cloud is shifted to the left side of the camera chip and for weak traps with magnetic gradient less than 25G/cm the atoms cloud reaches the bottom of the science chamber[8] at 3ms TOF (see fig. 4.7).

In order to calculate the mean of the distribution and the region of interest ROI we need to determine the cloud center (C_x, C_y). The cloud center (C_x, C_y) is calculated by averaging the pixel

[8]The optical density image has been cut at the bottom where the science chamber ends, outside the chamber there is no relevant information for the optical density.

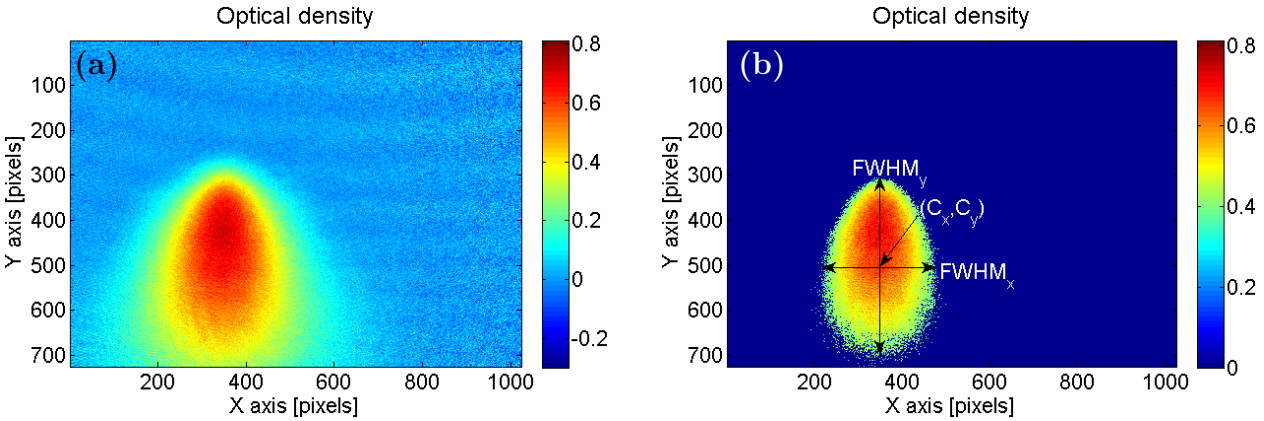

Figure 4.7: *Optical density and cutoff to calculate cloud center.* The optical density (a) of a cloud after 3ms TOF time. The cloud has been released from a magnetic trap with a gradient of 20G/cm. The gravitational field is acting along the y axis downwards. In (b) the optical density cutoff of the same cloud as (a) is shown. The optical density cutoff is the area $A(X,Y)$ with group of coordinates X,Y of the optical density that is above the half maximum. This area $A(X,Y)$ is used to calculate the cloud centre (C_x, C_y) according with eq. (4.39). Also from the selected area $A(X,Y)$ the full width half maximum (FWHM) along each axes is calculated. For information of how to calculate FWHM refer to text.

values X, Y of the optical density that are above the half maximum (fig. 4.7 (b)) as

$$C_x = \sum_x \frac{X}{N} \quad \text{and} \quad C_y = \sum_y \frac{Y}{N}; \tag{4.39}$$

where N is the number of pixel above half maximum. The difference between the maximum and minimum values of the group of coordinates X gives the full width half maximum (FWHM_x) of the atom distribution along the x axis. And in the same way the FHWM_y is determined for the y axis . The region of interest ROI is defined as the elliptical area covered by $8{\cdot}\text{FWHM}_{x,y}$ in each direction, corresponding to $3.9\sigma_{QT}$ and 99.6% covered of the quadrupole trap distribution (fig. 4.1 (b)). For a Gaussian distribution this region of interest ROI is equivalent to $9.4\sigma_G$ thus covers ≈100% of the Gaussian distribution (fig. 4.1 (a)). Outside the region of interest ROI the density distribution is assumed to be zero.

Having determined the cloud centre (C_x, C_y) and the region of interest ROI, the cloud size define as the standard deviation of the atoms distribution is obtained in the following way. Since just the spatial distribution in one of the axes is needed (x axis) a projection of the 2D optical density (fig.

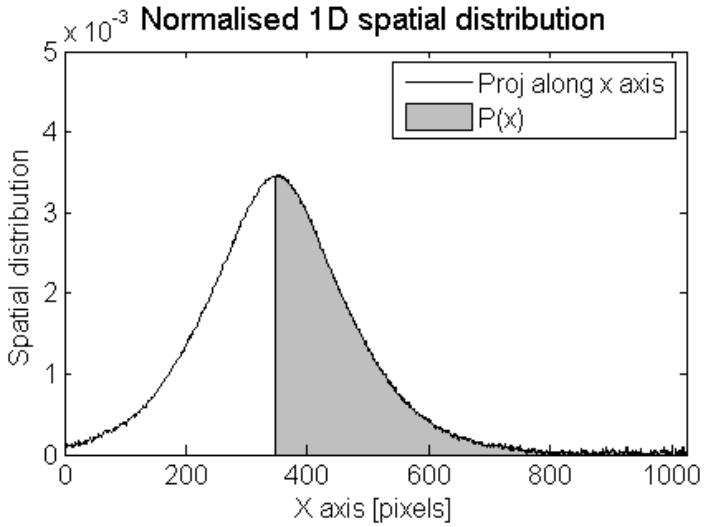

Figure 4.8: *Normalised 1D spatial distribution.* This plot shows the resulting normalised 1D spatial distribution (black line). This 1D spatial distribution is the result of summing the optical density OD (fig. 4.7) along the y axis. Also this distribution has been cut at the mean of the distribution C_x and normalised according to eq. 4.41 (grey area).

4.7 (a)) is done by integrating over the y axis. This integration gives the 1D spatial distribution along x (fig. 4.8) from where the standard deviation σ_t is obtained.

The standard deviation σ_t of the 1D spatial distribution along x is calculated using the general definition of the standard deviation introduced in eq. (4.18a). Therefore the 1D distribution is normalized and the mean of the distribution[9] has to be calculated. Since the experimental 1D spatial distribution is discrete we will sum along the x axis in order to calculate the expectation values.

In many cases the images have part of the left side of the distribution missing (because the cloud is not centred in the CCD which is an advantage as explain later). Although the distribution is assumed to be symmetric along the x axis so only half of the distribution is needed to calculate σ_t. In order to have a reliable sample of the distribution, the projection is cut at the mean C_x along the x axis and just the right side of the projection (fig. 4.8) is considered for normalization and

[9]Since the spatial distribution along the x axis is symmetric calculate the cloud center along this axis is equivalent to calculate the mean of the distribution.

calculation of the standard deviation σ_t. The standard deviation σ_t is then given by

$$\sigma_t = Conv\sqrt{2\sum_x P(x)(x-C_x)^2}, \quad \text{where} \tag{4.40}$$

$$P(x) = \frac{\sum_y OD(x,y)}{2\sum_{y,x} OD(x,y)} \quad \text{with} \quad C_x < x < 1024, \tag{4.41}$$

where x and y refer to the pixels of the optical density OD (fig. 4.7) and $Conv = pixel\ size/magnification$ is the conversion factor from pixels to real space. This approach (eq. 4.40) is only valid if the right half of the distribution is complete meaning that the cloud distribution should not exceed the field of view towards the right side in fig. 4.7. This condition is achieved in most of the cases since the cloud is not centred on the CCD.

The data analysis used to determine the standard deviation of the cloud has been tested with theoretical distributions. Since we do not have a theoretical column density for the cloud after TOF time, the Gaussian and quadrupole trap distribution were tested individually. The column density[10] of a 3D Gaussian distribution is equal to a 2D Gaussian distribution. In contrast, the 3D quadrupole trap density distribution (eq. 4.11) is not possible to integrate analytically along the z axis since the coordinates are coupled by $\sqrt{x^2+y^2+4z^2}$. Instead of integrating the quadrupole trap distribution a 2D distribution is created by assuming $z = 0$ and renormalising. In order to make the distributions more realistic a random noise was added.

The 2D normalised Gaussian distribution used is given by

$$G_{2D}(x,y) = \frac{1}{2\pi\sigma_{xG}\sigma_{yG}} exp\left(-\frac{(x-x_c)^2}{2\sigma_{xG}^2} - \frac{(y-y_c)^2}{2\sigma_{yG}^2}\right), \tag{4.42}$$

where the standard deviations $(\sigma_{xG}, \sigma_{yG})$ and the distribution center (x_c, y_c) are known. The calculated standard deviation σ_t has a 0.7% error from the theoretical value σ_{xG} without noise and 2% error in the worse case with noise.

The 2D quadrupole trap distribution used is given by

$$QT_{2D}(x,y) = \frac{(C\beta)^2}{2\pi} exp\left(-C\beta\sqrt{(x-x_c)^2+(y-y_c)^2}\right), \tag{4.43}$$

[10]The column density is integral of the 3D spatial distribution along the detection axis z.

with gravity not included[11]. An important fact to notice is that the standard deviation along x and y axes are the same and equal to $\sigma_{xQT} = \sigma_{yQT} = \sqrt{3}/C\beta$, which is a different result than the 3D case where $\sigma_{0x} = 2/C\beta$ (eq.4.30). This fact shows how the different variables are coupled in comparison to the Gaussian distribution where the variables and the standard deviation in each axis are independent.

In this 2D quadrupole trap distribution it is important to select a sufficient long region of interest ROI, otherwise the calculated standard deviation is underestimated. By selecting a ROI equal to 8·FWHM the calculated standard deviations reached errors $\leq 5\%$ from the theoretical value σ_{xQT} with and without noise.

On the other hand the calculation of the standard deviation of experimental data requires a reliable background substation, since each pixel is weighted by the 1D distribution and will contribute towards the standard deviation σ_t.

4.5 Temperature out of a single shot image

After developing a formula for the determination of the temperature out of a single shot (sect. 4.3) and a method to obtain the standard deviation σ_t for data analysis (sect. 4.4) we apply this methods to experimental data. In this section it will be verified that the developed formula (eq. 4.38) gives similar values of temperature T in comparison with the common TOF technique. The test is performed for different magnetic gradients B' and temperatures T. The magnetic gradient varies from weak at 20G/cm to relatively stronger traps at 50G/cm. The temperature varies with the different magnetic gradients.

In the analysis of the data it is possible to observe experimentally the deformation of the cloud in weak traps due to the gravitational field. Moreover the cloud size is also calculated with a Gaussian fit and it is possible to see the deviation from the calculation of σ_t via data analysis described in sect. 4.4.

This section is organised as follows: starting with a description of the atom cloud preparation, followed by the experimental results for the cloud size σ_t at different magnetic gradients B' and

[11] For no gravity case $\alpha = 0$.

TOF times t, continuing with the results on temperature determination developed in sect. 4.3 and the common TOF technique, and finally a comparison between our method and the common TOF technique.

4.5.1 Cloud preparation

The atom cloud has been produced in the same way for all magnetic gradients. The cloud is prepared by loading the 3D MOT, followed by optical molasses for 15ms. The atoms are then optically pumped to the $F = 2, m_F = 2$ state and magnetically trapped at 62G/cm in the weak axis of the transport coils. From there the cloud is transported to the science chamber in 0.9s and transferred to the Feshbach coils at 66G/cm within 1s. Once the cloud has been captured in the Feshbach coils the current is ramp down in 0.5s to the desired magnetic field gradient B' between 20 to 50G/cm. The cloud is held in the trap for one second for rethermalisation purposes. Then absorption imaging pictures are taken at different TOF times (3, 5, 7, 10, 15 and 20ms).

4.5.2 Experimental results of the cloud size σ_t

The size of the cloud (σ_t) is calculated in two ways, via data analysis (sect. 4.4) and by fitting a 1D Gaussian, both methods used the normalised 1D projection of the optical density along the x axis (fig. 4.8). The calculated cloud size for the different magnetic gradient and TOF times is presented in fig. 4.9.

The calculation of σ_t with data analysis agrees with the Gaussian fits at long TOF times and high magnetic gradients in fig. 4.9. At short TOF times, both methods deviated from each other. The Gaussian fit underestimates the cloud size at short TOF times, since the convolution of the quadrupole trap distribution and the Gaussian distribution would be similar to a Gaussian with a smaller width (fig. 4.1).

A rough estimation when both methods will agree is the TOF time boundary TOF_B. This time ensures that cloud size σ_t has increased to $\sqrt{2}$ from the initial cloud size σ_0 but does not assure that the distribution is Gaussian. The TOF boundary time TOF_B for each magnetic gradient is shown as a vertical black line in fig. 4.9. The TOF_B is calculated with the temperature of the cloud

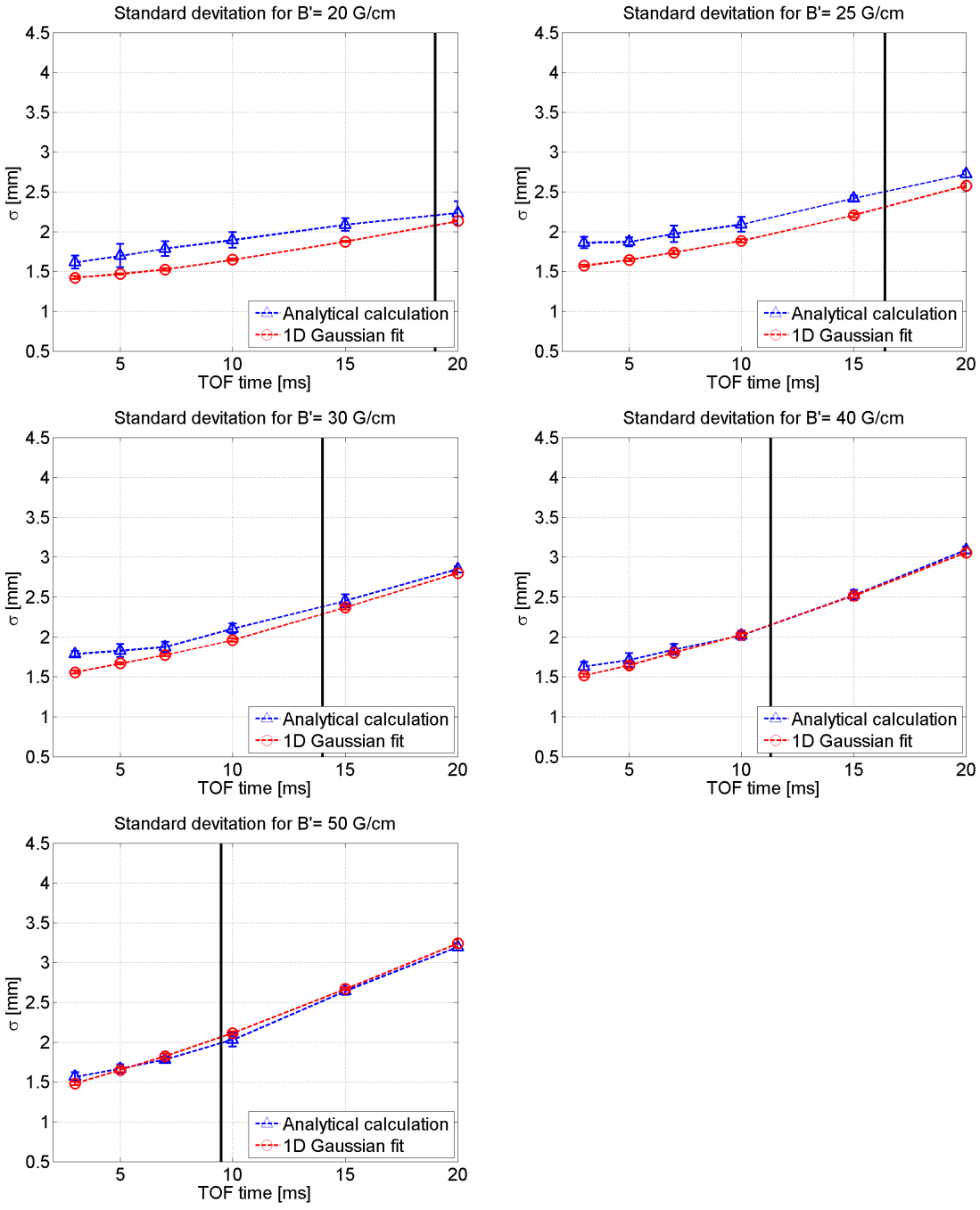

Figure 4.9: *Cloud size for tested magnetic gradient at different TOF times.* The plots show the cloud size σ_t after release from the magnetic quadrupole traps with different magnetic gradients (20, 25, 30, 40 and 50G/cm) and expansion for a given TOF time. The calculation of the cloud size σ_t is done with two different methods, analytically (see sect. 4.4) and with a 1D Gaussian fit. Each point in these plots is the average of the cloud size σ_t from six different pictures that have been prepared in the same way (sect. 4.5.1). The two different methods of size calculation used the same six images. The errorbars are calculated as the standard error of the six cloud sizes.

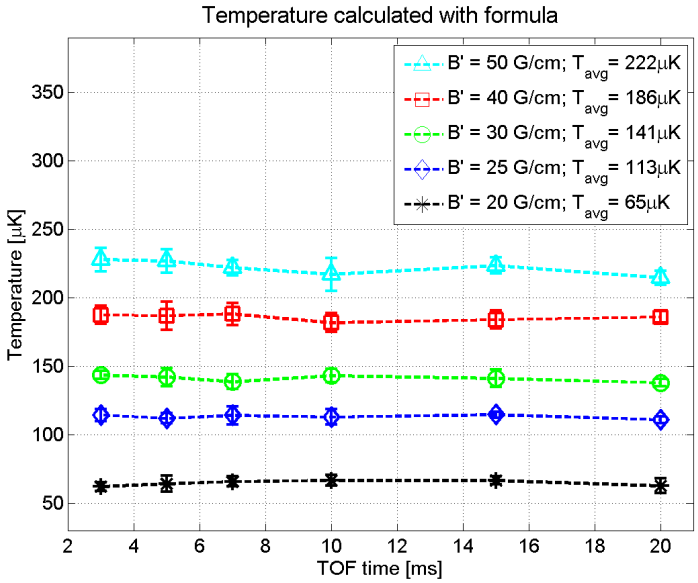

Figure 4.10: *Temperature calculation with deduce formula.* Each data point has been calculated using the deduce formula eq. (4.38) and the analytically calculated cloud size σ_t (fig. 4.9) with it respective TOF time and magnetic gradient B'. The error in temperature comes from the inherited error from the cloud size $\delta\sigma$. This temperature calculation is done for the different magnetic gradients 20, 25, 30, 40 and 50G/cm. The calculated temperatures follow a linear tendency with small fluctuation at various TOF times. The average temperature from different TOF for each magnetic gradient is shown in the plot legend.

deduced in the next section and the respective magnetic gradient B'. Weak traps need more time to reach a Gaussian distribution than tight traps. This result is not surprising since it is known that clouds in weak traps are deformed more by gravity than tight traps.

From the obtained cloud size σ_t shown in fig. 4.9 can be concluded that the analytical calculation by analysis of the cloud size is comparable in few percent with σ_G for TOF time after TOF_B, with just 5 and 6% difference in the worse cases for 20 and 25G/cm respectively.

4.5.3 Temperature calculation

Having determined the cloud size σ_t for the different TOF times and magnetic gradients B' (fig. 4.9) the temperature T was calculated first with the used of the formula eq.(4.38) and secondly with the common TOF technique. The first method used the calculation via analysis of the cloud size (σ_t), the corresponding magnetic gradient B' and TOF times. The common TOF technique used

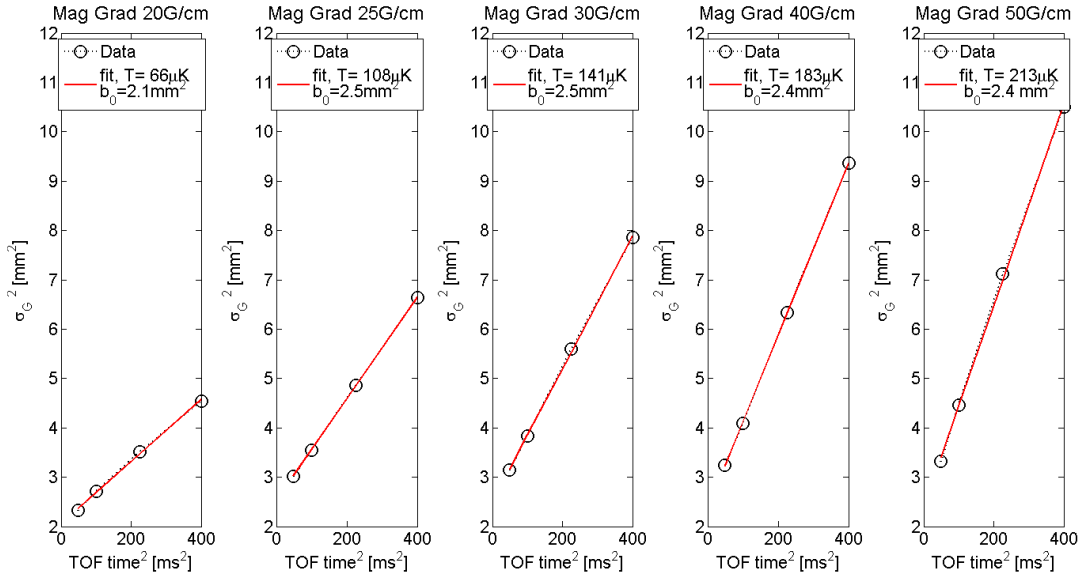

Figure 4.11: *Temperature calculation with common TOF technique.* In these plots the results of the temperature calculated with the common TOF technique are shown for the different magnetic gradients. The cloud sizes σ_G are calculated with the 1D Gaussian fit. For better reliability the longest TOF times are used (7 to 20ms).

the cloud size calculated by the 1D Gaussian fit σ_G and the corresponding TOF times. To make the results of the common TOF technique more reliable TOF times from 7 to 20ms have been used.

The results for the temperature calculation with equation (4.38) are presented in figure 4.10. The plot shows the temperature calculated for the different magnetic gradients B' at different TOF times. As expected the temperature calculated for each magnetic gradient B' remains constant with just small fluctuations at different TOF times. The fluctuation on the temperature goes from 7% on the worst case for 20G/cm and just 3% in the best case for 25G/cm.

For the common TOF technique the temperature was calculated by fitting a straight line to the plot σ_G^2 vs TOF^2 (fig. 4.11), where the slope a of the line is proportional to T according to eq.(4.2). A resume of the temperatures calculated with both methods is presented in table 4.1.

Since the clouds are prepared in the same way for all magnetic gradients it is expected that the temperatures are in some way related. By lowering the magnetic gradient adiabatically the phase-space density PSD is conserved. By equalising the initial and finals PSD the temperature of

the cloud T_f is predicted from the initial cloud temperature T_i and magnetic gradients as

$$PSD_i = PSD_f \quad \text{with} \quad PSD = n(0) \cdot \lambda_{dB} \propto \left(C^3\beta^3(1-\alpha^2)^2\right) \cdot T^{-3/2}, \tag{4.44}$$

whit $n(0)$ the peak density of the quadrupole trap (eq. 4.11). Solving for T_f one obtains

$$T_f = T_i \left(\frac{B'_f}{B'_i}\right)^{2/3} \left(\frac{1-\alpha_f^2}{1-\alpha_i^2}\right)^{4/9}. \tag{4.45}$$

The predicted temperature T_f is similar to the one use by Davis *et al.* [17] where they calculated the temperature for the increase on the magnetic gradient as $T_f = T_i \left(\frac{B'_f}{B'_i}\right)^{2/3}$. Equation (4.45) is more complete since considers the effect of gravity on the density distribution. The predicted temperatures with eq. (4.45) are included in table 4.1 and have been plotted with the experimental calculation of the temperature in figure 4.12. The temperature calculated experimentally agrees with the predicted temperature with just few percent difference except for 20G/cm magnetic gradient, this big difference (27%) is due to the magnetic gradient being too low to capture the hot atoms, therefore evaporative cooling is carried out in a similar way as [16].

B' [G/cm]	T_{form} [μK]	T_{comm} [μK]	T_{pred} [μK]	Diff$_{form-comm}$ [%]	Diff$_{form-pred}$ [%]	Diff$_{comm-pred}$ [%]
20	65 ± 4	66	82	2	27	24
25	113 ± 3	108	114	5	<1	6
30	141 ± 5	141	140	0	<1	<1
40	186 ± 5	183	180	2	3	1
50	222 ± 10	213	213	4	4	0

Table 4.1: *Temperature of the cloud at different magnetic gradients.* This table shows the collection of the temperature calculated by various methods: T_{form} is the average temperature calculated with the formula (eq. 4.38) for all TOF time shown in fig. 4.10, T_{comm} is the temperature calculated with the common TOF technique shown in fig. 4.11, and T_{pred} is the temperature predicted with equation (4.45).

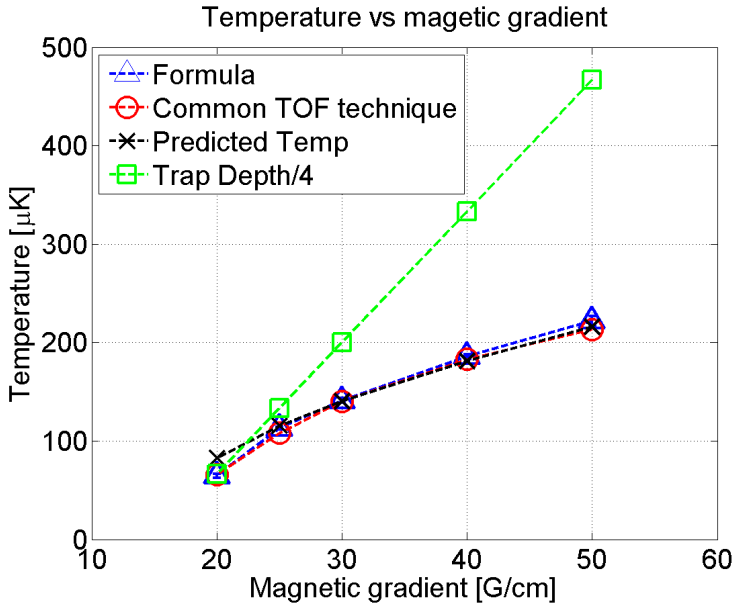

Figure 4.12: *Temperature variation with magnetic gradient.* This plot shows the temperature of the cloud calculated with the common TOF technique and with formula eq. (4.38). As well the predicted temperature given by eq. (4.45) is shown. Also it is plotted the a fraction of the trap depth which after thermalisation is reached.

4.5.4 Comparison of methods for temperature calculation

In this section both methods of temperature calculation are compared using different TOF times. It is known that for long TOF the common TOF technique is reliable [18, 109] and from figure 4.10 and table 4.1 is known that our method gives good result for all TOF times. Moreover it is expected that the common TOF technique breaks down at short TOF times, since the cloud size is underestimated by the 1D Gaussian fit which results in inaccurate temperature calculation.

The comparison of the methods is performed by taking a group of different TOF times with their respective cloud size σ_t and σ_G and calculating with them the temperature by the two methods (fig. 4.13). To calculate the temperature with the common TOF technique is needed at least data from two different TOF times, but we have chosen three or more TOF times in order to get more reliable results. Out of the set of six different TOF times (3-20ms) the possible combinations with three or more TOF times is shown in table 4.2. Each group of TOF times is referred to by the average TOF time of the components which is shown at the bottom row of table 4.2.

TOF [ms]	1^{st} point [ms]	2^{nd} [ms]	3^{rd} [ms]	4^{th} [ms]	5^{th} [ms]	6^{th} [ms]	7^{th} [ms]	8^{th} [ms]	9^{th} [ms]	10^{th} [ms]
3	3	3	-	3	-	3	-	-	-	-
5	5	5	5	5	5	5	-	5	-	-
7	7	7	7	7	7	7	7	7	7	-
10	-	10	10	10	10	10	10	10	10	10
15	-	-	-	15	15	15	15	15	15	15
20	-	-	-	-	-	20	-	20	20	20
avg.	**5.00**	**6.25**	**7.33**	**8.00**	**9.25**	**10.00**	**10.67**	**11.40**	**13.00**	**15.00**

Table 4.2: *TOF groups used for the comparison of the methods for the temperature calculation.* In this table the groups of TOF times used to calculate the temperatures with both methods are shown. Each TOF group is referred to by the average TOF which are presented in the bottom row. The groups are organised in an ascending order with respect to the average TOF. Each data point in figure 4.13 correspond to one group of TOF times of this table.

In order to calculate the temperature with the common TOF technique one group of TOF times is used from table 4.2 and the corresponding cloud size σ_G calculated by the 1D Gaussian fit as previously shown fig. 4.9. The same group of TOF times is then used to calculate the temperature with formula (4.38) followed by averaging the corresponding temperatures from of all TOF time taken into account. The results of the temperature calculations are presented in fig. 4.13.

In general, for all magnetic gradients the temperature calculated with our method stays linear for all data sets and the average temperature is the same as in table 4.1 with a dispersion of the data point from 1 to 7μK. On the other hand, the common TOF technique seems to reach a stable temperature for long TOF times[12] as expected, but for short TOF times it yields higher temperatures. The average temperature in the stable part has similar values than the temperature calculates in the previous section (table 4.1). The deviation in temperature form the shortest TOF time average (5.00ms) to the average temperature goes from 23% in the best case for 20G/cm to 39% in the worst case for 50G/cm.

[12]For 50G/cm magnetic gradient the temperature with the common TOF technique does not stabilise completely.

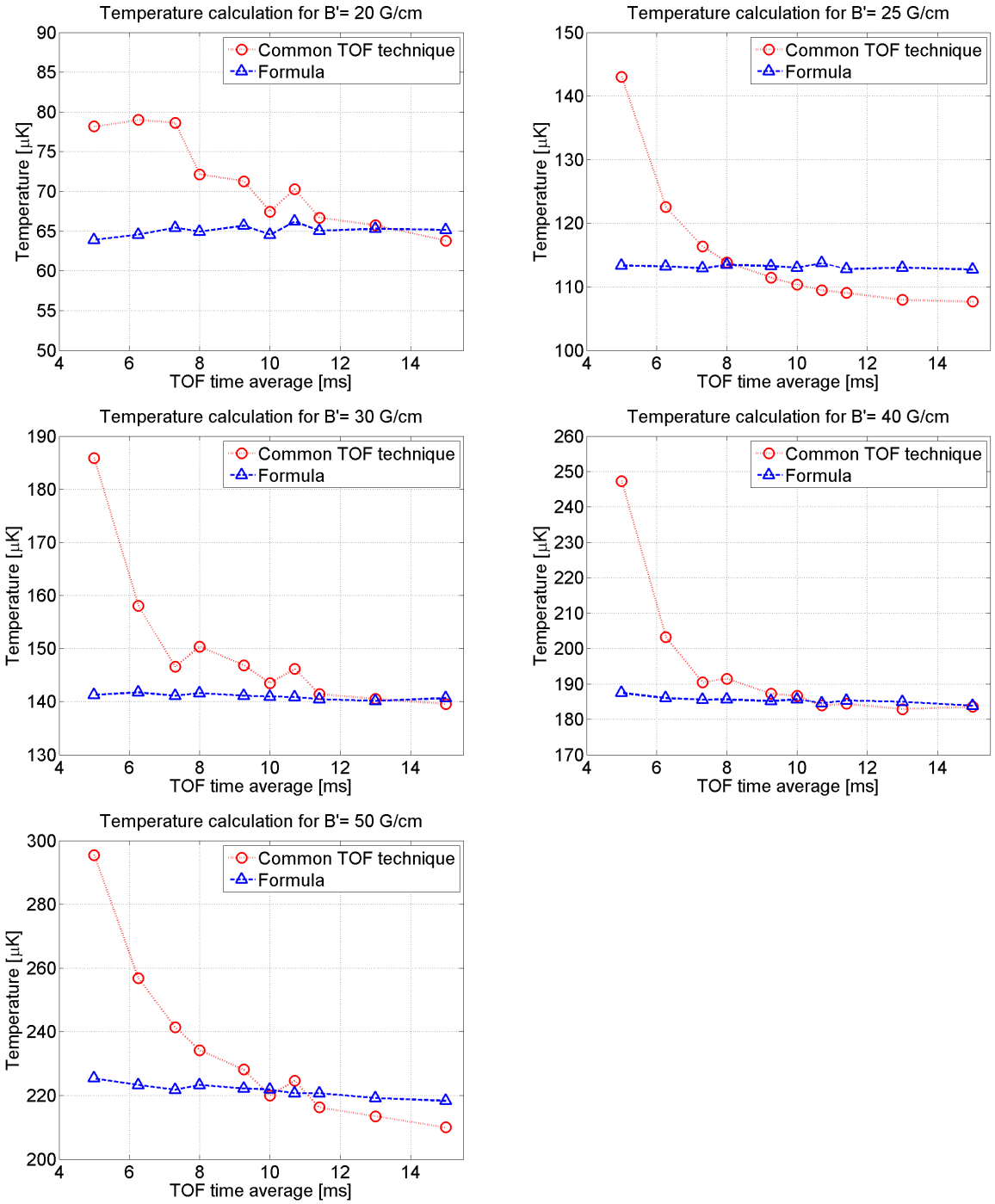

Figure 4.13: *Comparison of methods for temperature calculation.* These plots show the temperature calculated with both method for the different magnetic gradients. Each temperature calculated by the common TOF technique is produces using a TOF group from table 4.2 and the corresponding cloud size σ_G calculated with the 1D Gaussian fit (fig. 4.9). The same group of TOF time is used for our method but the temperature is calculated as the average of the corresponding temperatures for all TOF times taken into account.

Also we observe that our method overestimates the temperature for 25 and $50G/cm$ in comparison with the common TOF technique. Considering that the cloud size σ_t for $25G/cm$ is higher in comparison with the Gaussian calculation σ_G it is expected that the calculated temperature is higher. The percentage difference is 5%, and is the same that the one calculated in the previous section. On the other hand for $50G/cm$ the cloud sizes are similar but the percentage difference between the two average temperatures is just 4% which can be attributed to error in size calculation of any of the methods.

From the comparison we can conclude that: our method accurately calculates the temperature for all given TOF time; the common TOF time gives accurate temperatures up to 8% or better for TOF time average from 8ms or longer.

4.6 Conclusions

By combining the advantages of these two methods a more robust method of temperature calculation can be produced. The main advantage of our formula is that accurately calculates the temperature from a single shot at any TOF time. The main advantage of the common TOF technique is to fit a function to the data, becoming in this way less sensitive to small fluctuations or problems with background subtractions. The combination of cloud size determination with a Gaussian fit and temperature calculation with formula (eq. 4.38) can be used for high magnetic gradients and long TOF times. But at short TOF times our method of cloud size calculation (sect. 4.4) is more reliable. In general, it is easier and faster to calculate the temperature with formula (eq. 4.38) because it requires just a single TOF time and the respective cloud size σ_t, making it a good candidate for programs like the camera control where just a single TOF time is recorded each time. Our methods is even reliable for short TOF time with a percentage difference to the long TOF time of just 6%.

A drawback of our method is the sensitivity to systematic errors such as wrong magnetic gradient, Eddy currents while switching off the coils or wrong magnification. The two last errors are also in the common TOF technique. As mentioned before, the magnetic gradient can be accurately calculated by measuring the levitation current. The Eddy currents can be avoided by cutting a slot

to the housing of the coils, which is the case for the moving coils but no for the Feshbach coils[13]. To measure the magnification, the dropping of the centre of the cloud in free fall was analysed as a function of TOF time. This method should be one of the most reliable since it uses the atoms as a reference. Nonetheless this method can also give inaccurate result if the cloud has been influenced by other forces making it not to drop freely, such as Eddy currents or residual magnetic fields.

Further work is to calculate the temperature as a function of the other two standard deviations (σ_y, σ_x) which is useful for detection performed along a different axis. As well knowledge of the cloud size along the other axis is advantageous for analysis of cloud transferred through small apertures, or for study of atom losses due to proximity with surfaces [110, 111].

In summary this chapter presents: a study of the phase-space distribution of the atoms cloud in a magnetic quadrupole trap (sect. 4.2), we developed an accurate method of temperature calculation from a single shot (sect. 4.3) which can be used at any TOF time. This methods performs much better than the common TOF technique for short TOF times and gives similar values at long TOF times (fig. 4.13). Also we developed a method to calculate the cloud size σ_t at short TOF time when the Gaussian fits are not reliable (sect. 4.4).

[13]The Feshbach coils are the ones used to produce the magnetic quadrupole trap for the experimental data used in this chapter.

CHAPTER 5

EXPERIMENTAL TECHNIQUES TOWARDS BEC

Rather than talk about the optimisation of the system that has already been presented in [35], in this chapter a discussion of the atom losses and heating will be presented. In order to understand the capabilities of the experiment, a description of the experimental setup (chap. 2) was introduced. In order to describe the losses and heating of the atom cloud, the stages of the experimental sequence towards the BEC are described. Each stage will be presented in detail with experimental parameters and the resulting number of atoms N, temperature T, phase-space density PSD, and transfer efficiency. Once the experimental conditions have been established, the analysis of the losses will be performed, followed by the description of the heating processes along the experimental sequence.

The importance of looking at the atom loses is to understand the losses mechanisms and try to minimise them. Besides heating processes want to be avoided.

This chapter is organized as follows: starting with a brief description of the experimental sequence, continuing with atom loading of the 2D-3D MOT, followed by magnetic trapping and transport, then evaporative cooling in the magnetic and dipole trap is shown. At the end of the chapter the expansion of the BEC is described qualitatively and some preliminary result of the first 2D soliton are shown.

5.1 Experimental sequence outline

In order to obtain a Bose-Einstein condensate (BEC), the phase space density (PSD) has to increase from $\sim 10^{-19}$ at atom vapour to $\sim$2.6 at the dipole trap. To achieve this increase in PSD various

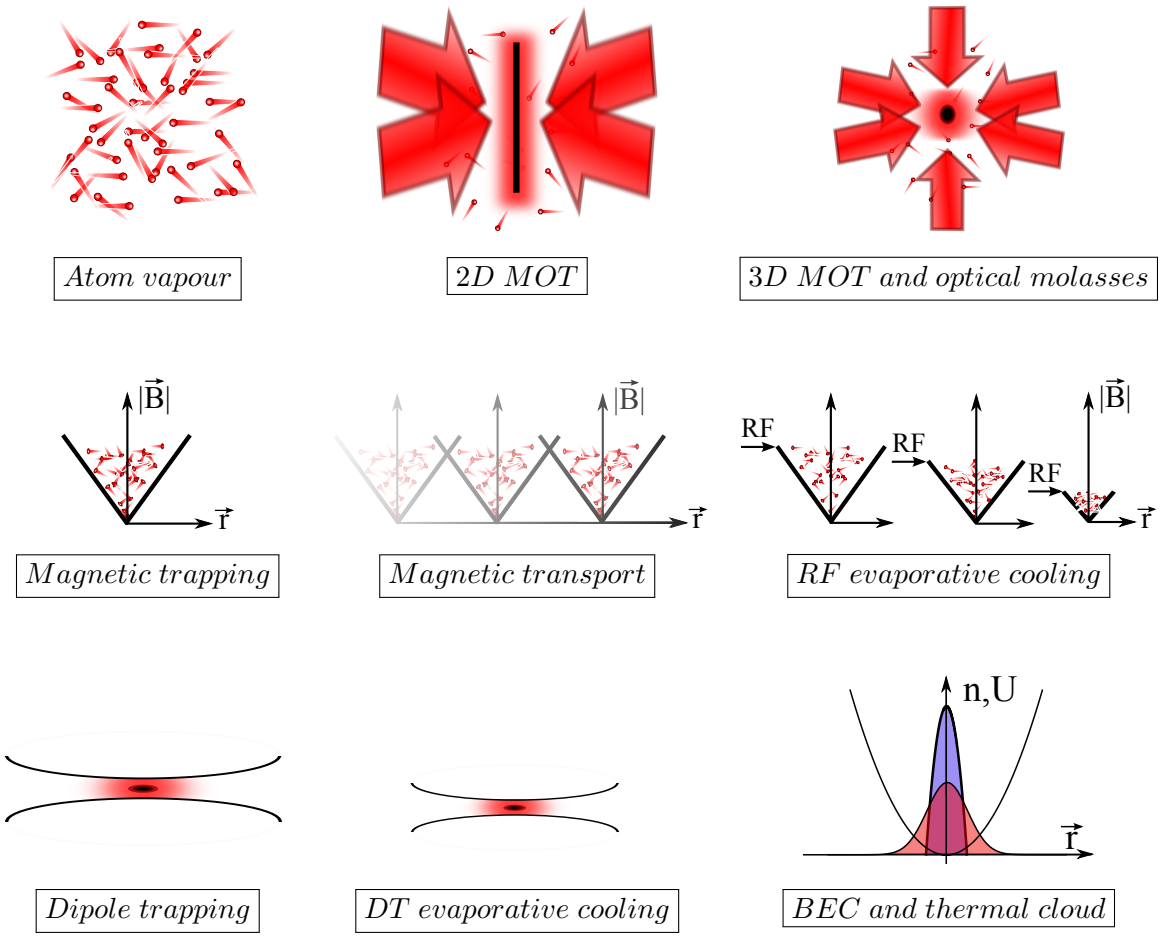

Figure 5.1: *Experimental sequence for BEC.* At the top row of this figure is shown the laser cooling processes, starting from a hot atom vapour, which is captured and cooled in two dimensions by the 2D magneto-optical trap. Afterwards the atoms are transferred to the 3D MOT chamber by a pushing beam and are recaptured by the 3D MOT where further cooled by optical molasses is performed. The middle row shows the magnetic confinement of the atom cloud used to transport the atoms from the 3D MOT chamber to the science chamber where induced RF evaporative cooling is performed. The bottom row shows the transfer from the magnetic quadrupole trap to the astigmatic dipole trap. Further evaporative cooling is performed at the dipole trap by lowering the intensity of the beam until BEC is reached.

experimental techniques to cool, control and confine the atoms are used. The description of the techniques is oriented in the order they are used. Starting with a hot atom vapour and finishing with a BEC in the dipole trap, as can be seen in fig. 5.1.

The atoms are first released in the vacuum system by rubidium dispensers and are captured

and cooled in two dimension by the 2D MOT. Then they are transfered to the 3D MOT chamber using a pushing beam. In the 3D MOT chamber the atoms are cooled further ($\sim 60\mu K$) by optical molasses. Once the atoms are cooled enough to be captured in a magnetic quadrupole trap, they are transported to the science chamber. Here induced radio frequency (RF) evaporative cooling is performed in the magnetic trap followed by the loading of the atoms into the dipole trap (DT). Another series of evaporative cooling is done in the dipole trap until the BEC is achieved (see fig. 5.1). A detail description of the various experiment stages is given in the following sections.

5.2 2D-3D magneto-optical trap

Magneto-optical traps are powerful tools to reduce the temperature of a sample and also provide trapping. The first 3D MOT was realised by Raab *et al.* [112] in 1987 where they show that their MOT had a trap depth of ≈ 0.4K, ten times higher than any magnetic trap reported before [86], while also achieving cloud temperatures of less than a mK. The atom number limit at the MOT is given by the equilibrium between capture and losses. The capturing of atoms is determined by the loading rate from the 2D MOT and the losses by the background collisions[1] and trap depth. On the other hand the theoretical temperature limit of laser cooled atom cloud is given by the Doppler temperature $T_D = \hbar\Gamma/(2k_B)$, with Γ the natural line width of the transition used. For the ^{87}Rb D2 line this yields a temperature of $T_D = 145\mu$K [63].

In our experiment, the 2D MOT is the first stage in the production of a degenerated ultra cold cloud. In here the ^{87}Rb atoms are captured from background gas[2] and cooled in two directions. The 2D MOT provides a beam of cold atoms [113] that is recaptured by the 3D MOT [112]. The atom transfer between the two MOT chambers is enhanced by a factor of ten by the pushing beam, which is placed above the 2D MOT and is aligned with both the 2D MOT and the 3D MOT. The MOTs are the only stages of the experiment were atoms are loaded, therefore the MOTs are optimised for maximum number of atoms, leaving the optimisation of the PSD for the following stages where the transfer efficiency and the temperature can be improved. The 2D-3D MOT setup is the one that

[1] At this low density regime, two body inelastic collisions and three body recombination can be neglected.
[2] An atom vapour of Rb atoms is released into the vacuum system using hot vapour dispensers.

dictates the starting point in atom number and temperature, and therefore dictates the initial PSD.

The 3D MOT has a final atom number of 2×10^9 atoms after 20s of loading time. Since the full loading of the MOT is long[3] the optimisation and analysis of the transfers have been done with shorter loading times and therefore a lower atom number. Nevertheless is expected that the losses and heating of a bigger cloud behaves in a similar way keeping the same percentage of atom losses and heating. The study of the atom losses and heating is performed from the previous experimental stage. And at the start corresponds to the atoms number at the 3D MOT and the optimize temperature of molasses (shown in next section).

5.2.1 Optical molasses

In order to reduce the temperature and consequently improve the PSD optical molasses is performed. The first observation of optical molasses was done by Chu *et al.* [100] in 1985, where they have studied the viscous damping force produced by three pairs of counter-propagating beams, reporting confining time of 0.1s and achieving temperatures close to the Doppler limit for sodium (240μK). Later experiments [99,114] and theory [115–117] showed that the limit of molasses was lower that the Doppler limit before suggested in [100]. A review of optical molasses [116] introduced two theoretical description of optical molasses: a *classic molasses* and a *polarisation gradient cooling*. The classical molasses considers the velocity dependence of Doppler cooling, but completely neglects interference between the counter-propagating beams and any coherent interaction of the atoms with the light that involves cycles of absorption and stimulated emissions. Using this theoretical description, the temperature limit of the classical molasses is equal to [116]:

$$k_B T_{mol} = \frac{\hbar\Gamma}{4} \frac{1 + I/I_{Sat} + (2\Delta/\Gamma)^2}{1 + 2|\Delta|/\Gamma}, \tag{5.1}$$

and can not reach lower temperatures than the Doppler limit T_D. On the contrary the polarisation gradient cooling gives a temperature of [115]:

$$k_B T_{pol} = \frac{\hbar\Gamma I/I_{Sat}}{2|\Delta|/\Gamma} \left(\frac{29}{300} + \frac{254}{75} \frac{1}{(2\Delta/\Gamma)^2} \right). \tag{5.2}$$

[3]The loading of the MOT takes half of the time needed for a full sequence (∼40s).

This temperature limit T_{pol} is directly proportional to the intensity I and inversely proportional to the detuning Δ, thus by reducing the intensity and increasing the detuning a lower temperatures can be reached. However the polarisation gradient cooling has critical velocity v_c above which the damping force decreases. Therefore v_c represents a capturing range for the polarisation gradient force. In order to have a linear damping force, and consequently effective polarisation gradient cooling, the atom rms velocity should be much larger than the recoil velocity [115] $mv_{rms} \gg \hbar k$, with m the atom mass, $k = 2\pi/\lambda$ the wave vector of the light and λ the wavelength of the light.

Experimentally, optical molasses is carried out after turning off the magneto-optical trap and switching back on the cooling light. Additionally, compensation coils have been used to cancel out any stray magnetic field that could shift the cloud position. The lowest temperature of 56μK is achieve at a detuning of $\Delta = 9.2\Gamma$ and total intensity in the six beams of $I = 10.5\text{mW/cm}^2$. These experimental parameters yield temperatures in classical molasses of $T_{mol} = 1.4$mK and in polarisation gradient cooling of $T_{pol} \sim 10\mu$K. The temperature reached with optical molasses is still higher than the one predicted by polarisation gradient by a factor of 5.6 although we have reached temperature below the Doppler limit by a factor of 2.6. By optimising the temperature at the optical molasses, the PSD has also been increased to $\sim 10^{-10}$.

5.3 Magnetic trapping and transport

After laser cooling the phase-space density still needs to be increased. Evaporative cooling is the second cooling stage. In order to perform RF evaporative cooling the atoms need to be transport to a chamber with better vacuum thereby longer lifetime of the cloud in the magnetic trap. The atom cloud is magnetically trapped in the transport coils and transported from the 3D MOT chamber to the science chamber. The loading of the magnetic trap and process to reduce heating is presented in the next sections.

5.3.1 Optical pumping

In order to improve the loading of the magnetic trap, the atoms are prepared in a low-field seeker state ($F = 2$, $m_F = 2$, $g_F = 1/2$). The preparation is done by applying a bias field to split

the hyperfine levels and a pulse of σ^+-polarised resonant light for 1.99ms that has an intensity of $130\mu\text{W/cm}^2$. This process is called optical pumping. The application of optical pumping increases 3.5 times the number of magnetically trap atoms (2×10^8 atoms) in comparison to a none optically pumped sample (0.57×10^8 atoms). This increase is higher than expected, since the distribution of the hyperfine levels m_F is homogeneous, in the $F = 2$ state there are two of five hyperfine states that can be captured $m_F = 1, 2$. The other three hyperfine states $m_F = 0, -1, -2$ are not captured or expelled (high field seekers) from the trap. Meaning just 40% of the atoms can be trapped. Therefore an increase of 2.5 times was expected. Further studies to fully understand the increase on atom number by optical pumping is needed.

Heating by optical pumping

Optical pumping also heat the atom cloud at a rate R_{heat}. This heating is due to the moment transfer of each absorbed photon. Therefore a short pulse is applied. Experimentally the temperature of the magnetically trapped atoms goes from 490μK to 590μK when optical pumping is performed, which correspond to an increase on temperature of 100μK (20%). The heating rate R_{heat} can be expressed as the product of the recoil limit temperature $T_R = h^2/(m\lambda^2 k_B)$ [115] and the scattering rate R_{sc} (eq. 3.8) as

$$R_{heat} = T_R \, R_{sc}. \tag{5.3}$$

Replacing the experimental values mentioned in the previous paragraph the heating rate is calculated to be $R_{heat} = 50\text{mK/s}$, with a pulse of 1.99ms the total heating is equal to 100μK which is in perfect agreement with the experiment.

Bias field to reduce heating

In order to reduce the atom losses the magnetic gradient is switched quickly, this fast switching accelerate the atom cloud above the trap center, thereby half of the atom cloud is heat up. One way to avoid this heating process is by shifting the magnetic trap center above the cloud, followed by adiabatically ramping up the magnetic field [35]. By applying the bias field without optical pumping the atoms cloud at the magnetic trap is 90μK colder. But if optical pumping and bias

field are applied the final temperature is 40μK hotter. The specific temperatures and number of atoms can be fount in table 5.1.

After magnetic trapping with optical pumping and offset magnetic field the cloud is composed of 2.1×10^8 atoms at a temperature of 630μK.

5.3.2 Magnetic transport

Once the atoms are captured in the transport coils they are transferred to the science chamber by mechanically moving the transport coils using a rail. The transport takes 0.9s. While being transported the atom cloud has to pass through a differential pumping stage with inner diameter of 16mm and the opening of the science chamber with 10mm diameter. These two opening dictate the cloud size that can pass through without it being cut. From the previous chapter it is known that the cloud size inside of a magnetic trap is given by the temperature of the cloud and the magnetic gradient (eq. 4.30). Even when this size is along the x axis a similar or bigger size is expected along the y axis due to the effect of the gravitational field, and half of the size along the z axis due to the magnetic gradient being twice as strong.

Experimentally, the atom cloud is transported in a magnetic trap with a gradient $B'_\rho = 66$G/cm, with temperature of 630μK or lower. This experimental conditions give an cloud size of $\sigma_{0,x} =$ 2.9mm. If gravity is not considered the cloud size along the y axis is equal to the cloud size along the x axis and the smallest aperture (10mm) will let pass $1.7\sigma_{0,x}$ which is equivalent to $\sim 90.6\%$ of the cloud (see appendix D). If gravity is included the cloud centre is pull downwards according to eq. 4.12b, and with the previous mentioned experimental conditions the shift $\langle y \rangle$ corresponds to 0.9mm. This shift reduces the area where the atom cloud can pass without touching the vacuum walls, thereby just $\sim$ 87.5% will pass through. The atoms that are lost by collision with the vacuum wall correspond to the most outer layer of the cloud and therefore the hottest atoms. Thus effectively this atoms losses produces evaporative cooling similar to [111]. The measure transfer efficiency is 95% this suggest that the initial cloud temperature is lower than 630μK. To reproduce this efficiency with the given magnetic gradient of 66G/cm the temperature of the cloud should be 460μK. This cloud temperature is feasible since the temperature of the cloud in the quadrupole

could were overestimated by assuming a point source as a initial size.

The cloud size depends linearly with temperature thus by reducing the temperature of the cloud more atoms will pass and be transferred to the science chamber without getting lost on the vacuum walls. Another way to improve the transport efficiency is by increasing the magnetic gradient which also reduces the atoms cloud size and therefore losses for collisions with the vacuum walls are avoided.

5.3.3 Transfer to Feshbach coils

Once the atoms are in the science chamber they are transferred to the Feshbach coils. This transfer is needed to free the transport coils and send them back to the position of the MOT chamber.

Experimentally the transfer is performed by simultaneously lowering the magnetic gradient of the transport coil and increasing the magnetic gradient of the Feshbach coil. The magnetic gradient B'_ρ are ramped from 66G/cm to 0 for the transport coils and from 0 to 58.5G/cm for the Feshbach coils[4] in 3s. The experimental result of this transfer are an initial condition at the transport coils of $N = 2.9 \times 10^8$ atoms at a temperature of $T = 420\mu$K. At the Feshbach coils we have $N = 2.5 \times 10^8$ atoms a temperature of $T = 340\mu$K.

First method of temperature reduction. The transfer process can be seen as adiabatic process where the magnetic gradient is lower it from 66G/cm to 58.5G/cm in 3s. If this is the case the number of atoms should be conserved as well as the PSD in which case the final temperature T_f is related to the initial temperature T_i with equation (4.45). This formula predicts a final temperature T_f of 385μKm which is 13% higher than the experimental result. Thus other mechanisms have to be contributing to the temperature reduction.

First cause of atom losses. Due to the fact that the transfer takes 3s, losses by background collisions have to be considered. Taking into account that the number of atoms in a magnetic trap decays as [74]:

$$N(t) = N(0)\exp(-t/\tau) \tag{5.4}$$

where $\tau = 52s$ is the magnetic life time [35]. After holding the atom cloud for 3s it is expected

[4]Higher magnetic gradient B'_ρ with the Feshbach coils were not used to avoid thermal stress in the power connectors, that could lead into a oil leak.

to lose 6% of the atoms which is lower than the one measured of 14%. Therefore some other loss mechanism is also taking place.

Other atom losses and cooling process. The perfect candidate to produce atom losses as well as cooling the atoms is evaporative cooling. If we assume that the missing 8% extra of atoms is due to evaporative cooling, the reduction in temperature is given by [19]:

$$\frac{T_f}{T_i} = \left(\frac{N_f}{N_i}\right)^{\gamma}, \tag{5.5}$$

with $\gamma = 1.048$ which has been calculated numerically and is a parameter that depends on the trap depth and temperature of the cloud. Replacing $N_f/N_i = 0.92$ (8% losses) we obtain a change of temperature $T_f/T_i = 0.916$. Thus the final temperature is 8.4% lower which is equivalent to a decrease of 35μK. Combining the two reduction of temperature a final temperature of $T_f = 350\mu$K is obtain which is in closed agreement with the temperature experimentally measured of $T = 340\mu$K.

5.4 Forced evaporative cooling

Evaporation as a technique to cool atoms was fist suggested by Hess in 1986 [15], where he explained how the removal of the hottest atoms can lead to a lower equilibrium temperature. This technique was first demonstrated for hydrogen [16] and adapted to alkali atom later on [17,18,23]. Evaporative cooling led to the realization of BEC soon after [1–3]. The technical limitation of evaporative cooling is that the thermalisation process should be shorter than the lifetime of the sample. The lifetime is determine by loss and heating process of the trapped atoms [20]. Combination of evaporation in magnetic trap and dipole trap similar to the one realised in this experiment have been done before [28, 29].

5.4.1 RF Evaporative cooling in the Feshbach coils

Induce RF evaporative cooling is one type of evaporative cooling and was fist suggested by Pritchard *et al.* [118]. In this scheme atoms are removed from the trap by inducing a RF transition to an untapped state [17] while still keeping a tight magnetic confinement. This technique is the one used

for the first BEC [2]

In our experiment, once the atom are captured in the Feshbach coils RF evaporative cooling is performed. The direct digital synthesis (DDS[5]) produces an RF signal that is delivered to the experiment by an antenna placed near to the science chamber. The RF signal is ramp from 40MHz to 10MHz in 5s, and in a second ramp from 10MHz to 2MHz in 4s keeping the same magnetic gradient $B'_\rho = 58.5$G/cm. In this ramps atoms are reduced to 5.5×10^7 and 5.5×10^6 and the temperature to 210μK and 25μK.

5.4.2 Transfer to the dipole trap

In order to reduce Majorana losses [24], the astigmatic dipole trap has been placed below the magnetic quadrupole trap centre and turned on at its maximum power (3.5W) during RF evaporation. Thus atoms that had escaped from the zero of the magnetic trap are recapture by the dipole trap. After induce RF evaporation the atoms are cool enough to be confined in the dipole trap without a big amount of losses. The transfer to the dipole trap is performed by lowering the magnetic gradient from $B'_\rho = 58.5$G/cm to slightly less the levitation gradient $B'_\rho = 14$G/cm in 1s. Only 1.7×10^6 atoms are transferred at a temperature of 13μK. The transferred efficiency of just 30% and can be seen as an additional evaporative process where the hottest atoms are not captured in the dipole trap.

5.4.3 Evaporative cooling at the dipole trap

Evaporative cooling by lowering the power of the dipole trap is another type of evaporation and was first demonstrated by Adams *et al.* in 1995 [18]. By reducing the power of the laser beam the trap depth and the trapping frequencies are also reduced. The reduction of the trap depth is beneficial for evaporation since the hottest atoms can leave the trap. In contras the reduction of the trapping frequencies is not as favourable because the confinement strength is reduced and therefore the density. Despite this reduction in density, BEC can be reached with just optical techniques [30].

Evaporation in the dipole trap is preformed by reducing the intensity of the 1550nm laser beam

[5]FlexDDS is a multichannel phase-coherent RF source.

in two ramps the first one from 100% to 30% in 3s followed by another ramp from 30% to 8% in 3s and holing the atoms for 0.25s to let it rethermalised. After these two ramps and rethermalisation BEC is reached with $N_c = 3.5 \times 10^4$atoms at a temperature of 100nK, with a surrounding thermal cloud of $N_{th} = 2.2 \times 10^4$. The final trapping frequencies are $(\omega_x, \omega_y, \omega_x) = 2\pi \times (54, 876, 25)$Hz and a trapping depth of 9.6μK

A resume of the atoms number, temperature, phase space density and transfer efficiencies is presented in table 5.1

Experiment stage	Atom number	Temp [μK]	PSD	% transfer
3D MOT	4.85×10^8	~ 200	-	100
Molasses	1.75×10^8	60	$\sim 10^{-10}$	36
Magnetic trapping	0.57×10^8	590	-	-
MT + optical pumping	2×10^8	690	-	-
MT + magnetic offset	0.63×10^8	500	-	-
MT + OP + magnetic offset	2.1×10^8	630	-	29
Transport to science chamber	2.9×10^8	420	-	95
Transfer to Fesh coils	2.5×10^8	340	-	86
RF evaporation ramp 1	5.5×10^7	210	$\sim 10^{-6}$	-
ramp 2	5.5×10^6	25	-	-
Transfer to dipole trap	1.7×10^6	13	7.2×10^{-6}	26
Evaporation @ DT	8.5×10^5	4.5	5.4×10^{-4}	-
BEC	3.5×10^4	0.1	> 2.612	-
Thermal cloud	2.2×10^4	0.1	-	-

Table 5.1: *Resume of experimental results at different stages of the BEC sequence.* It is important to notice that the discrepancy in atom numbers is due to the various loading time at different stages of the sequence optimisation. The transferred efficiencies are in proportion with the previous optimised stage. For the magnetic trapping the efficiency is with respect to the MOT not with molasses.

5.5 Expansion of the BEC

A defining characteristic of a BEC is its anisotropic expansion, the axis with more confinement is accelerated due to the repulsive force (interaction energy become kinetic energy). Description of this anisotropic expansion has been studied for cigar and disk BEC [90]. In this geometries, the BEC has a cylindrical symmetric characterised by the radial frequency $\omega_\rho = \omega_x = \omega_y$ and the asymmetry parameter $\lambda = \omega_z/\omega_\rho$. For the cigar shape the asymmetry parameter $\lambda \ll 1$ and for the disk shape $\lambda \gg 1$. Our BEC can be considered as a disk even when the frequencies along x and y are not the same, in this case the anisotropic acceleration will be along the z axis, that for our case refers to the vertical direction as can be seen in fig. 5.2. Something interesting to investigate is how much the difference on ω_x and ω_y affects the anisotropic expansion along the z axis, and if the expansion along x and y are the same or at least similar.

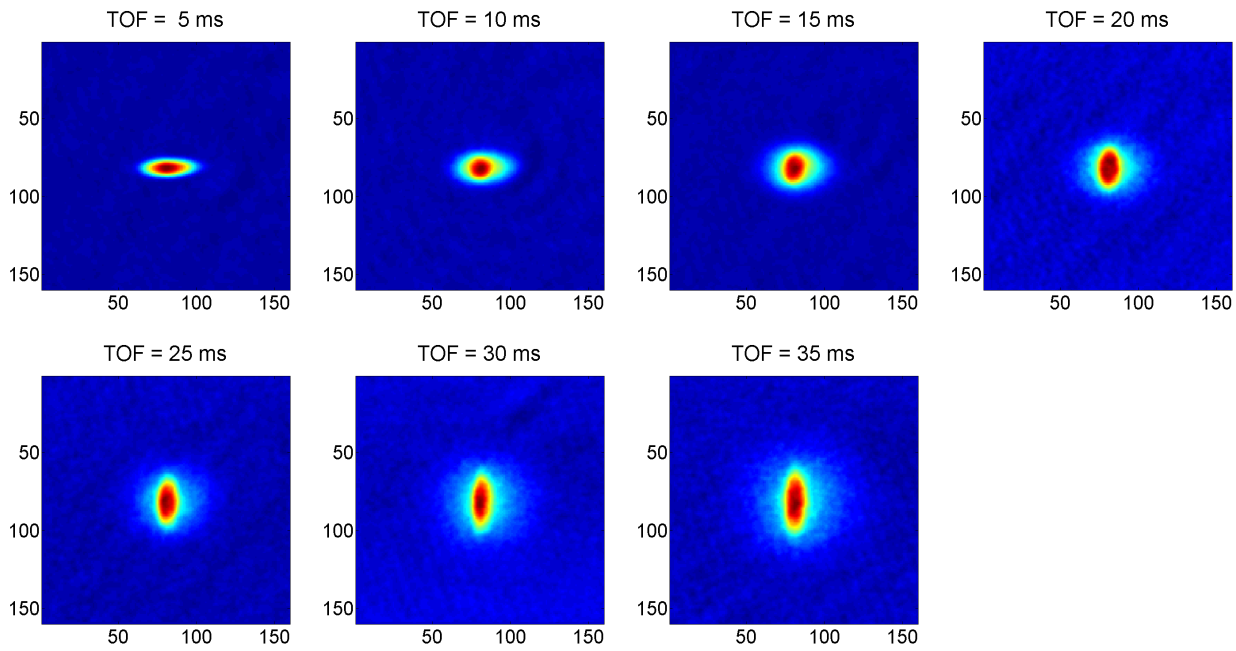

Figure 5.2: *BEC expansion.* The quasi 2D (disk) BEC is presented for different TOF times. The anisotropy on the expansion along the vertical and horizontal axis can be observed and is a crucial feature of the Bose-Einstein condensates.

5.6 Solitons!?

Preliminary results of what could be the first soliton in a quasi-2D Bose-Einstein Condensate have been observed (fig. 5.3). For more information refer to [36]. The "soliton" was generated using the phase-imprinting method [38] where half of the BEC is shone with near resonant light. The observation of the BEC has been done with the high resolution optical system (sect. 3.5.2).

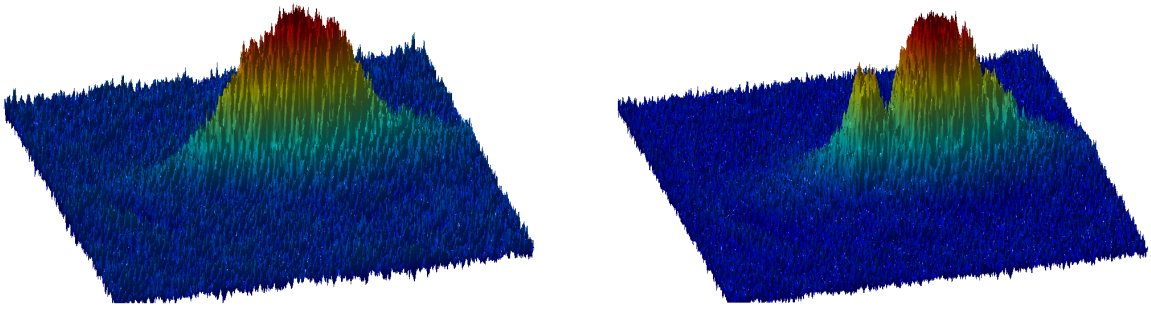

Figure 5.3: *Preliminary result of solitons.* In the left figure an undisturbed BEC is shown. In the right figure a dip on the BEC has been created by phase imprinting.

.

CHAPTER 6

CONCLUSIONS

In the context of this thesis the project has achieved the production of a robust and stable system, that is capable of producing ^{87}Rb BEC with a 100% rate.

The detection system for absorption imaging was designed, built and used to measure and characterise the atom cloud at the different stages of the experimental sequence. Observation of the BEC with the high resolution imaging system (vertical detection) has been achieved and further characterisation is in progress. A camera control for in-situ absorption image processing was developed. Calculation of atom number and temperature were implemented in this camera program as well as the defringing algorithm. Further improvements of the camera control are the implementation of temperature calculation for quadrupole traps and fitting of partly condensed clouds to calculate condensate fraction.

A new method to calculate the temperature of an atom cloud held in a quadrupole trap was developed. In the process the phase-space density of the atom cloud in the quadrupole trap was studied. This new method performed much better in the sort TOF time regime than the common TOF technique. Another advantage of this method is its accuracy in calculating the temperature for any TOF time, besides calculating the temperature from a single TOF time.

The various stages toward the BEC were analysed for atom losses and heating. Further studies to understand the increase in atom number due to optical pumping is needed. The expansion of the BEC was shown. Studies to characterise the anisotropic expansion can be done.

.

APPENDIX A

ATOM LIGHT INTERACTION

The main objective of this section is to introduce the semiclassical theory for atom and light interaction. The following derivation and calculation are based on [119].

The following derivations use a semiclassical approach based on two underlying fundamental assumptions. The first assumption is that the centre of mass of the atom is described by a small wavepacket, in quantitative terms $\Delta x << \lambda$ where Δx is the uncertainty on position of the atom and λ is the light wavelength. This ensure that the electric field is well defined over the atomic wavepacket. The second assumption is that the speed of the atom should be well defined so that the uncertainty in the atomic Doppler shift should be less than the atomic transition linewidth. Quantitatively, this is $k\Delta v << \Gamma$, where k s the light wavenumber, Δv is the uncertainty in atomic velocity and Γ is the natural linewidth of the atomic transition.

These two restriction may be combined with further condition, namely Heisenberg's uncertainty principle $m\Delta x\Delta v \geq \hbar/2$, to give the requirement $E_R \ll h\Gamma$, where E_R is the recoil energy given by $E_R = \hbar^2 k^2/2m$. E_R is the change in kinetic energy of an atom caused by the absorption of one photon, and m is the mass of the atom. This condition is well satisfied for most usable transitions e.g. $h\Gamma/E_R = 10,000$ for ^{87}Rb atoms in the D_2 transition, which is the one used in this thesis.

A.1 Atomic density matrix and Bloch vector

Consider a stationary atoms as a closed system with non-degenerate ground and excited levels $|g\rangle$ and $|e\rangle$ coupled by a electric dipole transition as described in figure A.1. The two states have

amplitudes $a(t)e^{-i\omega_g t}$ and $b(t)e^{-i\omega_e t}$ and energies $\hbar\omega_g$ and $\hbar\omega_e$ respectively. The transition from ground to excited state is characterise with the transition frequency $\omega_0 = \omega_e - \omega_g$.

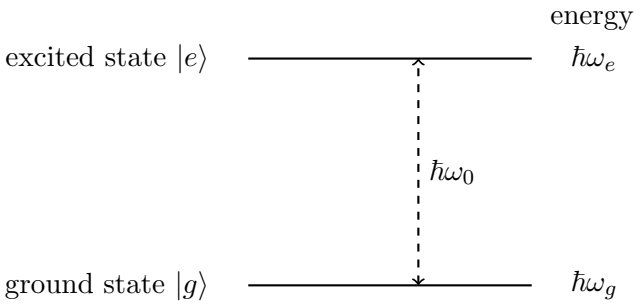

Figure A.1: Two level atoms scheme, and symbols used to described it.

The quantum state of the atom can be described in time t by

$$|\Psi\rangle = a(t)e^{-i\omega_g t}\,|g\rangle + b(t)e^{-i\omega_e t}\,|e\rangle\,, \tag{A.1}$$

which is interacting with a light field described by

$$\vec{E} = \frac{1}{2}\vec{\epsilon}(\vec{r})E_0(\vec{r})e^{-i\omega_L t} + c.c. \tag{A.2}$$

where $\vec{\epsilon}(\vec{r})$ is the polarisation unit vector at the position $\vec{r}$ of the atomic centre of mass, $E_0(\vec{r})$ the field amplitude and ω_L the light field angular frequency. From hereon the dependency on the position ($\vec{r}$) will be omitted except where a need of clarity dictates otherwise.

In order to describe the system as a function of time we have to solve the Schrödinger equation for the interaction

$$\left(H_{atom} - \vec{E}\cdot\vec{d}\right)|\Psi\rangle = i\hbar\frac{d}{dt}\,|\Psi\rangle\,, \tag{A.3}$$

where $\vec{d}$ is the atomic dipole operator. By substituting equation (A.1) into equation (A.3) and solving the couple equation the coefficients $a(t)$ and $b(t)$ are determined and equal to

$$a = \left(\exp\frac{i\Delta t}{2}\right)\left(\cos\frac{\Omega t}{2} - \frac{i\Delta}{\Omega}\sin\frac{\Omega t}{2}\right), \tag{A.4}$$

$$b = \left(\exp\frac{i\Delta t}{2}\right)\frac{i\Omega_0 e^{i\theta}}{\Omega}\sin\frac{\Omega t}{2}, \tag{A.5}$$

where $\Delta = \omega_L - \omega_0$ is the detuning of the laser, $\Omega_0 e^{i\theta} = \frac{E_0 \langle e|\vec{E}\cdot\vec{d}|g\rangle}{\hbar}$ is the complex Rabi frequency expressed in exponential form (Ω_0 and θ are both real) and $\Omega = \sqrt{\Omega_0^2 - \Delta^2}$ is the generalised Rabi frequency.

The atomic density matrix is an operator defined as

$$\rho = |t\rangle \langle t| = \begin{bmatrix} a^* a & b^* a e^{i\omega_0 t} \\ a^* b e^{-i\omega_0 t} & b^* b \end{bmatrix}. \tag{A.6}$$

The density matrix equation of motion without relaxation term[1] is

$$\frac{d\rho}{dt} = \frac{i}{\hbar} [H, \rho], \tag{A.7}$$

where H is the Hamiltonian matrix and consist of two parts $H_{atoms}+H_{dipole}$ which the first represents the internal energy of the atoms an the second one the atom-field interaction energy. In the rotating wave approximation H is then given by

$$H = \hbar \begin{bmatrix} \omega_g & -\frac{1}{2}\Omega_0 e^{-i\theta} e^{i\omega_L t} \\ -\frac{1}{2}\Omega_0 e^{i\theta} e^{-i\omega_L t} & \omega_e \end{bmatrix}. \tag{A.8}$$

Using the above expression for H in equation A.7 gives a set of four coupled equations given the elements of the matrix $\frac{d\rho}{dt}$ as linear combination of the elements of rho. These equations are rewritten in the Bloch vector (u, v, w), giving a new set of couple equations

$$\begin{aligned} \dot{u} &= \Delta v, \\ \dot{v} &= -\Delta u + \Omega_0 w, \\ \dot{w} &= -\Omega_0 v. \end{aligned} \tag{A.9}$$

These equations describe the evolution of the atomic density matrix ρ without relaxation terms.

[1] The relaxation term is the one that produces the spontaneous emission

The term w gives the population inversion and u and v are the in phase and phase quadrature components o the atomic dipole moment $\vec{d}$.

It is possible to add spontaneous emission form the excited to the ground state. The effect of the decay on the Bloch vector components u and v for a two-level atoms is calculated to be

$$\left(\frac{du}{dt}\right)_{\text{spont}} = -\frac{\Gamma}{2}u, \quad \left(\frac{dv}{dt}\right)_{\text{spont}} = -\frac{\Gamma}{2}v, \tag{A.10}$$

where Γ is the spontaneous decay rate. These relaxation rates are inserted into equation **??** to yield a master equation for the system known as the *optical Bloch equations*

$$\begin{aligned} \dot{u} &= \Delta v - \frac{\Gamma}{2}u, \\ \dot{v} &= -\Delta u + \Omega_0 w - \frac{\Gamma}{2}v, \\ \dot{w} &= -\Omega_0 v. \end{aligned} \tag{A.11}$$

These equations can be solved for the steady state setting $\dot{u} = \dot{v} = \dot{w} = 0$ giving as a result

$$\begin{bmatrix} u \\ v \\ w \end{bmatrix} = \frac{-1}{\Omega_0(1+s)} \begin{bmatrix} 2\Delta s \\ \Gamma s \\ \Omega_0 \end{bmatrix} \tag{A.12}$$

where the saturation parameter s is defined as

$$s = \frac{2\Omega_0^2}{\Gamma^2 + 4\Delta^2}. \tag{A.13}$$

The saturation parameter s is a measurement of the strength of the atom-field interaction, because the atoms inversion w only depends on s. The steady state population of the excited state is given by $s/(1+s)$, which saturates at $1/2$ when $s = \infty$

A.2 Mean light force on a stationary two-level atom

This section contains the fundamental results of the semiclassical derivation of the mean force experience by a standing two-level atom in a general monochromatic light field. The two-level model is generally appropriate since the phenomena of interest occur when the laser light is near to resonance with an atomic transition.

Having determined the atomic density matrix, the expectation value of the dipole moment can be calculates. Using Ehrenfest's theorem is is possible to deduce a quantum mechanical expression for the force experienced by a particle in a spatially dependent potential. The potential energy of the atom in a classical light field $\vec{E}$ is given by $-\vec{d}\cdot\vec{E}$ and in such a case Ehrenfest's theorem gives the mean light force $\vec{F}$:

$$\vec{F} = \langle\nabla(\vec{d}\cdot\vec{E})\rangle; \quad \text{or} \quad F_i = \langle\vec{d}\,\rangle\cdot\frac{d\vec{E}}{dx_i} \tag{A.14}$$

where the outer triangular brackets indicate the expectation value. This force $\vec{F}$ can be expressed in different notation, inhere is shown two of them. The first in terms of the Bloch vector components and secondly in terms of the atomic polarisability. The expectation value $\langle\vec{d}\,\rangle = \langle\Psi|\,\vec{d}\,|\Psi\rangle$ of the atom dipole moment is substituted into the light force equation (A.14) to give, after some algebra:

$$\vec{F} = \frac{\hbar}{2}(u\nabla\Omega_0 - v\Omega_0\nabla\theta), \tag{A.15}$$

Note that $\vec{F}$ is formed by two terms. The first that depends on u is called the **dipole force**, and the second, depending on v is call the **scattering force**. This categorisation into two types of light force is used in later sections.

In order to express the force in terms of the atomic polarisability α, which is defined by $\langle\vec{d}\,\rangle = \alpha\vec{E} + c.c.$, where α has an imaginary and real part. To use this approach it is convenient to rewrite the light field equation in terms of the intensity I and the field polarization $e^{i\varphi}$ as

$$\vec{E} = \sum_q \hat{e}_q I_q^{1/2} e^{i\varphi_q} e^{i\omega_L t} + c.c. \tag{A.16}$$

where $\hat{e}_q$ are the three Cartesian unity vectors of the I_q and φ_q. Substituting this expressions for

α, $\vec{E}$ and $\langle\vec{d}\rangle$ in equation (A.14). In the rotating wave approximation yields

$$\vec{F} = \Re(\alpha)\nabla I + 2\Im(\alpha)\sum_q I_q \nabla\varphi_q \tag{A.17}$$

In the steady state the polarization is then given by

$$\alpha = (u - iv)\frac{\hbar\Omega_0}{E_0^2} = \frac{\hbar\Omega_0^2(-2\Delta + i\Gamma)}{2I(\Gamma^2 + 2\Omega_0^2 + 4\Delta^2)}. \tag{A.18}$$

The expression for the force can be simplify even more if the field polarisation φ is independent of spatial position, resulting on:

$$\vec{F} = \Re(\alpha)\nabla I + 2\Im(\alpha)I\nabla\varphi. \tag{A.19}$$

Notice that also this force is composed of two distinct terms: the *dipole force* term associated with the real (reactive) part of the polarisation and the *scattering force* associated with the imaginary (dissipative) part.

A.2.1 The dipole force

The dipole trap is some times picture as the a.c. analogy of the resultant force on an induce dipole in an inhomogeneous electrostatic field. The oscillating dipole has a component proportional to u, in phase with the driving electric field. The alignment (parallel or anti-parallel) of this component depends on the detuning, e.g. if the detuning is negative (red detuned) the dipole moment has a component parallel to and in the same direction as the electric field. The potential energy due to this interaction is negative ($-\vec{E}\cdot\vec{d}$). Thus the force acts towards regions of grater $\vec{E}$. Therefore it is concluded that for negative (red) detuning the dipole force is strong-field seeker and for positive (blue) detuning is weak-field seeking.

One particular example of dipole force of an stationary atom in a 1D standing wave, composed by two counterpropagating linearly polarised planes wave. Which result in an electric field $\vec{E} = 2\vec{\epsilon}E_0\cos kz\cos\omega t$. In this electric field the scattering force is zero, but the dipole force is given by

$$\vec{F}_{\text{dipole}} = \frac{4\hbar k\Omega_s^2\Delta\sin 2kz}{\Gamma^2 + 2\Omega_0^2 + 4\Delta^2}. \tag{A.20}$$

where Ω_s is the magnitude of the Rabi frequency due to just one of the plane waves, thus $\Omega_0^2 = 4\Omega_s^2 \cos^2 kz$. This shows that the magnitude and direction of $\vec{F}_{\text{dipole}}$ varies sinusoidally with z. Pushing atoms to the anti-nodes for negative detuning and towards the nodes for positive detuning.

A.2.2 The scattering force

The scattering force is dependent on the second component of the Bloch vector v (the phase quadrature) and with the gradient of the phase φ of the driving electric field. In the case of a single plane wave, the gradient of the phase is propagation vector $\vec{k}$ which gives the direction of the scattering force. The scattering force can be understood in term of momentum transfer between absorption and emission of photons. Imaging an atoms in the way of a plane wave. If the frequency of the light is near resonance, the atom will absorb a photon, receiving a momentum kick equal to $\hbar\vec{k}$. The following spontaneous emission has a random direction. After many cycles the emission kicks cancel out on average, but the absorption kicks are always in the same direction, consequently they add. As a result the atom is subject of a net time-average force:

$$\vec{F}_{\text{scatt}} = \frac{\hbar\vec{k}\Gamma\Omega_0^2}{\Gamma^2 + 2\Omega_0^2 + 4\Delta^2}. \tag{A.21}$$

This equation shows that for low intensity field ($\Omega_0 < \Gamma$) the scattering force is proportional to the field intensity, but has an upper limit for high intensity fields of

$$\vec{F}_{\text{scatt(max)}} = \frac{\hbar\vec{k}\Gamma}{2} \quad \text{when } \Omega_0 \gg \Gamma, \Delta. \tag{A.22}$$

The idea of scattering force is associated with a process that involves absorption followed by incoherent spontaneous emission.

.

APPENDIX B

DETECTION MODULE IN COMPUTER CONTROL

As part of the computer control different modules have been created to facilitate the following of long experimental sequences. One of these modules is the detection module which is shown in table B.1. This modules controls the corresponding channels needed to perform absorption imaging, and works in conjunction with the camera control (sect. 3.6).

The detection is performed after the atom cloud is left to freely expend for a period of time TOF[1]. First the camera is triggered, then a flash of detection light is shone. The camera need $\approx$ 90ms to readout an image, thus a readout time of 120ms is more than enough for the camera to finish. A warm up slot for the AOM is added to ensure that the intensity of the flash is as equal as possible for both flashes. After the AOM warm up the same process of triggering the camera, the flash of detection light and readout time is repeated to produce the bright field image I_B.

The implementation of the past slot (sect. 3.6) in the detection module can be done by adding a extra slot at the beginning of the module where the offset time[2] will be 10ms as well as the slot length.

[1]The TOF time is set in the previous module.
[2]10 ms is the maximum time needed by the VCO to reach the resonance frequency.

Time slot[ms]/ Channels	**Trigger pulse 1** 0.05	**Detection flash 1** 0.08	**Readout 1** 120	**AOM warm up** 500	**Trigger pulse 2** 0.05	**Detection flash 2** 0.08	**Readout 2** 120
Digital	[T/F]						
camera trigger	T	F	-	-	T	F	-
shutter 3D MOT	T	-	-	-	-	-	-
shutter 2D MOT	T	-	-	-	-	-	-
shutter pushing beam	T	-	-	-	-	-	-
shutter detection GC	F	-	-	F	-	-	T
shutter detection	T	-	-	-	-	-	-
dipole trap AOM	F	F	F	-	-	-	-
AOM detection	F	T	F	T	F	T	F
Analogue	Value[V]/ramp[T/F]						
AOM detection intensity	1.8/F	-	0/F	0/F	1.8/F	-	-
AOM detection detuning	260/F	-	-	-	-	-	-
Dipole trap	0/F	-	-	-	-	-	-
VISA							

Table B.1: *Detection module in computer control.*

APPENDIX C

DATA STRUCTURE

The raw data is written in a format called HDF5 (*Hierarchical Data Format Version 5*). It has the advantage of storing information in a hierarchical way as sub-folders. Using this we are able to organise our data, keeping together the pictures and other relevant parameters from the experiment and camera that belong to the same experimental sequence.

In order to illustrate the structure of the data, the directory trees below show the two data types that were used (figures C.1 and C.2), where the datasets are denoted by "." and the groups by "/". The first one (fig. C.1) is not as efficient for extraction of raw images because the data file is saved as a dataset, this means that in order to subtract a piece of information the hole dataset has to be read. The same happens to the camera file. In the second version some improvements to the information classification were done by adding extra datasets and groups. The second data type (fig. C.2) improves the reading speed of raw pictures by subdividing the images in two different directories, making it possible to read individual image.

The development of a new data structure came after realising that the reading time of 84 files took $\approx 160s$ which is a long time for just reading the data. In order to choose the best data structure (fastest to read), four test structure were created by organising differently the information inside the HDF5 file using data sets and groups. The test structures are:
test structure 1 = data structure type 1 (fig C.1)
test structure 2 = data sets of: Camera setting, Atoms image, No atoms image and OptDens
test structure 3 = data sets of: Camera setting, Raw data (Atoms image, No atoms image) and

Test structure	read single image [s]	read both images [s]	results
1	173	177	slowest
2	31	62	
3	63	63	
4	30	60	fastest

Table C.1: Tested data structures for reading time.

Process data

test structure 4 = data sets of: Camera setting and groups of: RawData(/Atoms image, /No atoms image), Processed data and Experiment settings

The test was performed by reading the raw images of atoms and no atoms, and determining if it is faster to read individual images or a combined way. Which structure read the fastest a single image was also tested. The result of the time needed to read 84 files is shown in table C.1.

As a conclusion, structure 2 and 4 offer the advantage that atoms and no atoms images are stored separately making them faster to read single image. Reading both images from structure 2, 3 and 4 is almost the same but 2 and 4 are still faster. Also storing the images in different folders offer the flexibility of reading individual files and doing it faster than store them together. The chosen structure was test 4 since is the one with shortest reading time and with more organisation. The final data structure is presented in figure C.2.

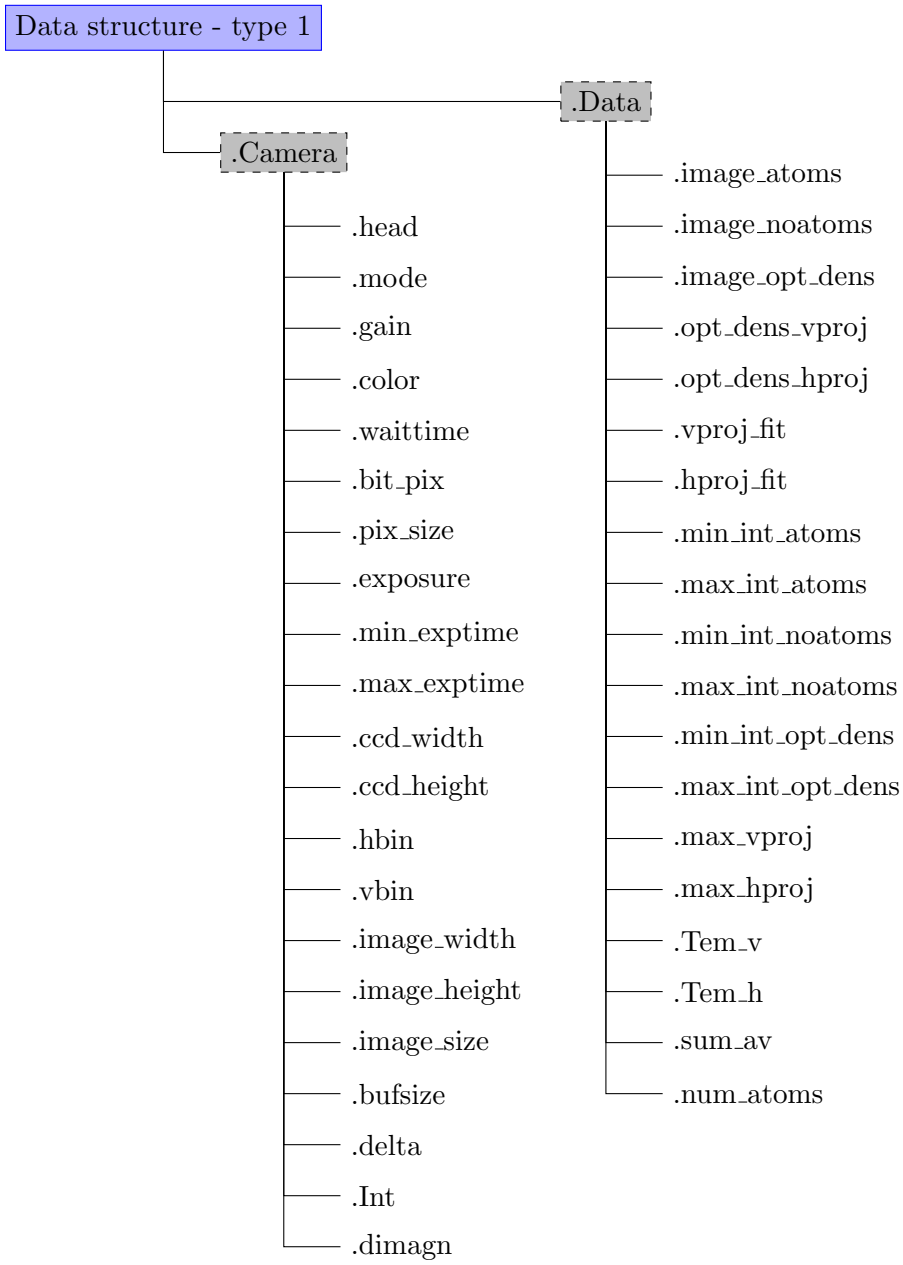

Figure C.1: Data structure type 1

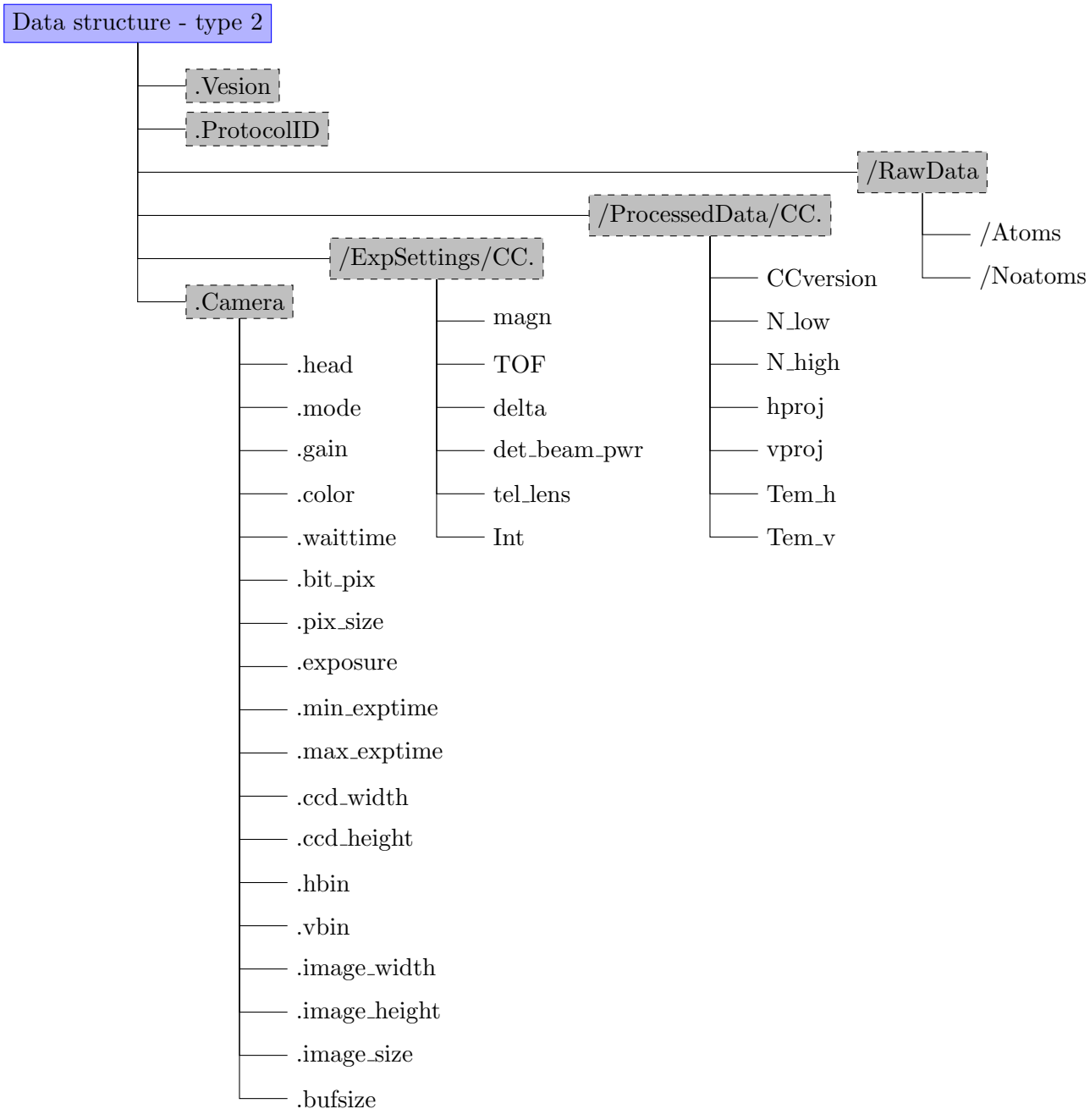

Figure C.2: Data structure type 2

APPENDIX D

NORMALISED 1D QUADRUPOLE TRAP DISTRIBUTION

This appendix shows how the 1D density distribution in a magnetic quadrupole traps used in figure 4.1 is obtained.

The density distribution of an atom cloud held in a quadrupole trap has been obtain in section 4.2 and is given by eq. 4.11. From this equation is know that the density distribution[1] goes as $\sim \exp(-|\vec{r}|)$. If gravity is not included this density distribution can be written as:

$$n(r) = \frac{a}{4\pi} \exp(-ar), \tag{D.1}$$

with $a = \beta C$. Rather than use the calculated cloud size σ_0 along the x axis, where integrals over the other two axis (y, x) have been performed, it is assumed that the density distribution (eq. D.1) just depends on x. By assuming this the 3D density distribution becomes a 1D distribution that has to be normalised.

The new distribution is expressed as:

$$n(x) = \frac{\exp(-a|x|)}{N}, \tag{D.2}$$

with N the normalization factor, which is calculated with the normalisation condition $\int n(x) = 1$, therefore

$$N = \int_{-\infty}^{\infty} \exp(-ax)dx = \frac{2}{a}. \tag{D.3}$$

[1] A transformation of coordinates $2z \to z'$ was performed to have an isotropic distribution.

Also the standard deviation σ of this 1D density distribution (eq. D.2) can be calculated as

$$\sigma^2 = \langle x^2 \rangle, \tag{D.4}$$

$$= \int_{-\infty}^{\infty} x^2 n(x) dx, \tag{D.5}$$

$$= \frac{2}{a^2}, \tag{D.6}$$

where the symmetry of the distribution has been used. The 1D density distribution is rewritten in terms of the standard deviation and replacing the normalisation factor one obtain:

$$n(x) = \frac{1}{\sqrt{2}\sigma} \exp\left(-\frac{\sqrt{2}|x|}{\sigma}\right). \tag{D.7}$$

This equation is the one used in figure 4.1. The half with half maximum (HWHM) is calculated as the value of x when the distribution has dropped to half of it maximum values as:

$$\exp\left(-\frac{\sqrt{2}|x|}{\sigma}\right) = \frac{1}{2}, \tag{D.8}$$

solving this equation for x one obtains

$$\text{HWHM} = \frac{\ln(2)}{\sqrt{2}}\sigma \approx 0.49\sigma. \tag{D.9}$$

In order to quantify the extension of the distribution numerical integrals of the 1D distribution (eq. D.7) were realised at several standard deviation σ and HWHM, the results are presented in table D.1. This percentage of the distribution have been used to define the region of interest (ROI) to calculate the standard deviation of a falling cloud σ_t (sect. 4.4)

Num. of σ	% of the distribution	Num. of HFHM	% of the distribution
1	75.69	1	50.00
2	94.09	2	75.00
3	98.56	3	87.50
4	99.65	4	93.75
5	99.91	5	96.87
6	99.98	6	98.44
7	99.99	7	99.22
8	99.999	8	99.61
9	99.9997	9	99.80
10	99.9999	10	99.90

Table D.1: *Percentage of the 1D density distribution at various distances.* This table shows the percentage of the 1D distribution as a result of integrating n(x) (eq.D.7) from (-Num. of σ) to (Num. of σ) for the left side. And in the similar way for number of HWHF in the right side.

.

.

APPENDIX E

LIST OF ABBREVIATIONS

1D	one-dimensional
2D	two-dimensional
3D	three-dimensional
AOM	acousto-optic modulator
AR	anti-reflection
BEC	Bose-Einstein condensate/condensation
CCD	charged-couple device
DDS	direct digital synthesis
DFB	distributed feedback
DFG	degenerate Fermi gases
DT	dipole trap
ECDL	external cavity diode laser
EOM	electro optical modulator
FM	frequency modulation
FPGA	field programmable gate array
FWHM	full width half maximum
GUI	graphic user interface
HDF5	hierarchical data format version 5

HWHM	half width half maximum
MOT	magneto-optical trap
MT	magnetic trap
OD	optical density
OP	optical pumping
PCI	Peripheral Component Interconnect
PD	Photo diode
PSD	phase space density
PXI	PCI eXtensions for Instrumentation
PZT	piezo-electric transducer
QT	quadrupole trap
ROI	region of interest
RF	radio frequency
TA	tapered amplifier
TCP/IP	transmission control protocol/internet protocol
TOF	time of flight
UHV	ultrahigh vacuum
VCO	voltage controlled oscillator
VISA	virtual instrument software architecture
XML	extensible markup language

LIST OF FIGURES

LIST OF TABLES

.

LIST OF REFERENCES

[1] M. H. Anderson, J. R. Ensher, M. R. Matthews, C. E. Wieman, and E. A. Cornell, "Observation of bose-einstein condensation in a dilute atomic vapor.," *Science (New York, N.Y.)*, vol. 269, pp. 198–201, July 1995.

[2] K. Davis, M. Mewes, M. Andrews, N. van Druten, D. Durfee, D. Kurn, and W. Ketterle, "Bose-Einstein Condensation in a Gas of Sodium Atoms," *Physical Review Letters*, vol. 75, pp. 3969–3973, Nov. 1995.

[3] C. Bradley, C. Sackett, J. Tollett, and R. Hulet, "Evidence of Bose-Einstein condensation in an atomic gas with attractive interactions," *Physical Review Letters*, vol. 75, pp. 1687–1690, Aug. 1995.

[4] M. Endres, M. Cheneau, T. Fukuhara, C. Weitenberg, P. Schauss, C. Gross, L. Mazza, M. C. Bañuls, L. Pollet, I. Bloch, and S. Kuhr, "Observation of correlated particle-hole pairs and string order in low-dimensional Mott insulators.," *Science (New York, N.Y.)*, vol. 334, pp. 200–3, Oct. 2011.

[5] G. Roati, C. D'Errico, L. Fallani, M. Fattori, C. Fort, M. Zaccanti, G. Modugno, M. Modugno, and M. Inguscio, "Anderson localization of a non-interacting Bose-Einstein condensate.," *Nature*, vol. 453, pp. 895–8, June 2008.

[6] J. Billy, V. Josse, Z. Zuo, A. Bernard, B. Hambrecht, P. Lugan, D. Clément, L. Sanchez-Palencia, P. Bouyer, and A. Aspect, "Direct observation of Anderson localization of matter waves in a controlled disorder.," *Nature*, vol. 453, pp. 891–4, June 2008.

[7] G. Modugno, "Anderson localization in Bose–Einstein condensates," *Reports on Progress in Physics*, vol. 73, p. 102401, Oct. 2010.

[8] I. Bloch, J. Dalibard, and S. Nascimbène, "Quantum simulations with ultracold quantum gases," *Nature Physics*, vol. 8, pp. 267–276, Apr. 2012.

[9] H. Feshbach, "Unified theory of nuclear reactions," *Annals of Physics*, vol. 5, pp. 357–390, Dec. 1958.

[10] A. Einstein, "Quantentheorie des einatomigen idealen Gases," *Sitzungsber. Preuss. Akab. Wiss.*, vol. Bericht 3, p. 18, 1925.

[11] S. N. Bose, "Planck ' s Law and Light Quantum Hypothesis .," *Zeitschrift fur Physik*, vol. 26, pp. 178–181, 1924.

[12] W. Ketterle, D. S. Durfee, and D. M. Stamper-Kurn, "Making, probing and understanding Bose-Einstein condensates," *arXiv:cond-mat/9904034v2*, p. 84, Apr. 1999.

[13] T. Hänsch and A. Schawlow, "Cooling of gases by laser radiation," *Optics Communications*, vol. 13, pp. 68–69, Jan. 1975.

[14] W. D. Phillips, J. V. Prodan, and H. J. Metcalf, "Laser cooling and electromagnetic trapping of neutral atoms," *Journal of the Optical Society of America B*, vol. 2, p. 1751, Nov. 1985.

[15] H. Hess, "Evaporative cooling of magnetically trapped and compressed spin-polarized hydrogen," *Physical Review B*, vol. 34, pp. 3476–3479, Sept. 1986.

[16] N. Masuhara, J. Doyle, J. Sandberg, D. Kleppner, T. Greytak, H. Hess, and G. Kochanski, "Evaporative cooling of spin-polarized atomic hydrogen," *Physical Review Letters*, vol. 61, pp. 935–938, Aug. 1988.

[17] K. Davis, M.-O. Mewes, M. Joffe, M. Andrews, and W. Ketterle, "Evaporative Cooling of Sodium Atoms," *Physical Review Letters*, vol. 74, pp. 5202–5205, June 1995.

[18] C. Adams, H. Lee, N. Davidson, M. Kasevich, and S. Chu, "Evaporative cooling in a crossed dipole trap," *Physical Review Letters*, vol. 74, pp. 3577–3580, May 1995.

[19] K. B. Davis, M. O. Mewes, and W. Ketterle, "An analytical model for evaporative cooling of atoms," *Applied Physics B Laser and Optics*, vol. 60, no. 2-3, pp. 155–159, 1995.

[20] W. Ketterle and N. V. Druten, "Evaporative cooling of trapped atoms," *Advances In Atomic, Molecular, and Optical Physics*, vol. 37, pp. 181–236, 1996.

[21] T. Bergeman, G. Erez, and H. Metcalf, "Magnetostatic trapping fields for neutral atoms," *Physical Review A*, vol. 35, pp. 1535–1546, Feb. 1987.

[22] A. Migdall, J. Prodan, W. Phillips, T. Bergeman, and H. Metcalf, "First Observation of Magnetically Trapped Neutral Atoms," *Physical Review Letters*, vol. 54, pp. 2596–2599, June 1985.

[23] W. Petrich, M. Anderson, J. Ensher, and E. Cornell, "Stable, Tightly Confining Magnetic Trap for Evaporative Cooling of Neutral Atoms," *Physical Review Letters*, vol. 74, pp. 3352–3355, Apr. 1995.

[24] E. Majorana, "Atomi orientati in campo magnetico variabile," *Il Nuovo Cimento*, vol. 9, pp. 43–50, Feb. 1932.

[25] D. Brink and C. Sukumar, "Majorana spin-flip transitions in a magnetic trap," *Physical Review A*, vol. 74, p. 035401, Sept. 2006.

[26] D. Naik and C. Raman, "Optically plugged quadrupole trap for Bose-Einstein condensates," *Physical Review A*, vol. 71, p. 033617, Mar. 2005.

[27] R. Dubessy, K. Merloti, L. Longchambon, P.-E. Pottie, T. Liennard, A. Perrin, V. Lorent, and H. Perrin, "Rubidium-87 Bose-Einstein condensate in an optically plugged quadrupole trap," *Physical Review A*, vol. 85, p. 013643, Jan. 2012.

[28] Y.-J. Lin, A. Perry, R. Compton, I. Spielman, and J. Porto, "Rapid production of 87Rb Bose-Einstein condensates in a combined magnetic and optical potential," *Physical Review A*, vol. 79, p. 063631, June 2009.

[29] D. L. Jenkin, D. J. McCarron, M. P. Köppinger, H. W. Cho, S. A. Hopkins, and S. L. Cornish, "Bose-Einstein condensation of 87Rb in a levitated crossed dipole trap," *The European Physical Journal D*, vol. 65, pp. 11–18, Apr. 2011.

[30] M. Barrett, J. Sauer, and M. Chapman, "All-Optical Formation of an Atomic Bose-Einstein Condensate," *Physical Review Letters*, vol. 87, p. 010404, June 2001.

[31] S. Burger, F. S. Cataliotti, C. Fort, P. Maddaloni, F. Minardi, and M. Inguscio, "Quasi-2D Bose-Einstein condensation in an optical lattice," *Europhysics Letters (EPL)*, vol. 57, pp. 1–6, Jan. 2002.

[32] J. F. Bertelsen, *Ultracold Atomic Gases*. PhD thesis, University of Aarhus, 2007.

[33] M. Baumert, *Dipole traps and optical lattices for quantum simulations*. PhD thesis, University of Birmingham, 2013.

[34] M. Holynski, *Creating a two dimensional cold mixture experiment*. PhD thesis, University of Birmingham, 2012.

[35] N. Meyer, *Building and characterisation of a dual species quantum simulator*. PhD thesis, Universität Hamburg, 2014.

[36] C. O'Neale, *Towards solitons in a 2D BEC apparatus*. PhD thesis, University of Birmingham, 2014.

[37] R. Dum, J. Cirac, M. Lewenstein, and P. Zoller, "Creation of dark solitons and vortices in Bose-Einstein condensates," *Physical Review Letters*, vol. 80, pp. 2972–2975, Apr. 1998.

[38] S. Burger, K. Bongs, S. Dettmer, W. Ertmer, and K. Sengstock, "Dark Solitons in Bose-Einstein Condensates," *Physical Review Letters*, vol. 83, pp. 5198–5201, Dec. 1999.

[39] J. H. Denschlag, J. E. Simsarian, H. Häffner, C. McKenzie, A. Browaeys, D. Cho, K. Helmerson, S. L. Rolston, and W. D. Phillips, "A Bose-Einstein condensate in an optical lattice," *Journal of Physics B: Atomic, Molecular and Optical Physics*, vol. 35, pp. 3095–3110, July 2002.

[40] G. Huang, V. Makarov, and M. Velarde, "Two-dimensional solitons in Bose-Einstein condensates with a disk-shaped trap," *Physical Review A*, vol. 67, p. 023604, Feb. 2003.

[41] I. Bloch, "Ultracold quantum gases in optical lattices," *Nature Physics*, vol. 1, pp. 23–30, Oct. 2005.

[42] S. F. Huelga and M. B. Plenio, "Vibrations, quanta and biology," *Contemporary Physics*, vol. 54, pp. 181–207, June 2013.

[43] L. Marcassa, G. Telles, S. Muniz, and V. Bagnato, "Collisional losses in a K-Rb cold mixture," *Physical Review A*, vol. 63, p. 013413, Dec. 2000.

[44] J. Goldwin, S. Papp, B. DeMarco, and D. Jin, "Two-species magneto-optical trap with $ˆ{40}$K and $ˆ{87}$Rb," *Physical Review A*, vol. 65, p. 021402, Jan. 2002.

[45] S. Inouye, M. R. Andrews, J. Stenger, H.-J. Miesner, D. M. Stamper-Kurn, and W. Ketterle, "Observation of Feshbach resonances in a Bose-Einstein condensate," *Nature*, vol. 392, pp. 151–154, Mar. 1998.

[46] A. Simoni, F. Ferlaino, G. Roati, G. Modugno, and M. Inguscio, "Magnetic Control of the Interaction in Ultracold K-Rb Mixtures," *Physical Review Letters*, vol. 90, p. 163202, Apr. 2003.

[47] A. Roth, *Vacuum Sealing Techniques*. Springer, 1994.

[48] D. Anderson and J. Reichel, "Cold atom system with atom chip wall," *US Patent 7,126,112*, vol. 2, no. 12, pp. 1–4, 2006.

[49] A. Alfantazi and R. Moskalyk, "Processing of indium: a review," *Minerals Engineering*, vol. 16, pp. 687–694, Aug. 2003.

[50] H. A. Adam, S. Kaufman, and B. S. Liley, "Indium seals for dismountable vacuum systems," *Journal of Scientific Instruments*, vol. 34, pp. 123–124, Mar. 1957.

[51] K. J. Weatherill, J. D. Pritchard, P. F. Griffin, U. Dammalapati, C. S. Adams, and E. Riis, "A versatile and reliably reusable ultrahigh vacuum viewport.," *Review of Scientific Instruments*, vol. 80, p. 026105, Feb. 2009.

[52] B. Kaltenhäuser, H. Kübler, A. Chromik, J. Stuhler, and T. Pfau, "Low retaining force optical viewport seal.," *Review of Scientific Instruments*, vol. 78, p. 046107, Apr. 2007.

[53] AIM, "Sealing with indium."

[54] Cookso-Electronics, "Sealing with Indium," 2013.

[55] A. Vogel, M. Schmidt, K. Sengstock, K. Bongs, W. Lewoczko, T. Schuldt, A. Peters, T. Van Zoest, W. Ertmer, E. Rasel, T. Steinmetz, J. Reichel, T. Könemann, W. Brinkmann, E. Göklü, C. Lämmerzahl, H. Dittus, G. Nandi, W. Schleich, and R. Walser, "Bose–Einstein condensates in microgravity," *Applied Physics B*, vol. 84, pp. 663–671, July 2006.

[56] Leibniz Universität Hannover, "Quantum Gases in Microgravity (QUANTUS)."

[57] A. Vogel, *Bose-Einstein condensates for space applications and novel teaching concepts*. PhD thesis, Universität Hamburg, 2009.

[58] T. G. Tiecke, *Feshbach resonances in ultracold mixtures of the fermionic quantum gases 6Li and 40K*. PhD thesis, University of Amsterdam, 2009.

[59] X. Baillard, A. Gauguet, S. Bize, P. Lemonde, P. Laurent, A. Clairon, and P. Rosenbusch, "Interference-filter-stabilized external-cavity diode lasers," *Optics Communications*, vol. 266, pp. 609–613, Oct. 2006.

[60] G. C. Bjorklund, M. D. Levenson, W. Lenth, and C. Ortiz, "Frequency modulation (FM) spectroscopy," *Applied Physics B Photophysics and Laser Chemistry*, vol. 32, pp. 145–152, Nov. 1983.

[61] K. B. MacAdam, "A narrow-band tunable diode laser system with grating feedback, and a saturated absorption spectrometer for Cs and Rb," *American Journal of Physics*, vol. 60, p. 1098, Dec. 1992.

[62] D. W. Preston, "Doppler-free saturated absorption: Laser spectroscopy," *American Journal of Physics*, vol. 64, p. 1432, Nov. 1996.

[63] D. Steck, "Rubidium 87 D line data," no. available online at http://steck.us/alkalidata (revision 2.0.1, 2 May 2008), p. 31.

[64] G. Ritt, G. Cennini, C. Geckeler, and M. Weitz, "Laser frequency offset locking using a side of filter technique," *Applied Physics B*, vol. 79, pp. 363–365, June 2004.

[65] P. Tudor, *Laser frequency offset locking with digital electronics.* 4th year dissertation, University of Birmingham, 2013.

[66] G. Duckworth, *Investigating the use of Digital Electronics in Fast Offset Locking of Lasers.* 4th year dissertation, University of Birmingham, 2013.

[67] A. C. Wilson, J. C. Sharpe, C. R. McKenzie, P. J. Manson, and D. M. Warrington, "Narrow-Linewidth Master-oscillator power amplifier based on a semiconductor tapered amplifier," *Applied Optics*, vol. 37, p. 4871, July 1998.

[68] Evanescent-Optics-INC., "The wave guide, modes and evanescent tails basics."

[69] V. V. Vladimirskii, "Magnetic mirrors, channels and bottles for cold neutrons," *Sov. Phys.*, vol. 12, pp. 740–746, 1961.

[70] C. V. Heer, "Feasibility of containment of quantum magnetic dipoles," *Review of Scientific Instruments*, vol. 34, pp. 532–537, 1963.

[71] D. Pritchard, "Cooling Neutral Atoms in a Magnetic Trap for Precision Spectroscopy," *Physical Review Letters*, vol. 51, pp. 1336–1339, Oct. 1983.

[72] W. Ketterle and D. E. Pritchard, "Trapping and focusing ground state atoms with static fields," *Applied Physics B Photophysics and Laser Chemistry*, vol. 54, pp. 403–406, May 1992.

[73] H. J. Metcalf and P. van der Straten, *Laser Cooling and Trapping*. Verlag New York: Springer, 1999.

[74] J. Van Dongen, C. Zhu, D. Clement, G. Dufour, J. L. Booth, and K. W. Madison, "Trap-depth determination from residual gas collisions," *Physical Review A*, vol. 84, p. 022708, Aug. 2011.

[75] D. Fagnan, *Study of Collision Cross Section of Ultra-Cold Rubidium using a Magneto-Optic and pure Magnetic trap*. Bachelor thesis, University of British Columbia, 2009.

[76] M. Greiner, I. Bloch, T. Hänsch, and T. Esslinger, "Magnetic transport of trapped cold atoms over a large distance," *Physical Review A*, vol. 63, p. 031401, Feb. 2001.

[77] H. J. Lewandowski, D. M. Harber, D. L. Whitaker, and E. A. Cornell, "Simplified System for Creating a Bose–Einstein Condensate," *Journal of Low Temperature Physics*, vol. 132, pp. 309–367, Sept. 2003.

[78] K. Nakagawa, Y. Suzuki, M. Horikoshi, and J. Kim, "Simple and efficient magnetic transport of cold atoms using moving coils for the production of Bose–Einstein condensation," *Applied Physics B*, vol. 81, pp. 791–794, Sept. 2005.

[79] J. Bertelsen, H. Andersen, S. Mai, and M. Budde, "Mixing of ultracold atomic clouds by merging of two magnetic traps," *Physical Review A*, vol. 75, p. 013404, Jan. 2007.

[80] N. L. Smith, W. H. Heathcote, G. Hechenblaikner, E. Nugent, and C. J. Foot, "Quasi-2D confinement of a BEC in a combined optical and magnetic potential," *Journal of Physics B: Atomic, Molecular and Optical Physics*, vol. 38, pp. 223–235, Feb. 2005.

[81] D. Comparat, A. Fioretti, G. Stern, E. Dimova, B. Tolra, and P. Pillet, "Optimized production of large Bose-Einstein condensates," *Physical Review A*, vol. 73, p. 043410, Apr. 2006.

[82] R. Grimm, M. Weidemüller, and Y. B. Ovchinnikov, "Optical dipole traps for neutral atoms," *Advances In Atomic, Molecular, and Optical Physics*, vol. 42, p. 39, Feb. 1999.

[83] M. Erhard, *Experimente mit mehrkomponentigen Bose-Einstein-Kondensaten.* PhD thesis, Universität Hamburg, 2004.

[84] E. Hecht, *Optics.* New York: Addison-Wesley Longman, 3rd ed., 1998.

[85] K. Huang, *Statistical mechanics.* Massachusetts Institute of Technolog: John Wiley & Sons, second ed., 1987.

[86] V. Bagnato, D. Pritchard, and D. Kleppner, "Bose-Einstein condensation in an external potential," *Physical Review A*, vol. 35, pp. 4354–4358, May 1987.

[87] Y. Kagan, E. Surkov, and G. Shlyapnikov, "Evolution of a Bose-condensed gas under variations of the confining potential," *Physical Review A*, vol. 54, pp. R1753–R1756, Sept. 1996.

[88] Y. Castin and R. Dum, "Bose-Einstein condensates in time dependent traps," *Physical Review Letters*, vol. 77, pp. 5315–5319, Dec. 1996.

[89] L. P. Pitaevskii and A. Rosch, "Breathing modes and hidden symmetry of trapped atoms in two dimensions," *Physical Review A*, vol. 55, pp. R853–R856, Feb. 1997.

[90] F. Dalfovo, C. Minniti, S. Stringari, and L. Pitaevskii, "Nonlinear dynamics of a Bose condensed gas," *Physics Letters A*, vol. 227, pp. 259–264, Mar. 1997.

[91] A. Parkins and D. Walls, "The physics of trapped dilute-gas Bose–Einstein condensates," *Physics Reports*, vol. 303, pp. 1–80, Sept. 1998.

[92] F. Dalfovo, S. Giorgini, and S. Stringari, "Theory of Bose-Einstein condensation in trapped gases," *Reviews of Modern Physics*, vol. 71, pp. 463–512, Apr. 1999.

[93] L. P. Pitaevskii and S. Stringari, *Bose-Einstein Condensation.* New York: Publisher Oxford University Press, 2003.

[94] M. Brinkmann, *Optimierung der Detektion und Auswertung von 87Rb-Spinor-Kondensaten.* Diplomarbeit, Universität Hamburg, 2005.

[95] C. Becker, *Multi component Bose-Einstein condensates from mean field physics to strong correlations.* PhD thesis, Universität Hamburg, 2008.

[96] Mitutoyo, *Micrioscope Units and Objectives Catalog*.

[97] J. Denschlag, "Generating Solitons by Phase Engineering of a Bose-Einstein Condensate," *Science*, vol. 287, pp. 97–101, Jan. 2000.

[98] I. Yavin, M. Weel, A. Andreyuk, and A. Kumarakrishnan, "A calculation of the time-of-flight distribution of trapped atoms," *American Journal of Physics*, vol. 70, no. 2, p. 149, 2002.

[99] P. Lett, R. Watts, C. Westbrook, W. Phillips, P. Gould, and H. Metcalf, "Observation of Atoms Laser Cooled below the Doppler Limit," *Physical Review Letters*, vol. 61, pp. 169–172, July 1988.

[100] S. Chu, L. Hollberg, J. Bjorkholm, A. Cable, and A. Ashkin, "Three-dimensional viscous confinement and cooling of atoms by resonance radiation pressure," *Physical Review Letters*, vol. 55, pp. 48–51, July 1985.

[101] A. M. Steane and C. J. Foot, "Laser cooling below the Doppler limit in a magneto-optical trap," *Europhysics Letters (EPL)*, vol. 14, pp. 231–236, Feb. 1991.

[102] P. Kohns, P. Buch, W. Süptitz, C. Csambal, and W. Ertmer, "On-Line Measurement of Sub-Doppler Temperatures in a Rb Magneto-optical Trap-by-Trap Centre Oscillations," *Europhysics Letters (EPL)*, vol. 22, pp. 517–522, June 1993.

[103] C. Westbrook, R. Watts, C. Tanner, S. Rolston, W. Phillips, P. Lett, and P. Gould, "Localization of atoms in a three-dimensional standing wave," *Physical Review Letters*, vol. 65, pp. 33–36, July 1990.

[104] J.-Y. Courtois, G. Grynberg, B. Lounis, and P. Verkerk, "Recoil-induced resonances in cesium: An atomic analog to the free-electron laser," *Physical Review Letters*, vol. 72, pp. 3017–3020, May 1994.

[105] T. M. Brzozowski, M. Maczynska, M. Zawada, J. Zachorowski, and W. Gawlik, "Time-of-flight measurement of the temperature of cold atoms for short trap-probe beam distances," *Journal of Optics B: Quantum and Semiclassical Optics*, vol. 4, pp. 62–66, Feb. 2002.

[106] P. Arora, S. B. Purnapatra, A. Acharya, R. Kumar, and A. Sen Gupta, "Measurement of temperature of atomic cloud using time-of-flight technique," *MAPAN*, vol. 27, pp. 31–39, Apr. 2012.

[107] M. Landini, S. Roy, L. Carcagní, D. Trypogeorgos, M. Fattori, M. Inguscio, and G. Modugno, "Sub-Doppler laser cooling of potassium atoms," *Physical Review A*, vol. 84, p. 043432, Oct. 2011.

[108] S. P. Ram, S. R. Mishra, S. K. Tiwari, and H. S. Rawat, "Temperature and phase-space density of a cold atom cloud in a quadrupole magnetic trap," *Journal of the Korean Physical Society*, vol. 65, pp. 462–470, Sept. 2014.

[109] S. Händel, *Experiments on ultracold quantum gases of 85Rb and 87Rb*. PhD thesis, Durham University, 2011.

[110] D. M. Harber, J. M. McGuirk, J. M. Obrecht, and E. A. Cornell, "Thermally induced losses in ultra-cold atoms magnetically trapped near room-temperature surfaces," *Journal of Low Temperature Physics*, vol. 133, pp. 229–238, Nov. 2003.

[111] G. Reinaudi, T. Lahaye, A. Couvert, Z. Wang, and D. Guéry-Odelin, "Evaporation of an atomic beam on a material surface," *Physical Review A*, vol. 73, p. 035402, Mar. 2006.

[112] E. Raab, M. Prentiss, A. Cable, S. Chu, and D. Pritchard, "Trapping of neutral Sodium atoms with radiation pressure," *Physical Review Letters*, vol. 59, pp. 2631–2634, Dec. 1987.

[113] K. Dieckmann, R. Spreeuw, M. Weidemüller, and J. Walraven, "Two-dimensional magneto-optical trap as a source of slow atoms," *Physical Review A*, vol. 58, pp. 3891–3895, Nov. 1998.

[114] D. S. Weiss, E. Riis, Y. Shevy, P. J. Ungar, and S. Chu, "Optical molasses and multilevel atoms: experiment," *Journal of the Optical Society of America B*, vol. 6, p. 2072, Nov. 1989.

[115] J. Dalibard and C. Cohen-Tannoudji, "Laser cooling below the Doppler limit by polarization gradients: simple theoretical models," *Journal of the Optical Society of America B*, vol. 6, p. 2023, Nov. 1989.

[116] P. D. Lett, W. D. Phillips, S. L. Rolston, C. E. Tanner, R. N. Watts, and C. I. Westbrook, "Optical molasses," *Journal of the Optical Society of America B*, vol. 6, p. 2084, Nov. 1989.

[117] P. J. Ungar, D. S. Weiss, E. Riis, and S. Chu, "Optical molasses and multilevel atoms: theory," *Journal of the Optical Society of America B*, vol. 6, p. 2058, Nov. 1989.

[118] D. E. Pritchard, K. Helmerson, and A. G. Martin, *Proceedings of the Eleventh International Conference on Atomic Physics, 4-8 July 1988 Paris, France followed by Proceedings of the Symposium in honor of Jean Brossel, 9 July 1988, Paris, France.* Singapore; New Jersey: World Scientific, 1989.

[119] S. A. Hopkins, *Laser cooling of rubidium atoms in a magneto-optical trap.* PhD thesis, The Open University, Mar. 1996.